Reconfigurable graphene complex oxide nanostructures

by

Qing Guo

B.S., Nankai University, 2013

Submitted to the Graduate Faculty of

the Dietrich School of Arts and Sciences in partial fulfillment

of the requirements for the degree of

Doctor of Philosophy

University of Pittsburgh

2020

UNIVERSITY OF PITTSBURGH

DIETRICH SCHOOL OF ARTS AND SCIENCES

This dissertation was presented

by

Qing Guo

It was defended on

May 29th 2020

and approved by

Dr. Jeremy Levy, Department of Physics and Astronomy, University of Pittsburgh

Dr. Hrvoje Petek, Department of Physics and Astronomy, University of Pittsburgh

Dr. Roger Mong, Department of Physics and Astronomy, University of Pittsburgh

Dr. Carlos Badenes, Department of Physics and Astronomy, University of Pittsburgh

Dr. Susan Fullerton, Department of Chemical and Petroleum Engineering

Dissertation Director: Dr. Jeremy Levy, Department of Physics and Astronomy, University of Pittsburgh

Reconfigurable graphene complex oxide nanostructures

Qing Guo, PhD

University of Pittsburgh, 2020

Graphene and complex-oxide heterostructures collectively exhibit nearly all of the known major properties in solid-state materials. Our goal is to integrate these two materials to create new emergent properties and functionalities. A new wet graphene transfer method is developed and used to integrate graphene with the complex-oxide system $LaAlO_3/SrTiO_3$. Interactions between the graphene and $LaAlO_3/SrTiO_3$ interface are controlled at nanoscale dimensions using a conductive atomic force microscopy technique developed previously for the complex-oxide interface. The resulting hybrid structures exhibit novel and useful electronic and optical properties, many of which depend critically on controlling the chemical potential of graphene relative to the charge-neutrality point. The local density of states can be altered in graphene by programmable changes of the conductance of the complex oxide interface. In one experiment, an edge-mixed quantum Hall effect is observed in sketched graphene/complex-oxide $p-n$ junction devices. Magnetotransport measurements of superlattice structures show characteristic interference features that can be associated with the periodically patterned interface. Coulomb drag measurements between single-layer graphene and a conductive $LaAlO_3/SrTiO_3$ interface is also performed in these hybrid devices. The metallic behavior and high transparency of graphene make it an ideal top electrode for controlling magnetic properties at the $LaAlO_3/SrTiO_3$ interface. We discuss possible new directions based on this highly versatile hybrid material platform.

Table of contents

List of tables

List of figures

1.0 Introduction

In the last century, semiconductor electronics and opto-electronics have devolved to a high volume, scaled-up, and industrial technology. High quality and precise dimensional control is the key to the success and prevalence of silicon-based electronics [85]. While silicon is still playing a dominant role in microelectronics, it approaches its fundamental limits as the size of the device scaling down. Therefore, the new generation of materials is continually being sought to supplement or replace silicon devices [25]. Nanofabrication in recent years enables the development of the integration of 2D materials in complex, integrated circuitry, as well as quantum confinement, which allows the study of fundamental physics.

Graphene is the first truly 2D single crystalline material with exotic electronic structure rather different from usual three-dimensional materials. It is well known that graphene was first isolated and transferred to another substrate from graphite which consists of hexagonal carbon sheets in 2004 by Konstantin Novoselov, Andre Geim, and their collaborators [58]. The Fermi surface is characterized by six double cones. For undoped graphene, the Fermi level situates at the connection points of these cones. The Fermi level can be changed by chemical doping or electric field thus the material is either n-doped (with electrons) or p-doped (with holes). At the Fermi level, the dispersion relations for both electrons and holes are linear, which corresponds to zero effective mass. The graphene excitations are identical to the Dirac equation for massless fermions, which travel at a constant speed and lead to the unusual quantum Hall effect in graphene. Besides, graphene is practically transparent. The optical absorption rate is only 2.3% of the light [53]. This number is given by $\pi\alpha$, where α is the fine structure constant. This unique property along with high conductance allows graphene to work as transparent gating material.

Besides graphene, a variety of 2D materials have attracted extensive interest due to its excellent properties and potential applications. The techniques of material growth with unit-cell allows the creation of atomically precise oxide heterostructures [28]. In 2004, Ohtomo and Hwang reported a high-mobility electron gas at interface between LAO and STO [61]. The strong electron-electron interactions [40] and complex band structures from d-orbitals [73]

gives rise to various physical properties in LAO/STO, such as superconductivity [68], magnetism [7], spin-orbit coupling [11] and electron pairing without superconductivity [17]. The LAO/STO interface has been found to exhibit "emergent" behavior such as metal-insulator transition [80] and magnetism [7]. The existence of conductance between two insulating materials raises many questions about the origin of conductance. The conductance is also found to be tunable with external electrical fields either globally with backgate [80] or locally with conductive atomic force microscope (c-AFM) tips. High-quality nanoscale devices can be sketched on the complex oxide interfaces reversibly [13].

This dissertation focuses on the integration of graphene and LAO/STO heterostructures, aiming to discover new physics from the interaction between these two fascinating 2D materials. Devices are processed by nanofabrication techniques and sketched with c-AFM lithography techniques. Transport and optical measurements are done at both room temperature and 2k to study the hybrid system's electronic and magnetic properties. Chapter 1 is an introduction to graphene and LAO/STO. Chapter 2 includes sample growth, device fabrication, and measurement techniques such as the c-AFM writing technique. Chapter 3 focuses on reconfigurable graphene/LAO/STO nano-devices. With c-AFM writing techniques, graphene can be doped to a different level by using LAO/STO as a local gating medium. Edge-state mixing is observed in the graphene p-n junction device. Rewritable doping patterns are also sketched with an STM tip in a graphene/LAO/STO heterostructure. Furthermore, the graphene superlattice is sketched by doping the graphene in nanoscale. Magnetotransport measurements are performed at T = 2 K. The measurement of the interface magnetism is studied on LAO/STO using the magneto-optical Kerr effect. Here graphene is used as a transparent gate for optical measurements. Experiment setup and preliminary results for Kerr imaging of LAO/STO magnetism are included. Coulomb drag is also performed in graphene/LAO/STO. The interaction between graphene and LAO/STO is studied in both graphene and LAO/STO under the superconducting region and quantum Hall region. The last chapter is the conclusion and outlook for the future.

1.1 Graphene

1.1.1 Graphene electronic properties

Graphene is made out of carbon atoms arranged in a hexagonal structure. It was first isolated by Novoselov *et al.* [58]. Since its discovery, graphene has attracted wide attention because of its unique electrical properties, such as very high carrier mobility [67, 58, 59, 66, 16], the room temperature quantum Hall [59, 66, 16, 36], and ambipolar electric field effect along with ballistic conduction of charge carriers [58].

The structure of graphene can be treated as a triangular lattice with a basis of two atoms per unit cell. The lattice vectors can be written as [57, 87]

$$\mathbf{a}_1 = \frac{a}{2}\left(3, \sqrt{3}\right), \mathbf{a}_2 = \frac{a}{2}\left(3, -\sqrt{3}\right), \tag{1.1}$$

With $a \approx 1.42$ Å is the lattice constant. The two points K and $K^{'}$ at the corners of graphene Brillouin zone(BZ) are named as Dirac points. In momentum space, their positions can be described as:

$$\boldsymbol{K} = \left(\frac{2\pi}{3a}, \frac{2\pi}{3\sqrt{3}a}\right), \boldsymbol{K}^{'} = \left(\frac{2\pi}{3a}, -\frac{2\pi}{3\sqrt{3}a}\right), \tag{1.2}$$

With tight bonding model, the Hamiltonian for electrons hoping to both nearest- and next-nearest neighbor can be written as:

$$H = -t \sum_{<i,j>,\sigma} (a^{+}_{\sigma,i} b_{\sigma,j} + \mathbf{H}.c.) - t' \sum_{<<i,j>>,\sigma} (a^{+}_{\sigma,i} a_{\sigma,j} + b^{+}_{\sigma,i} b_{\sigma,j} + \mathbf{H}.c.), \tag{1.3}$$

Where $a_{\sigma,j}(a^{+}_{\sigma,i})$ is the annihilation and creation operator for an electron with spin $\sigma(\sigma = \uparrow, \downarrow)$ on site R_i. t is the nearest-neighbor hopping energy and $t^{'}$ is the next nearest-neighbor hopping energy. The energy bands calculated from this Hamiltonian have the form:

$$E_{\pm}(\boldsymbol{k}) = \pm t\sqrt{3 + f(\boldsymbol{k})} - t^{'} f(\boldsymbol{k}), \tag{1.4}$$

$$f(\boldsymbol{k}) = 2\cos(\sqrt{3}k_y a) + 4\cos(\frac{\sqrt{3}}{2}k_y a)\cos(\frac{\sqrt{3}}{2}k_x a), \tag{1.5}$$

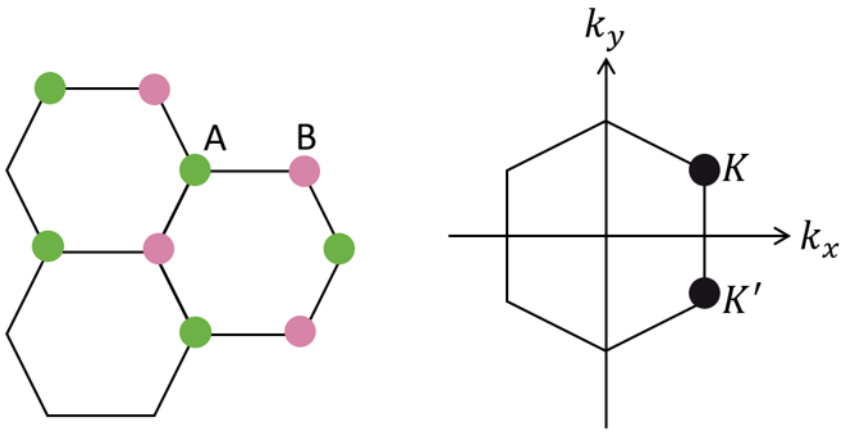

Figure 1: Left: honeycomb lattice structure of graphene. A and B denote the different sublattices. Right: Brillouin zone. K and $K^{'}$ represent Dirac cones.

Here the plus sign denotes to the upper and the minus sign denotes the lower band. For finite value of $t^{'}$, the electron-hole symmetry is broken and the upper and lower bands become asymmetric. Here we focus on the band structure close to one of the Dirac points, the dispersion can be obtained by expanding the full band structure. Close to the $\mathbf{K}$ (or $\mathbf{K}^{'}$) vector, as $\mathbf{k} = \mathbf{K} + \mathbf{q}$, with $|\mathbf{q}| << |\mathbf{K}|$,

$$E_{\pm}(\mathbf{q}) \approx \pm v_F|\mathbf{q}| \ + \ O[(q/K)^2], \tag{1.6}$$

Here $\mathbf{q}$ is the momentum measured relatively to the Dirac points and $v_F = 1 \times 10^6$ m/s is the Fermi velocity. The most significant between graphene and usual case, where $\epsilon(\mathbf{q}) = q^2/(2m)$, $v = k/m = \sqrt{2E/m}$ is the Fermi velocity doesn't reply on the energy or momentum. The expression of the spectrum near the Dirac point including $t^{'}$ up to second order in q/K is given by

$$E_{\pm}(\mathbf{q}) \approx 3t^{'} \pm v_F|\mathbf{q}| - (\frac{9t^{'}a^2}{4} \pm \frac{3ta^2}{8}\sin 3\theta_q)|\mathbf{q}|^2, \tag{1.7}$$

where

$$\theta_q = \arctan\frac{q_x}{q_y} \tag{1.8}$$

is the angle in momentum space. $t^{'}$ is the next nearest-neighbor hopping energy.

The Hamiltonian can be written as

$$\mathbf{H}(\mathbf{q}) = \hbar v_F \begin{pmatrix} 0 & q_x + iq_y \\ q_x - iq_y & 0 \end{pmatrix} = \hbar v_F \hat{\sigma} \cdot \mathbf{q} \tag{1.9}$$

The wavefunction around $\mathbf{K}$ in the momentum space has the form

$$\psi_{\pm,\mathbf{K}}(\mathbf{q}) = \frac{1}{\sqrt{2}} \begin{pmatrix} e^{-i\theta_{\mathbf{q}}/2} \\ \pm e^{i\theta_{\mathbf{q}}/2} \end{pmatrix}, \quad \psi_{\pm,\mathbf{K}'}(\mathbf{q}) = \frac{1}{\sqrt{2}} \begin{pmatrix} e^{i\theta_{\mathbf{q}}/2} \\ \pm e^{-i\theta_{\mathbf{q}}/2} \end{pmatrix}. \tag{1.10}$$

The wave function at $\mathbf{K}$ and $\mathbf{K}'$ are related by time-reversal symmetry: a reflection along the k_x axis. Also, if the phase θ is rotated by 2π, the wave function changes sign indicating a phase of π. Usually, this is called a Berry's phase in the literature.

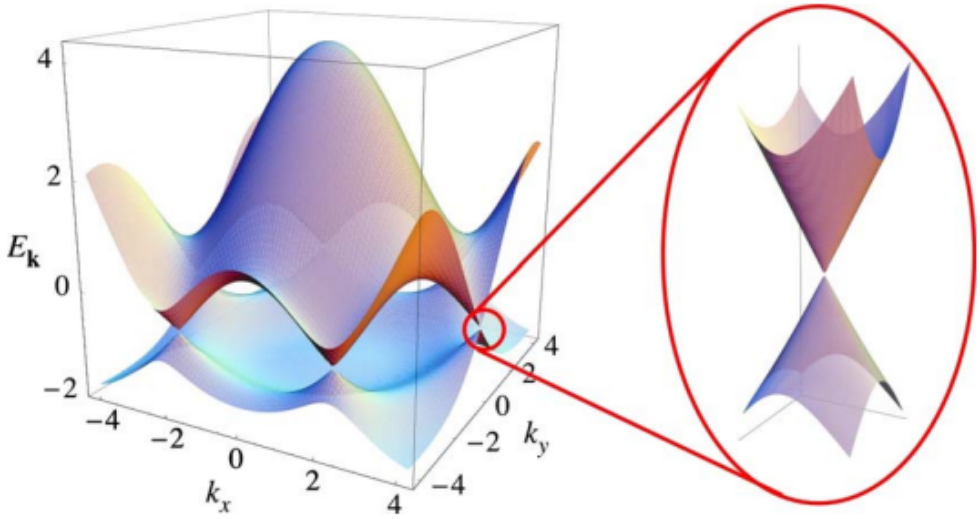

Figure 2: The band structure of graphene. The low energy approximation around $\mathbf{K}$ and $\mathbf{K}'$ has linear dispersion relation. The conduction and valence bands are gapless . The electrons behave like Dirac fermions. Adapted from [91].

1.1.2 Graphene quantum Hall

In a two dimensional conductor, if a voltage is applied in the plane, we expect to see the charge carriers accelerated in the direction perpendicular to their motion and end up to pile up along one side of the plane, leading to a voltage perpendicular to the current. This phenomenon is the Hall effect. In 1980 Klaus von Klitzing discovered a new behavior of the Hall effect at sufficiently low temperatures [45]. At certain ranges of a magnetic field, the Hall resistance exhibits plateaus at perfectly quantized resistance values.

In graphene, we keep the number of electrons fixed and vary the magnetic field perpendicular to the plane, in low temperature, the Fermi level of graphene will oscillate up and down as magnetic field varies. This can be understood as the vary of the Landau levels of the system. The period of the oscillation is found by setting the total number of electrons in the system equal to the number of states at the critical points,

$$N = \nu \frac{2eB_{crit}A}{h}, \tag{1.11}$$

Instead of fixing the total number of carriers, we could keep the magnetic field constant and vary the number of carriers by varying the gating of the system. The properties of the system do not merely oscillate. There are plateaus in the voltage measured in the perpendicular direction at the points where the number of electrons equals the number of states in an integer number of Landau levels. When the system is in these levels, the system's Hall resistance is equal to a constant,

$$R_H = \frac{\nu h}{e^2}, \tag{1.12}$$

Here ν is the number of Landau level filled and h and e are universal constants. This is known as the integer quantum Hall effect.

The low-energy band structure of graphene can be approximated as cones located at two inequivalent Brillouin zone corners 1. In these cones, the two-dimensional (2D) energy dispersion relation is linear. The electron dynamics can be treated as 'relativistic'. Landau-level (LL) formation for electrons in this system under a perpendicular magnetic field, B, has been widely studied experimentally and theoretically. To analyze the energy levels

of monolayer graphene in a magnetic field, one can substitute $\mathbf{q}$ in the Hamiltonian with $\mathbf{q} - e\mathbf{A} \equiv \pi$

$$\mathbf{H} = v_F \begin{pmatrix} 0 & \pi_x + i\pi_y \\ \pi_x - i\pi_y & 0 \end{pmatrix} \tag{1.13}$$

Note that $[\pi_x, \pi_y] = ie\hbar B_z$. If we set $\prod_i = l_B \pi_i / \hbar$, H^2 can be expressed as:

$$\mathbf{H^2} = \frac{\hbar^2 v_F^2}{l_B^2} \begin{pmatrix} \prod_x^2 + \prod_y^2 + 1 & 0 \\ 0 & \prod_x^2 + \prod_y^2 + 1 \end{pmatrix} \tag{1.14}$$

This is exactly a harmonic oscillator Hamiltonian with eigenvalues $\frac{\hbar^2 v_F^2}{l_B^2}(2|n| + 1 \pm 1)$ and $|n| = 0, 1, 2, ...,$, thus the eigenvalues are:

$$E_n = sgn(n)\sqrt{2e\hbar V_F^2 |n| B}, \quad |n| = 0, 1, 2, ... \tag{1.15}$$

Compared with the LLs obtained in conventional 2DEGs, there is a distinctive LL at $E = 0$ as the consequence of the electron-hole symmetry in graphene. The zero energy LL is formed equally from electron and hole states leading to a half-integer shift in the number of flux quanta needed to fill an integer number of LLs. The total degeneracy of each level is four, two from the spin degeneracy, two from the two Dirac cones (valley degeneracy). Thus the quantum Hall plateaus occur at the filling factors

$$\sigma_{xy} =^2 /h, \ \nu = 4(n + 1/2), n \in Z \tag{1.16}$$

1.2 Introduction to LAO/STO

1.2.1 STO symmetry breaking

LAO and STO compounds are well-known band insulating oxides with perovskite ABO structure. Lattice constant of LAO is $a = 3.791$ Å, while lattice constant of STO is $a = 3.905$ Å. At room temperature, the bandgap of LAO is 3.2 eV [30]. LAO is well known

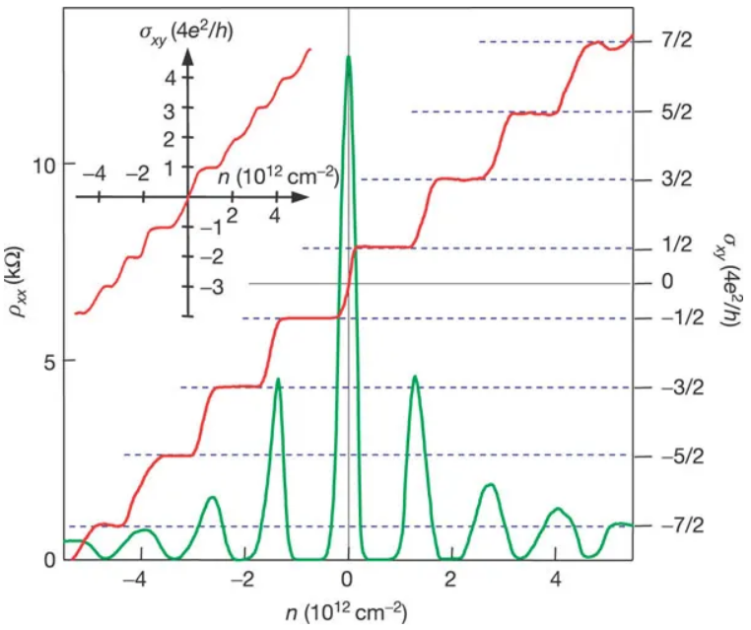

Figure 3: Quantum Hall effect in graphene as a function of charge-carrier density. Green line represents the longitudinal resistance. Red line represents the Hall conductance with $\sigma_{xy} = 4(n + 1/2)$. Adapted from [60].

as a functional dielectric in microwave superconducting resonators, filters and antennae, due to its relatively low losses at microwave frequencies [12] and high dielectric constant ($\epsilon_r \sim 24$) among other oxides. STO is a band insulator with a bandgap of $3.3 \sim 3.5$ eV, with a cubic perovskite crystal structure. As the temperature decrease, this cubic structure can be replaced by more efficient packing. At T = 105 k, neighboring oxygen octahedra rotate in the opposite direction while leads to a formation of tetragonal domains in STO. At even lower temperatures, a ferroelectric transition will occur. The dielectric constant can be $\epsilon_r \sim 20,000$ [72]. Moreover, STO is known to become superconducting at very low temperatures ($200 \sim 400$ mK), and is characterized by a very peculiar temperature vs. doping phase diagram characterized by a bell shape dome reminding those of High-Tc cuprates and pnictides. Superconductivity in STO is still not fully understood since it occurs in a range of electron doping more than three orders of magnitude lower than

classical BCS metallic superconductors. Finally, the symmetry breaking of spin space was not observed in bulk STO. However, ferromagnetism is reported in STO based heterostructures. More interestingly, this magnetism can coexist with superconductivity. All these mentioned symmetries can have mutual interplay thus make STO a very rich system.

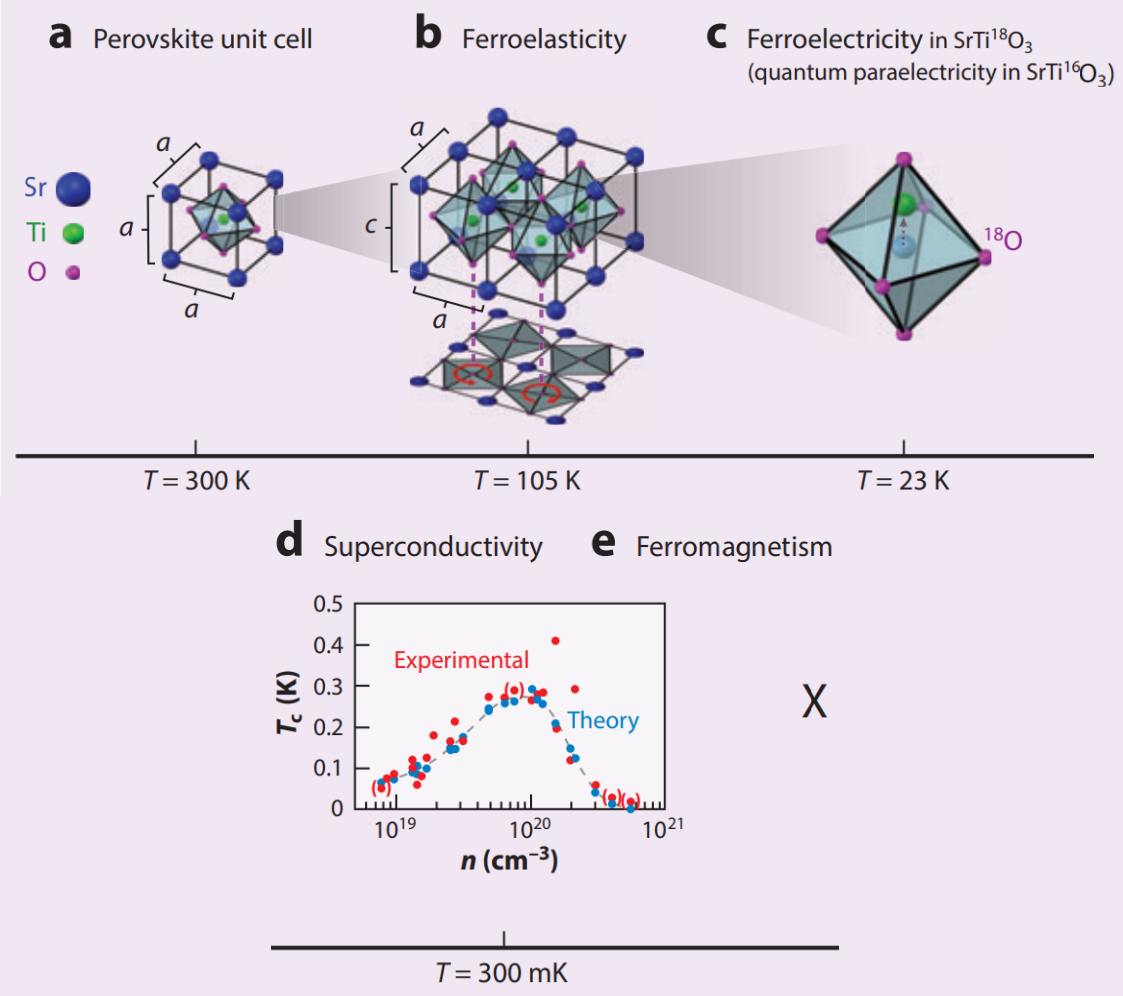

Figure 4: STO various symmetry breaking as the temperature is lowered. (a) cubic symmetry at room temperature (b) Below T = 105 K, a ferroelastic transition occurs. (c) At T = 23 k, a ferrolectric appears. (d) Near T = 300 mK, doped $SrTiO_3$ becomes a superconductor. (e) Bulk STO does not exhibit magnetism at any temperature. Adapted from [77].

1.2.2 STO electronic structure

Most of the physically observable quantities of complex oxide are stem from the electronic structure of STO. This system's low energy physics is mostly related to the fivefold-degenerate d orbitals of the titanium atom. The surrounding oxygen cage lifts the degeneracy. The levels split into a high-energy doublet (e_g states) and a low-energy triplet (t_{2g} states) that remains close to the Fermi level. The t_{2g} states are composed of the d_{xy}, d_{xz}, and d_{yz} orbitals. These orbitals couples to nearby titanium atom orbital through p orbitals of oxygen that lies between them. The hopping matrix elements are lager in plane than out of plane. As known in Figure 5(b), the hopping of d_{xy} orbital is stronger in x and y direction than in z direction.

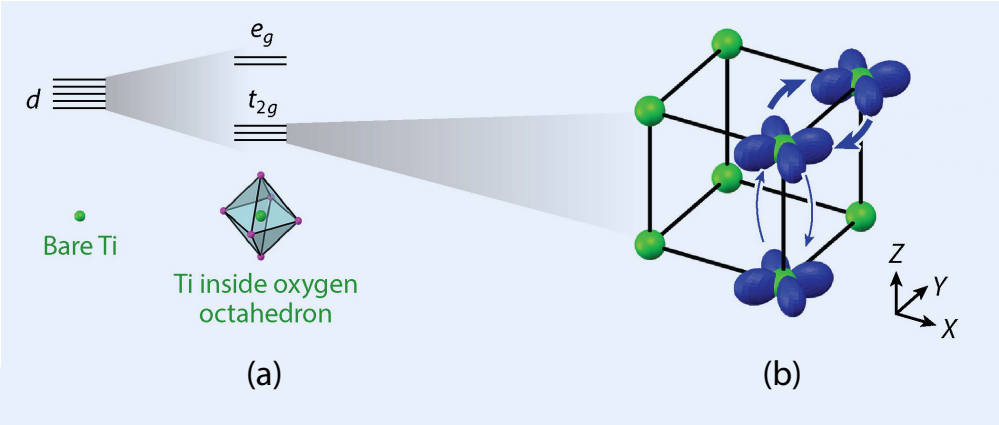

Figure 5: (a) Electronic orbitals near Fermi level are the fivefold-degenerate titanium d orbitals. The degeneracy of the orbitals is broken by the rotation of octahedral cage of oxygen atoms. The energy levels are lifted into e_g and t_{2g}. (b) The hopping of d_{xy} is much easier along in the plane directions, mediated by the $2p$ orbitals of oxygen atoms. Adapted from [77].

The Ti valence sate is mixed at LAO/STO, consists of Ti^{4+} from pure STO and Ti^{3+} from $LaTiO_3$. Using a two dimensional X-ray absorption spectroscopy (XAS) map (LAO-thickness versus photon energy, E), spectral features around the Ti L_3-edge is examined (Figure 6). The spectrum shows intense lines at both $E = 457.1$ eV and 459.4 eV, corresponding to the Ti t_{2g} and e_g orbital levels, respectively.

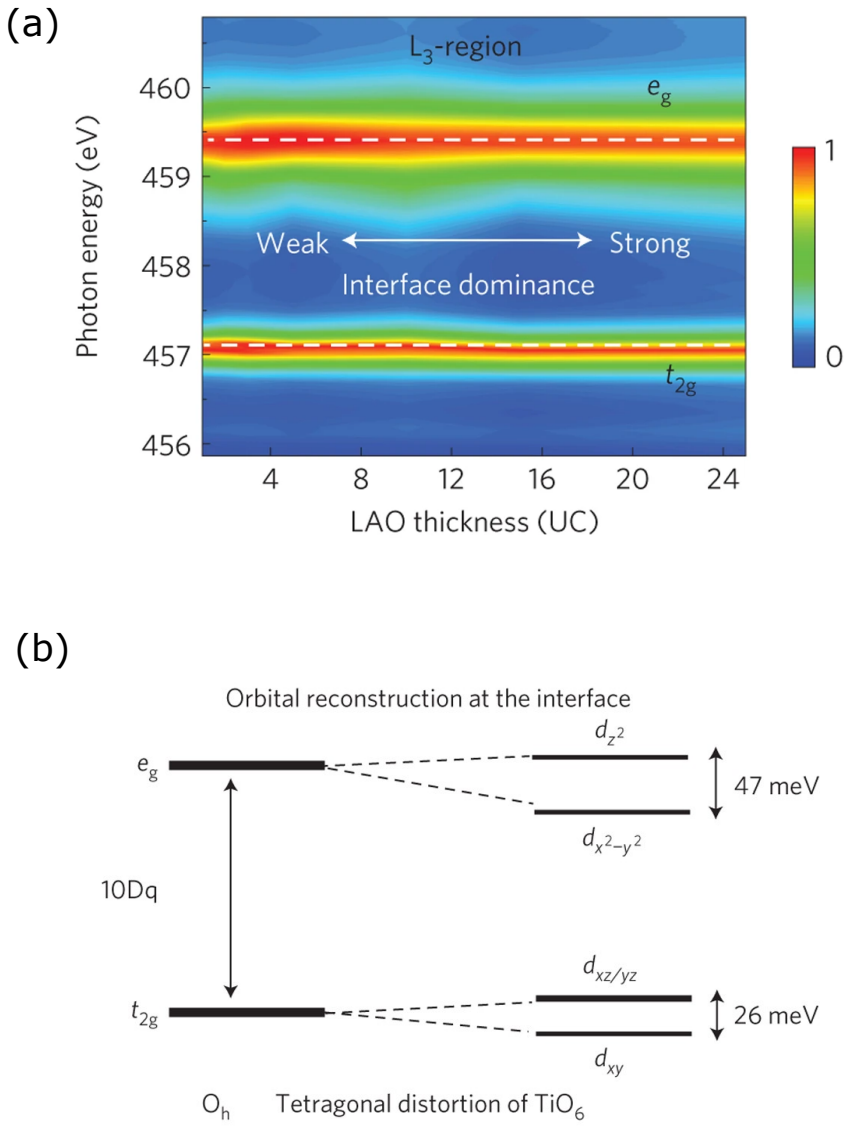

Figure 6: (a) Two-dimensional map of XAS spectra around the Ti L_3-region. (b) Schematic energy diagrams of the crystal field splitting and 3d orbital degeneracy. Adapted from [46].

A tetragonally distorted TiO_6 octahedron will lead to an energy splitting for both the degenerate t_{2g} and e_g orbital bands. The existence of such a distorted structure is verified by Ti L-edge X-ray absorption linear dichroism (XLD) measurements of the LAO/STO heterostructure [46]. The energy of planar orbitals (d_{xy} and $d_{x^2-y^2}$) in both the t_{2g} and e_g

bands is lower than that of the out-of-plane orbitals. The additional electron ($3d^1$) in the Ti^{3+} state occupies the polarized d_{xy} orbital level.

1.2.3 Metal-insulator transition and critical thickness

Both LAO and STO are band insulators, but the interface will become conducting when LAO (001) films are deposited on STO (001). This is first demonstrated by Ohtomo and Hwang in 2004 [61]. There are essentially two categories of possible theoretical approaches, one is based on the electronic reconstruction scenario and the other is based on extrinsic doping.

For the first explanation, in an ideal case, an electrostatic potential is accumulated at the interface. In the [001] direction, LAO can be regarded as a series of $La^{3+}O^{2-}$ and $Al^{3+}O_2^{2-}$ planes while STO a series of $Sr^{3+}O^{2-}$ and $Ti^{4+}O_2^{2-}$ planes. Thus, uncompensated charged LAO planes result in the build-up of the electric field on uncharged STO. This polarization will lead to an electric construction in the case of n-type (TiO_2 terminated $SrTiO_3$) interfaces. if 0.5 electron per u.c. is transferred from LAO surface valence bands (Oxygen $2p$ bands)to the STO conduction bands (Ti $3d$ t_{2g} bands), the polarcatastrophe can be avoided and the interface becomes conducting.

The observation of critical thickness for conductance can support the polar catastrophe mechanism well. However, there is a large discrepancy between the carrier density proposed by the polar catastrophe mechanism and measurement. In the polar catastrophe picture, each unit cell will donate half an electron and result in carrier density of 3.2×10^{14} cm^{-2}, while the observed values are in the order of 10^{13} cm^{-2}. One explanation is that there are two kinds of electrons, one is strongly localized with low mobility, while the other has higher mobility [29]. The low carrier concentration is also verified from Shubnikov-de Haas oscillations. Also, the formation of 2DEG on amorphous LAO on STO is contradicting to the polar catastrophe model.

Another explanation of the origin of 2DEG is oxygen vacancies [43]. The oxygen vacancies content is strongly dependent on the background oxygen pressure used during the deposition. Usually, high oxygen pressures ($> 10^3$ mbar) produce insulating or barely conducting films.

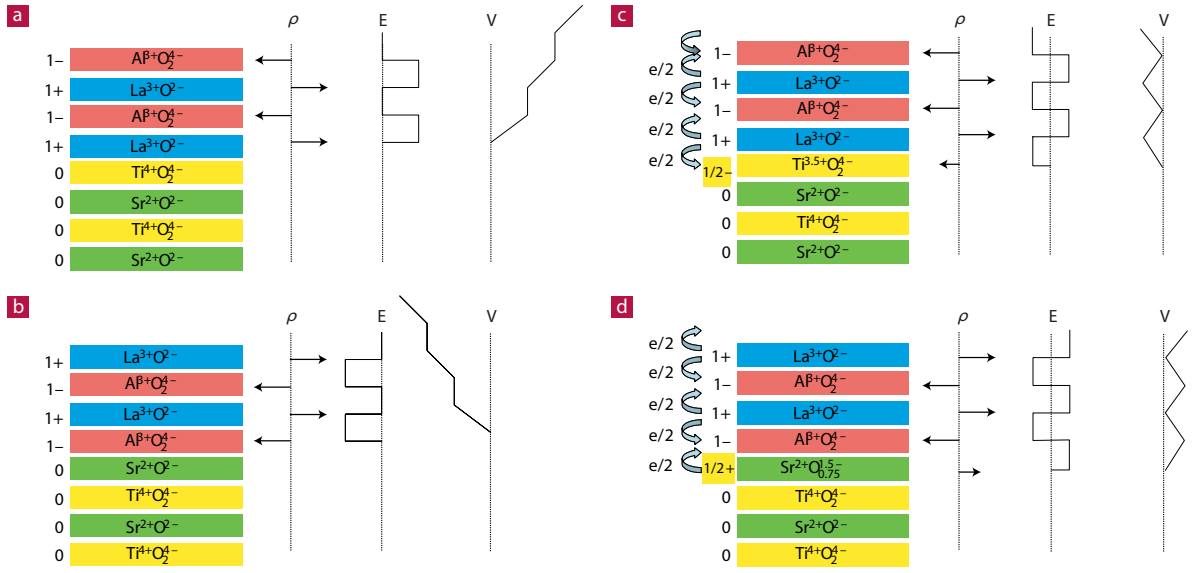

Figure 7: Polar catastrophe mechanism. (a) $La^{3+}O^{2-}$ and $Al^{3+}O_2^{2-}$ are polarized. A non-zero potential is built up when LAO is grown on TiO_2 terminated STO. (c) Electrons are transferred from LAO to STO to compensate the potential. A conducting 2DEG is formed. (b) and (d) are similar mechanism for the hole gas on the interface. Adapted from [54].

The growth of the LAO/STO sample under different oxygen partial pressure shows that the carrier density is correlated to P_{O_2}. Oxygen vacancies can also be the origin of magnetism. However, oxygen vacancies can't explain the critical thickness.

The metal-insulator transition was first reported by Thiel et al in 2006 [80] at LAO/STO interface when the thickness of LAO is above 4 uc. In Figure 8, the conductance is zero when the thickness is under 4 unit cells. About 4 unit cells, the conductance increases dramatically. At critical thickness, the interface conductance is tunable by gating voltage. As in Figure 3, when $V = 100$ V is applied to backgate, the interface becomes conducting. The conductance will persist when the positive voltage is removed. However, when $V = -100$ V is applied to backgate, the conductance drops to zero.

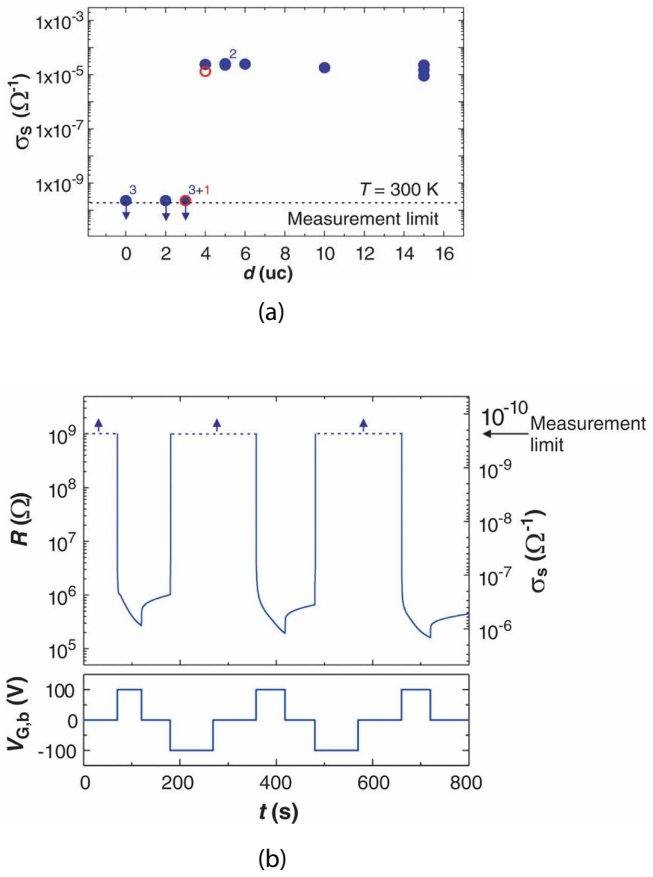

Figure 8: Critical thickness of LAO/STO. Top: When LAO is above the critical thickness, the interface is conducting. The as-grown LAO is insulating when the LAO thickness is below the critical thickness. Bot: The conductivity can be tuned with backgate. When +100 V is applied to the backside of the sample, the interface becomes conductive. When the voltage is removed, the conductivity can persists for some time. When 100 V is applied, the interface becomes insulating again. The conductivity can be tune reversibly by applying backgate voltage [80].

1.2.4 c-AFM lithography of 2DEG and the "water-cycle" mechanism

More interestingly, the conductance of the LAO/STO interface can be tuned locally by the conductive AFM lithography technique(c-AFM). For a 3.4 uc LAO/STO sample, the

thickness of LAO is below critical thickness, the interface is not conducting. By applying positive voltage to a nanoscale AFM tip, characteristic conducting features as small as 2 nm can be created at the interface. This process is reversible. By applying a negative voltage to the tip, the nano-features can be restored to the insulating state again. The tunability can be explained by the "water-cycle" mechanism [5]. The water adsorbed onto the LAO surface is dissociated into OH^- and H^+. When a positive voltage is applied to the tip, OH^- will be removed and only excessive H^+ will be left on the LAO surface. H^+ will then attract electrons from STO and make the interface conductive. The water cycle mechanism is verified by the control c-AFM writing experiments performed in a vacuum. In the vacuum atmosphere, the writing process can't accomplish since water is absent.

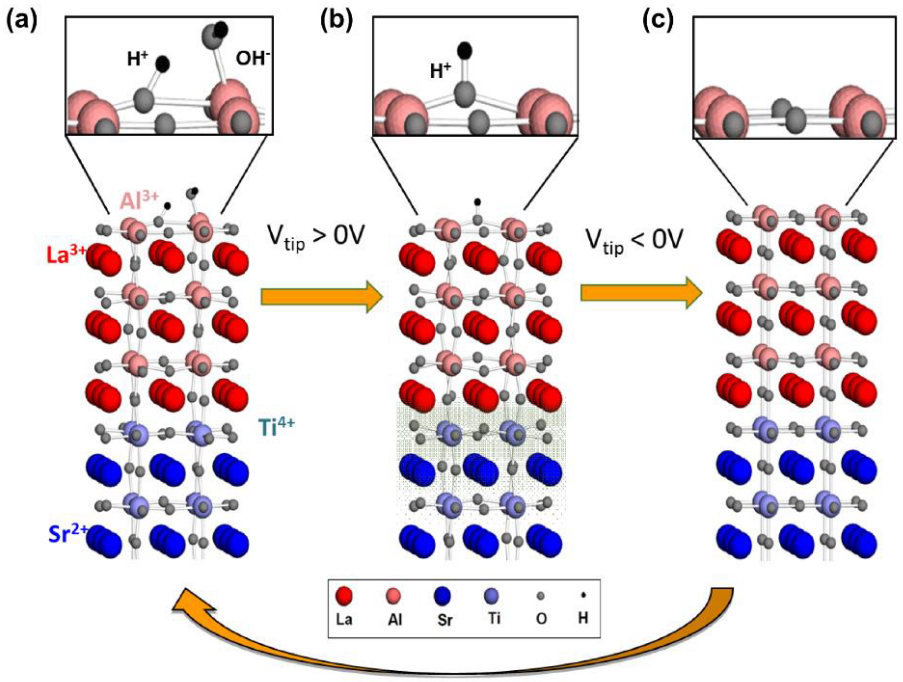

Figure 9: The "water cycle" mechanism. When a positive voltage is applied to c-AFM tip, the OH^- bond can be removed and excessive H^+ are left on LAO surface, which will induce 2DEG at the interface. When a negative voltage is applied to c-AFM tip, the H^+ bond will be removed thus restore the OH^-–H^+ balance, Adapted from C. S. Hellberg's APS talk [91].

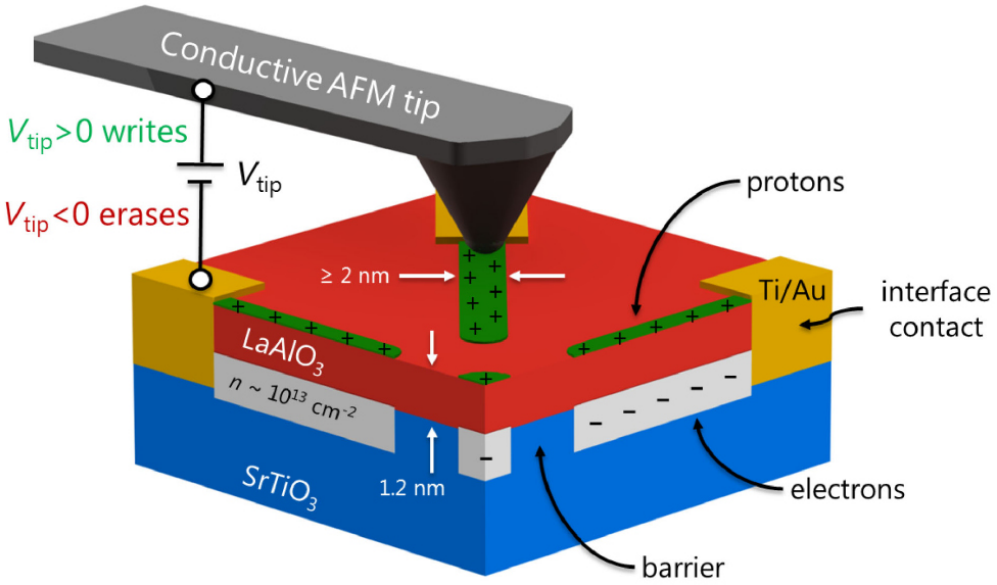

Figure 10: Conductive region can be created at LAO/STO interface with positively bias conductive AFM tip. Water molecules dissolve into protons and hydroxides. Protons act as topgate and attract electrons from interface thus make the interface conducting. Naonstructures can be as small as 2 nm. Adapted from [63].

2.0 Experimental methods

2.1 Sample growth

2.1.1 LAO/STO growth

A variety of techniques are used to grow LAO/STO heterostructures, including pulsed laser deposition(PLD), molecular beam epitaxy(MBE), laser MBE, hybrid MME and sputtering [8]. Our samples are grown by collaborators, Sangwoo Ryu, HyungwooLee, Jung-Woo Lee, Kitae Eom, and Chang-Beom Eom, at the University of Wisconsin-Madison.

STO is used extensively as a substrate for the fabrication of various oxide materials. STO(001) substrates are purchased from commercial crystal suppliers. The mis-cut angle is smaller than 0.1°, so the LAO/STO terrace's width is about 500 nm. Later pulsed laser deposition allows materials to grow layer-by-layer with atomic precision. In order to achieve this precision, an atomically flat substrate with TiO_2 termination is essential. A TiO_2 can be achieved by using a buffered HF solution. The substrate is then subjected to a high temperature at 1000° in an oxygen atmosphere for several hours.

In the PLD process, a KrF 248 nm laser is directed at a target. The target material is ablated due to the local heating and form plasma. The plasma expands and deposits on the substrate. During the PLD growth reflection high-energy electron diffraction (RHEED) is used for monitoring the growth. For 3.4 u.c LAO/STO, the STO substrate is heated at 550 °C and chamber oxygen pressure is maintained at 1×10^{-3} mbar. After growth, the sample is annealed in 1 atm of O_2.

2.1.2 Graphene growth

Graphene is mainly obtained by two methods: exfoliation and CVD-grown method. The size and shape of exfoliated graphene can't be well controlled. To get large-scale graphene and later etch to the desired pattern, we adopted the CVD method. Our graphene is in collaboration with Shonali Dhingra, Jen-Feng Hsu, and BrianD'Urso from University of

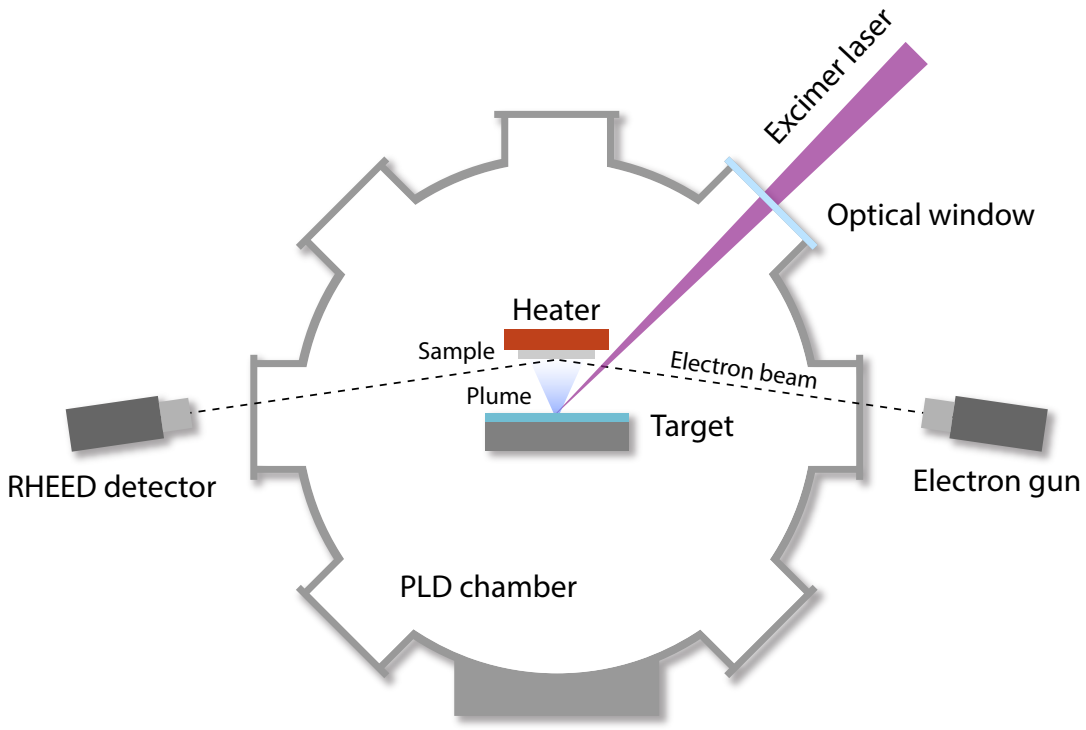

Figure 11: PLD epitaxial growth. The PLD chamber is backfilled with oxygen to the target pressure. A beam of pulsed-deep-UV excimer laser is focused onto the LAO target. LAO is ablated off, and a plume of plasma extending towards the heated substrate on top and condensed into atomic layer films. RHEED signal is used to monitor the thickness of LAO. Adapted from [47].

Pittsburgh. The growth parameters are from Shonali Dhingra'sPh.D. dissertation [23].

The CVD process uses gaseous organic molecules (methane, ethylene, etc.) as carbon sources. In high temperature (1000 °C, the metal surface is highly reactive and can catalyze graphene formation. CVD is a dynamic process of etching and growth. The domain is forming and being etched away at the same time. [86, 94] The growth terminates until the domains are in contact with each other or the gas flow is stopped. With high hydrogen portion, the larger graphene domains will also be etched. The ratio of methane and hydrogen need to be carefully controlled.

2.1.3 Copper substrate preparation

Many materials can be used for graphene growth, such as SiC, Cu, Ir, and Ni. Among them Cu is the most commonly used one [2]. In CVD growth, the carbon atoms form into graphene deposits on the copper substrate. Aside from the intrinsic wrinkles on graphene due to thermal fluctuations [52], the initial roughness of the copper substrates can get added to graphene. The roughness of copper will directly digress graphene quality. Surface contaminants on copper provide nucleation centers for graphene and can cause polycrystalline structure and multi-layer growth [27]. The copper surface can be cleaned and flattened with electrochemical polishing [2] or mechanical polishing. In this work, graphene substrate is polished using procedures developed by Shonali Dhingra, Jen-Feng Hsu from Dr. Brian D'Urso's group in University of Pittsburgh. The roughness of the copper substrate is reduced to a few nanometers [23] by using a diamond turning machine (DTM). This method can greatly increase copper domain sizes are five times larger [24]. By reducing the incremental step to 10 μm, the finishing surface's roughness can be smaller than 2 nm.

Other than surface roughness, the copper domain size is another limiting factor for sizeable single domain graphene growth. Although it was not clear the effect of copper substrate domains on the graphene quality [44, 88, 92], larger copper domain sizes give us a chance to grow larger graphene single crystals. Annealing the copper at high temperature will reconstruct and merge the polycrystalline domains into larger domains, but mechanical processing will introduce defects and break the single domains; therefore the substrate needs

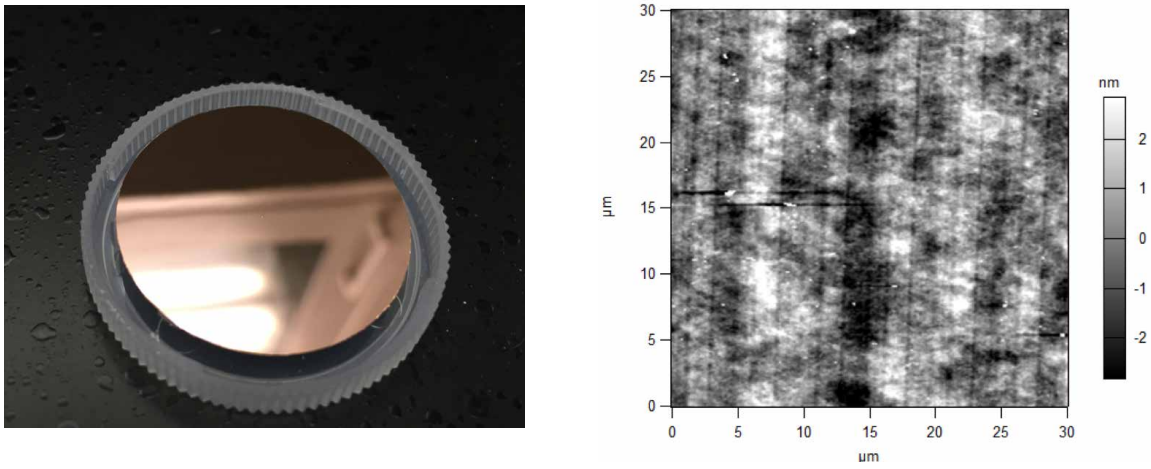

(a) (b)

Figure 12: (a) The copper surface after DTM polishing. The final thickness of the substrate is about 100 μm. (b) The AFM image of the copper foil surface. The roughness is within 2 nm. Adapted from [47].

to be re-annealed before graphene growth starts. Oxygen-free high thermal conductivity copper (OFHC) rods with purity (99.99%) are purchased from McMaster Carr. The rod is first annealed at $T = 1050°$C for 24 hours, and the polycrystalline domains in the rod will merge into larger domains within. Then the rod is then cut into copper discs of 2 mm thick in the machine shop. The mechanical cutting process will break the domains and introduce surface contaminant. The surfaces copper discs are cleaned on the DTM, and then annealed again at 1050 °C for 8 hours. After annealing, the domain re-formation in the disc will cause corrugation on the surface. Therefore, the copper surface is polished with DTM for a second time. Then the copper discs are cut into 100 μm foils, by 10 μm steps.

The CVD graphene growth is performed in LPCVD or atmospheric pressure (APCVD). LPCVD grows requires higher growth temperature. The copper might evaporate and contaminate the furnace. Thus we adopt the APCVD method, following the recipe from [24].

- Pump down the furnace to 5∼15 mTorr.

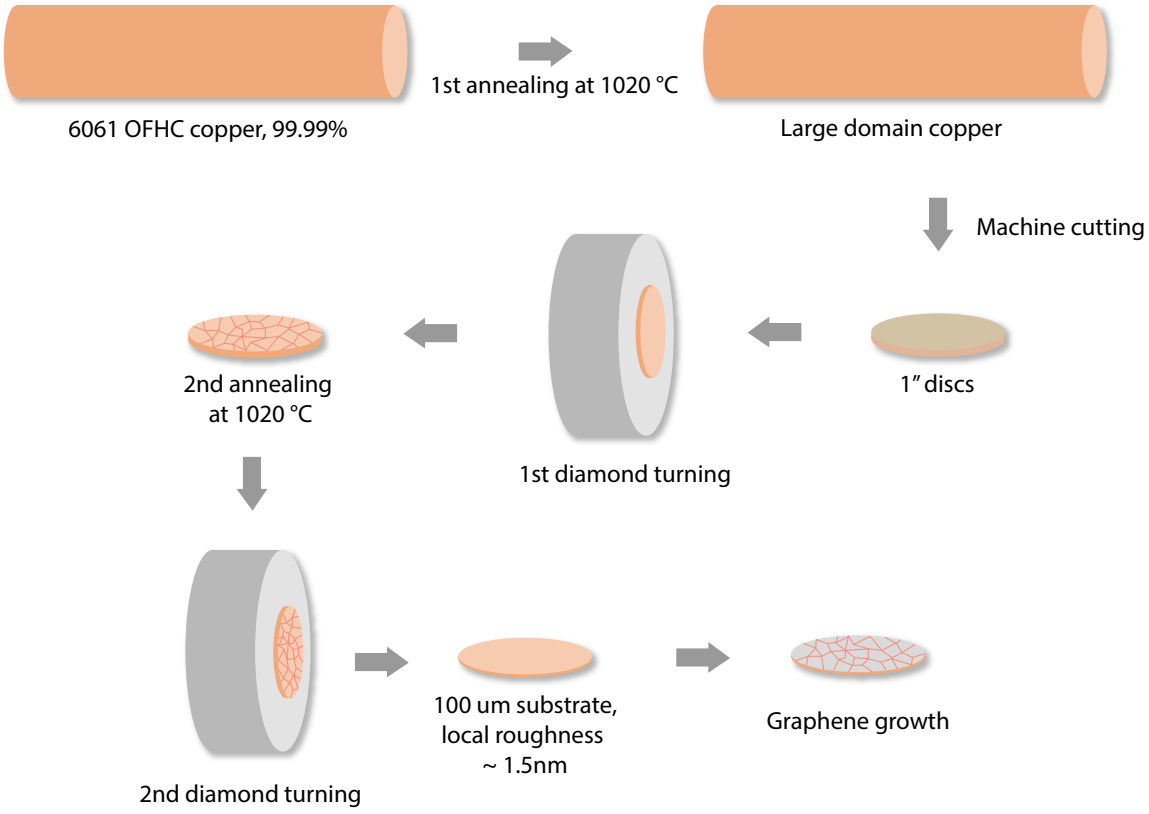

Figure 13: Processing copper rods into 100 μm foils for graphene growth. Copper rod is first annealed at 1050 °C for 24 hours to form larger domains. Then the rod is cut into 2 mm thick copper discs. The discs are polished with DTM. Second annealing is done at 1020 °C. Thus, the copper disc surface is polished again with DTM to be cut into 100 μm foils. Adapted from [47].

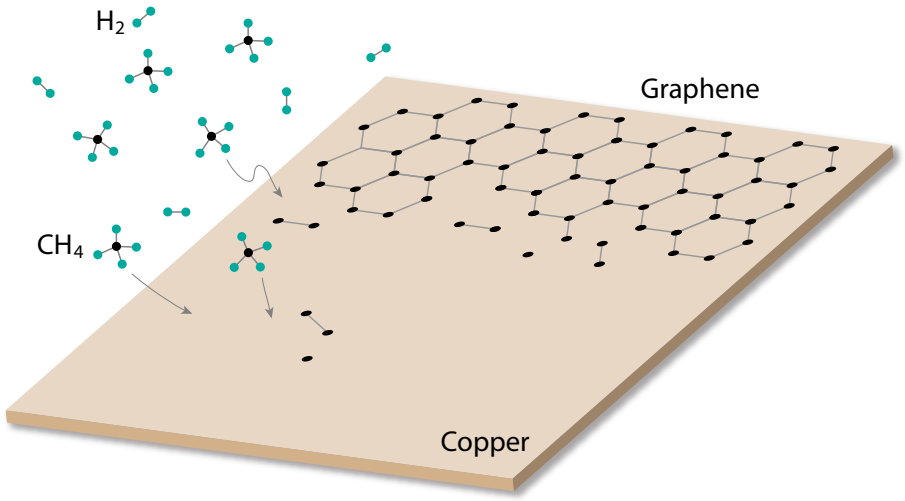

Figure 14: Graphene CVD growth. At a temperature $T \approx 1000$ °C, methane molecules will react with copper and leave carbon atoms on the surface. The atoms will self-assemble into seperate graphene domains. Hydrogen is used to etch away the smaller domain so that the final single layer graphene domains are as large as possible. The large domains would concatenate with each other and finally become one entire piece of graphene. Adapted from [47].

- Flowed 70 sccm of H_2/Ar mixture. The pressure would rise to 280 mTorr.
- Ramp the furnace up to 1000°C (941°C on the furnace controllerThe temperature on controller monitor has a discrepancy with the actual temperature.). Stay at this temperature for 8 hours.
- Cool down the furnace to room temperature. Close off the gas mixture at room temperature. This process takes a whole night.

AP Growth is as follows:

- Pump down the furnace to 5∼15 mTorr.

- Flow 186 sccm of H_2/Ar mixture (flow rate does not matter. We were using two MKS MassFlo Controller. The maximum allowed flow rate for each controller is 100 sccm. The clamp on the exhaust will fall off when the pressure in the furnace reaches the atmospheric pressure.
- Start the growth program on the furnace controller. Since the AP Growth is done quite close to the melting point of copper, this program contains three steps to prevent overshooting of temperature. The temperature is firstly ramped-up to $\sim$ 1000°C (953°C on furnace controller) at a rate of 10C/min; it is then taken slowly up to $\sim$ 1035°C (983°C on furnace controller) at a rate of 2°C/min; finally it is ramped up to $\sim$ 1050°C (998°C on furnace controller) at a rate of 1°C/min. The furnace then stayed at this temperature for 2.5 hours.
- After 2.5 hours, we flow 14 sccm of CH_4/Ar mixture into the tube. The growth persists for the remaining 1.5 hours. The pressure is 86$\sim$88 mTorr during this stage.
- Cool the furnace down to room temperature. CH_4/Ar gas mixture is turned off after the furnace cooled down to $\sim$ 650°C. H_2/Ar is flowing overnight until the temperature is close to room temperature.

Table 1: Copper annealing program

	stage 1	stage 2
Temperature ramping rate	10 °C/min	20 °C/min
Final temperature	941° C	20° C
Persist time	8 hr	0 hr

2.2 LAO/STO sample processing and graphene patterning

Nowadays mechanically transferred exfoliated graphene encapsulated with hexagonal boron nitride (h-BN) [21] is widely used for high-quality graphene device fabrication. The

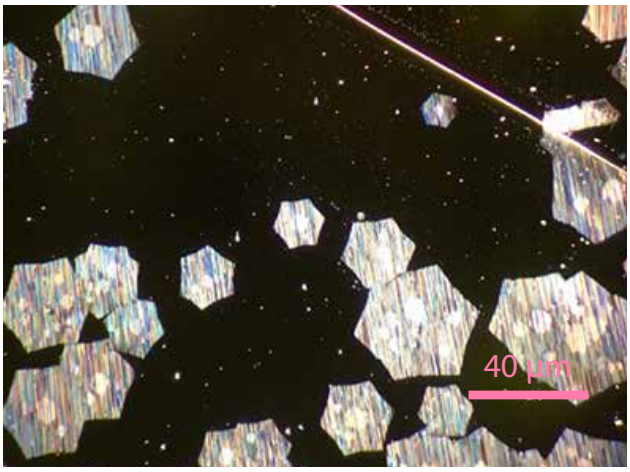

(a)

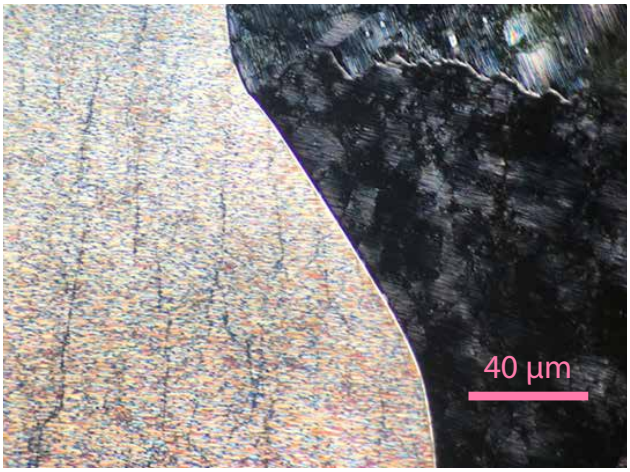

(b)

Figure 15: Dark field mode microscope images of CVD graphene on copper substrates. (a) The copper substrate is partially covered with graphene. Hexagonal shape single domain graphene can be observed. Growth is terminated before graphene entirely covered the substrate. (b) Graphene covers the entire copper substrate. Copper domains of two different orientations can be observed.

mobility of these devices can be as high as $35,000$ $\mathrm{cm^2V^{-1}s^{-1}}$ at room temperature. However, to get arbitrary size and shape of graphene, CVD grown graphene with wet transfer-

Table 2: Graphene growth program

	stage 1	stage 2	stage 3	stage 4
Temperature ramping rate	10 °C/min	2 °C/min	1 °C/min	20 °C/min
Final temperature	953° C	983° C	998° C	20° C
Persist time	0 hr	0 hr	4 hr	end

ring is preferred. In the wet transfer, a spin-coated polymer layer protects graphene while the metallic growth substrates such as Cu is completely etched away by soaking protection-layer/graphene/substrate stack in etchants such as nitric acid, hydrochloric acid (HCl), ferric chloride ($FeCl_3$) or ammonium persulfate (AP). The protection layer is finally removed with an organic solvent.

Usually, Polymethyl methacrylate (PMMA) is used as a protection layer. However, persistent PMMA residue formed during a graphene transfer has been a limitation in optimizing graphene device performance. Our collaborator Dr. Brian D'Urso proposed a replacement of PMMA: Hyflon, which can effectively reduce the contaminants. Hyflon is a type of perfluorinated polymer and is highly hydrophobic and chemically inert. It has been used as protective coatings, interlayer dielectric films and pellicles for electronic membranes.

There are mainly two types of Hyflon available, Hyflon AD 40 and Hyflon AD 60. These two amorphous perfluoro-polymers are in powder form, only soluble in a few types of perfluorinated solvent. Hyflon AD 40 and Hyflon AD 60 have different molecular weights and glass transition temperature. Based on empirical evidence, we choose Hyflon AD 60 since Hyflon 60 is easier to be removed in the cleaning procedure.

.

2.2.1 Graphene wet transferring

Hyflon AD 60 solvent is made by 2.5 grams Hyflon powder dissolved in 100 ml FC- 40. The solution is well shaken for 48 hrs at 100 rpm. Hyflon solvent is then filtered with a

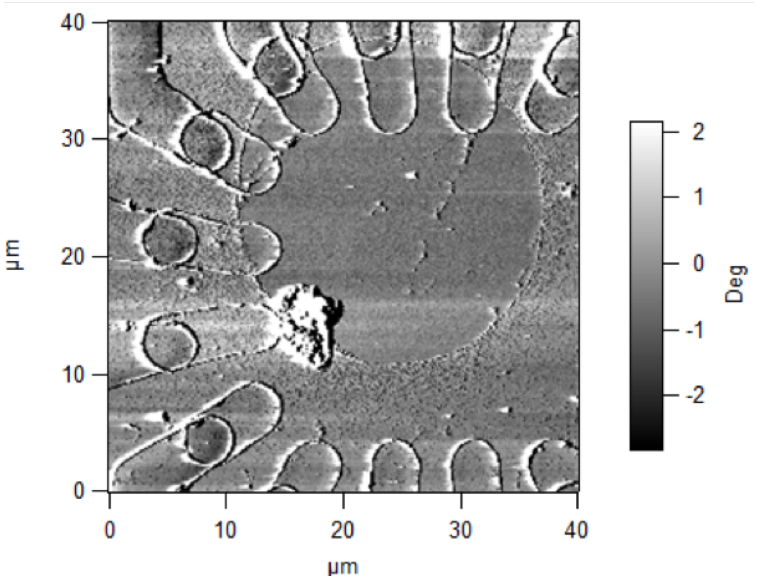

Figure 16: AFM phase image of circular graphene on LAO/STO. Graphene is transferred with PMMA. Residuals can be found outside the graphene region. Adapted from [47].

series of filters with pore size 450 nm, 200 nm, 100 nm to remove residues. Graphene is grown on 100 um thick circular copper film with 2 cm radius. LAO/STO substrate is 5 mm × 5 mm square. To fully cover the LAO/STO substrate, we need to cut graphene/copper foil into 6 mm × 6 mm squares with a blade, as shown in Figure 21. The domains of graphene are visible. The small copper film piece is stuck to a 3" inch wafer with tape. The tape should firmly cover the edge of the copper film to prevent Hylfon contaminating the backside of copper. Otherwise, the backside of copper would be covered by Hyflon, which cannot be dissolved by copper enchant-ammonium persulfate. Hyflon residue will attach to the backside of graphene after copper dissolving. This should be avoided.

The transferring process with Hyflon is similar to the PMMA transfer method. We stick the graphene/copper piece with wafer by tape. Hyflon is then spin-coated on top of graphene. With a spin coating speed of 3500 rpm, the thickness of Hyflon is 50 nm. Hyflon/graphene/copper is etched with RIE to make Hyflon hydrophilic so later we can spin coat AZ4210 on top of Hyflon. Based on our experience, the whole transfer process

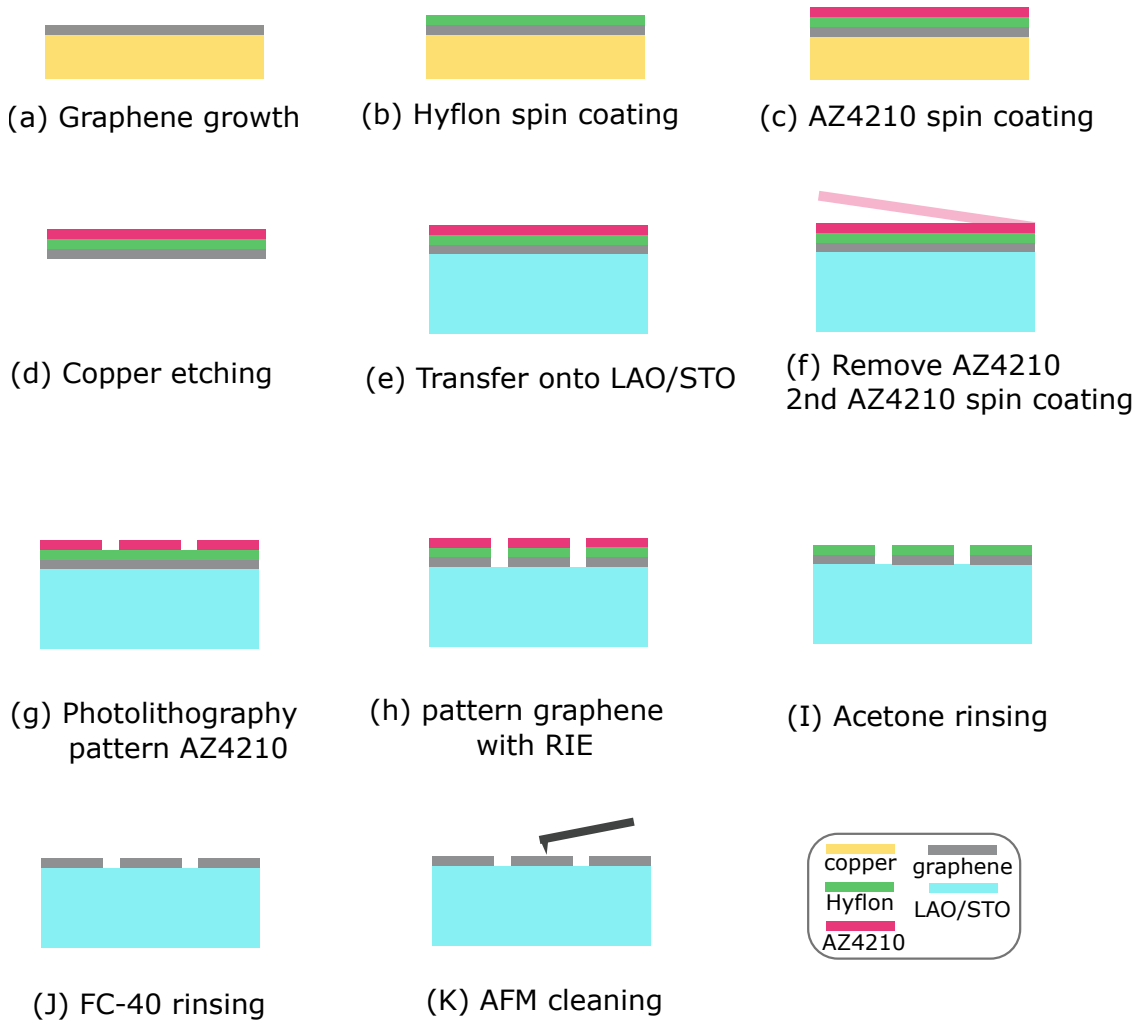

Figure 17: Hyflon transfer and patterning procedure. (a) graphene is grown with CVD on a copper substrate. (b) Hyflon is spin-coated on graphene. (c) photoresist is added to Hyflon as a supporting layer. (d) The copper substrate is etched away with ammonium persulfate; graphene is rinsed in DI-water for several times. (e) graphene is transferred onto the LAO/STO substrate. (f) Photoresist for transfer assistance is removed; another layer of photoresist for photolithography is coated. (g) Standard UV photolithography. (h) Oxygen plasma etching. (i)Remove photoresist with acetone. (j) Remove Hyflon with FC-40. (k) AFM cleaning with contact mode scanning.

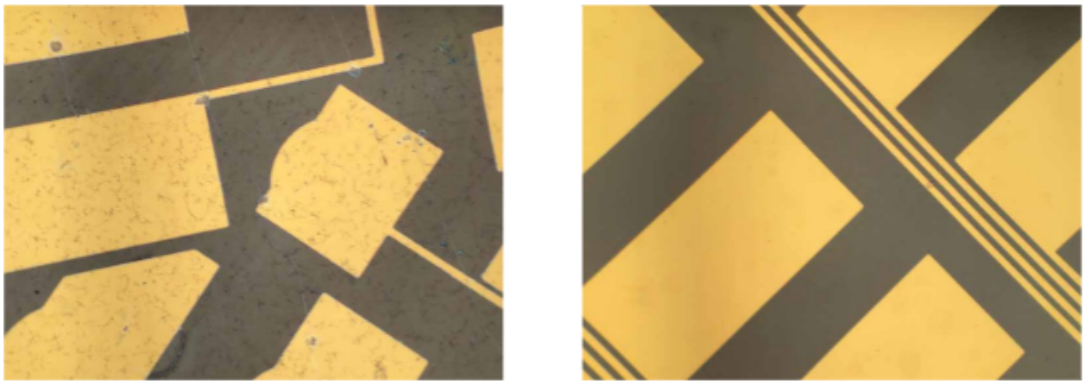

Figure 18: (a) Without copper substrate backside cleaning, the graphene transferred onto LAO/STO has contaminants trapped. (b) The graphene on LAO/STO is much cleaner if the backside is cleaned. Adapted from [47].

can be done without this AZ4210. However, this additional AZ4210 layer can provide better mechanical support for Hyflon/graphene. This reduces the failure rate. After the AZ4210 spin coating, we take AZ4210/Hyflon/graphene/copper off from the silicon wafer and carefully cut the piece's edge to get a slightly smaller piece. The piece is placed on an ammonium persulfate solvent, floating on it. After 4 hours, the copper is fully dissolved, only leave AZ4210/Hyflon/graphene piece floating on top of the solvent. We scooped the AZ4210/Hyflon/graphene piece out with Teflon mesh and rinsed it in clean water four times. The LAO/STO substrate is then immersed into water and scoop the AZ4210/Hyflon/graphene piece from its bottom. The AZ4210/Hyflon/graphene will stay on top of LAO/STO with a water bubble in between. This bubble can be eliminated by heating the sample on a heat plate at 75° for 10 min.

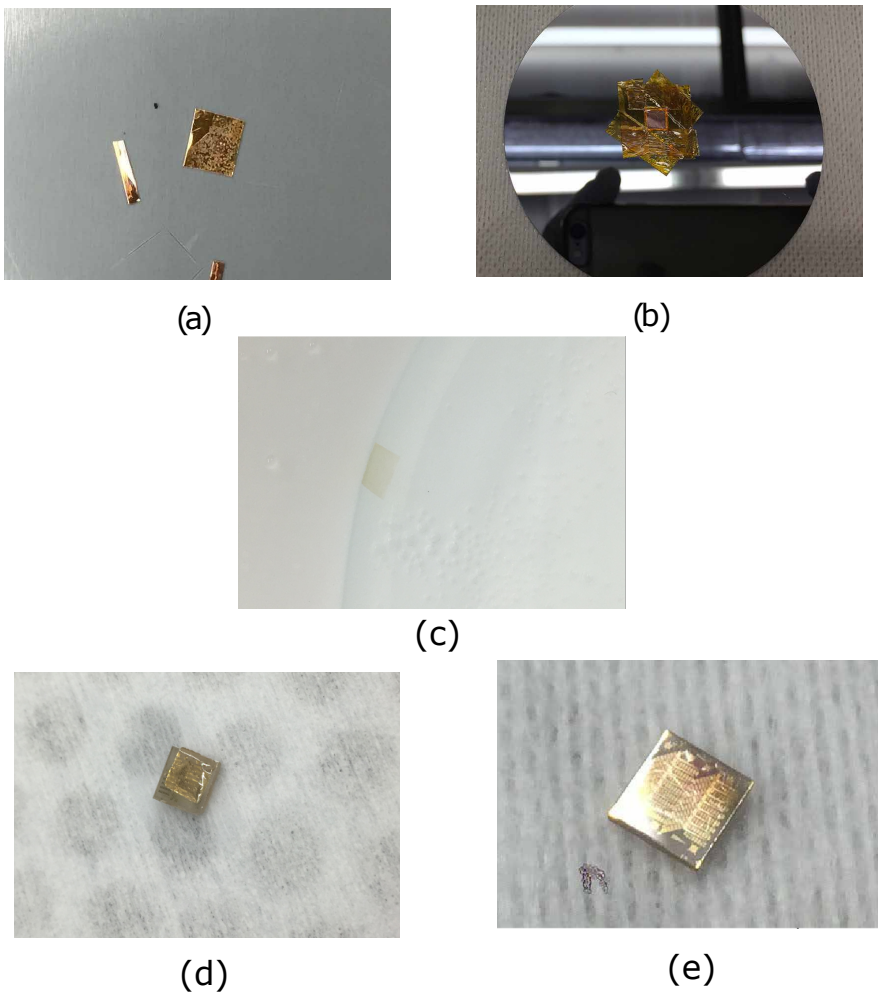

Figure 19: (a) The graphene with copper foil is cut into squares. The top side and backside of copper piece can be distinguished by color. The top side is darker. (b) Copper foil with CVD graphene is fixed onto a silicon wafer as a spin-coating carrier. The edges of the copper foils are covered with tape to prevent Hyflon solution contamination. (c) The graphene flake with Hyflon and photoresist floats on the surface of water.(d) Water bubble between graphene and LAO/STO is visible. (e) Graphene transferred onto pre-patterned LAO/STO. Water between the graphene LAO is evaporated on a hot plate set to 75 °C.

2.2.2 Graphene/LAO/STO photolithgraphy and etching

The transferring process with Hyflon is similar to the PMMA transfer. The graphene is patterned with standard UV photolithography. Graphene Hall har is protected by photoresist and the exposed regions are developed. The contaminants introduced by wet-transferring can be removed by RIE process.

For each sample, there are 16 graphene Hall bar devices on it. The size of each device is about 30 um × 30 um. The sample size is 5 mm × 5 mm. So the graphene Hall bar is only a small portion of the sample. We need to etch most of the graphene away. With such large graphene pieces, multiple layers of graphene, especially at the sample edge, are inevitable. A more powerful RIE process outside the devices is desirable to avoid a short on bonding pads. So we divided this photolithography into two steps. The first step is to etch graphene into 16 squares with aggressive RIE that covers all devices on one sample. The second step is to further etch these squares into a Hall bar structure with moderate power.

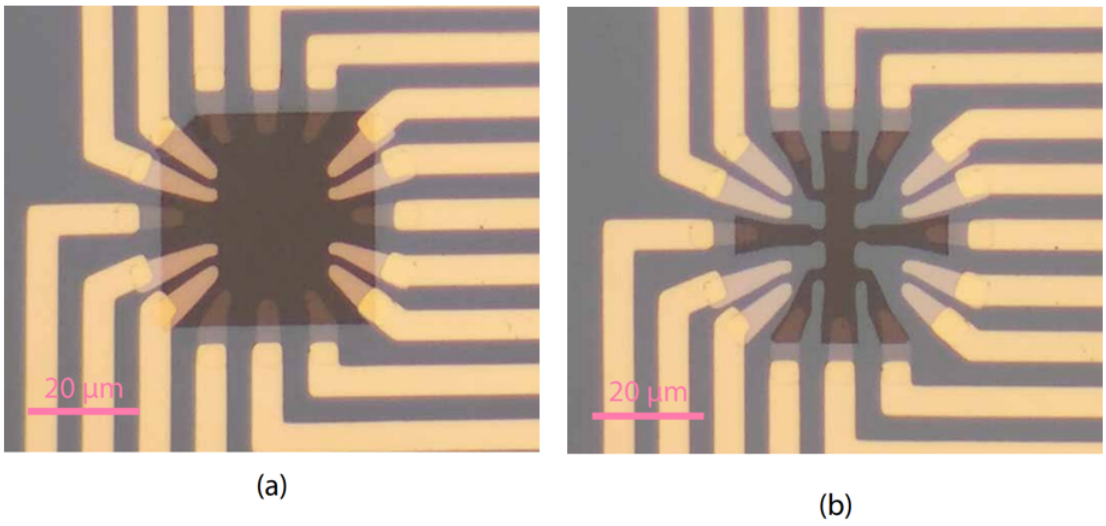

Figure 20: Two-step graphene etching. (a) A square shape region is protected by AZ4210 photoresist. The Outside region is etched with an aggressive RIE recipe to remove the contaminants introduced by wet-transfer. (b) A Hall-bar shape region is protected by AZ4110 photoresist. The Outside region is etched with an mild RIE recipe. Adapted from [47].

Right after the wet-transferring, the mechanical supporting AZ4210 is washed off by

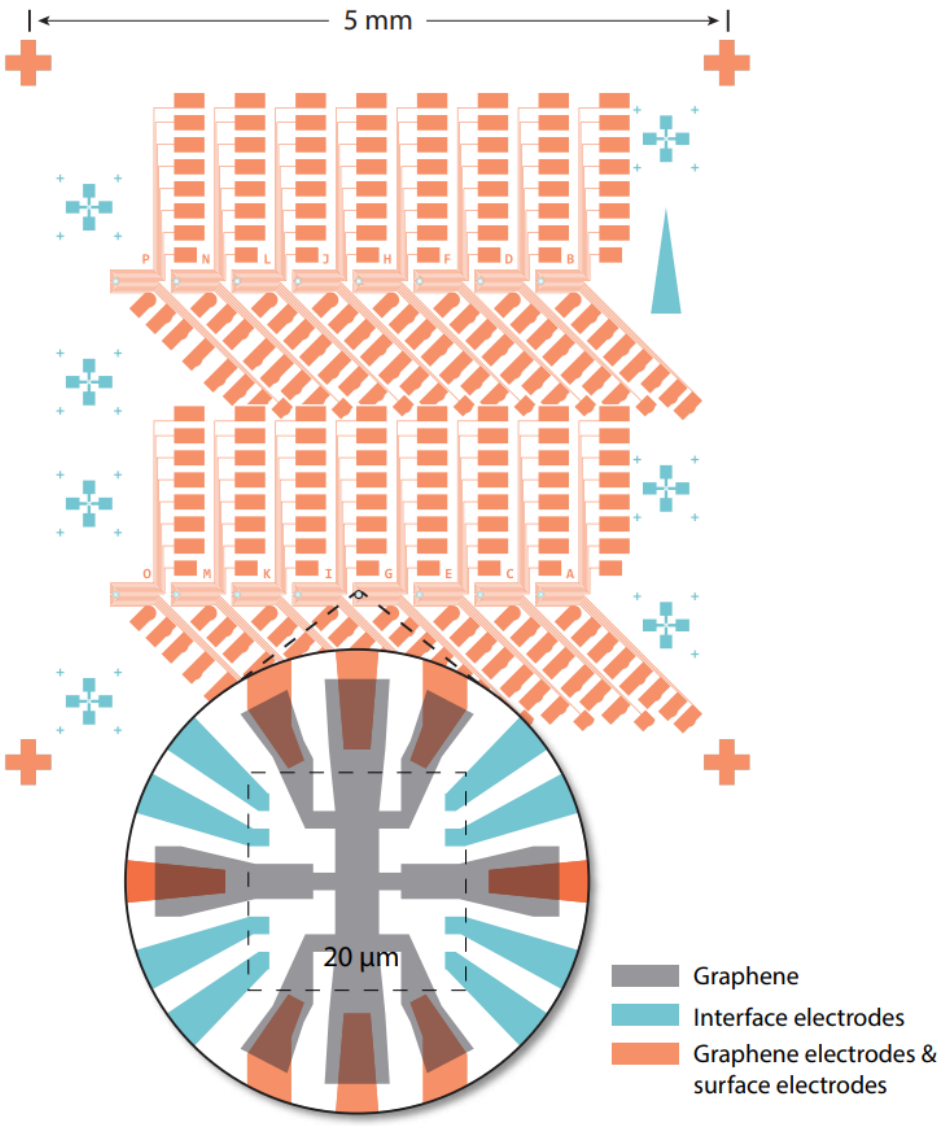

Figure 21: Patterns for graphene/LAO/STO. Two sets of electrodes are patterned separately, for interface and graphene contact. Adapted from [47].

acetone. This supporting AZ4210 layer is exposed to white light during the transferring process thus cannot be used for photolithography. Another 2.1 μm thick AZ4210 is spin-coated onto Hyflon/graphene/LAO/STO surface. The square-shape is patterned to protect the canvas. Then the sample is etched with RIE until all the contaminants and multi-layer graphene are cleaned. The etching time needs to exceed 300 s. After the first step, AZ4210

Table 3: One-step RIE etching recipe

Instrument	RIE
Gas	Oxygen
Flow rate	19 sccm
Power	50 W
Pressure	300 mTorr
Time	60 – 180 s

is washed off by acetone and IPA solvent. A 1.1 μm thick AZ4110 is spin-coated on the sample. The second step will etch the square graphene into a Hall bar shape. The recipe is listed in the following table 3.

After photolithography, AZ4210 is washed away by acetone. Only Hyflon is left on top of graphene. FC-40 a solvent for Hyflon with a boiling point at 170°C. To remove Hyflon, FC-40 is heated to 70°C and shook at 100 rpm for 12 hours.

2.2.3 STM on graphene/LAO/STO and AFM cleaning of graphene

Scanning Tunneling Microscopy(STM) is a technique for imaging surface at the atomic level. In STM experiments, one brings a sharp metallic tip very close to the surface of a sample, with a typical tip-sample distance of $\sim$ 1nm. For positive tip-sample bias voltages, electrons tunnel from the tip into empty states in the sample; for negative voltages, electrons tunnel out of the occupied states in the sample into the tip. The tunneling current is a function of tip position, applied voltage, and the local density of states(LDOS) of the sample.

First, a bias voltage is applied to either sample or tip. A tip is brought close to the sample by a coarse sample to tip control. When the tip is close enough, this control is turned off and replaced by a fine piezoelectric control. At this range, the typical distance between the sample and tip is 0.4 to 0.7 nm. The voltage bias will cause electrons to tunnel through,

creating a current that can be measured. Once tunneling is established, the distance and bias between tip and sample can be varied. There are two modes for STM, constant height mode and constant current mode. In constant current mode, height is adjusted during scanning to maintain a current. The variation in the image is due to the variation in charge density.

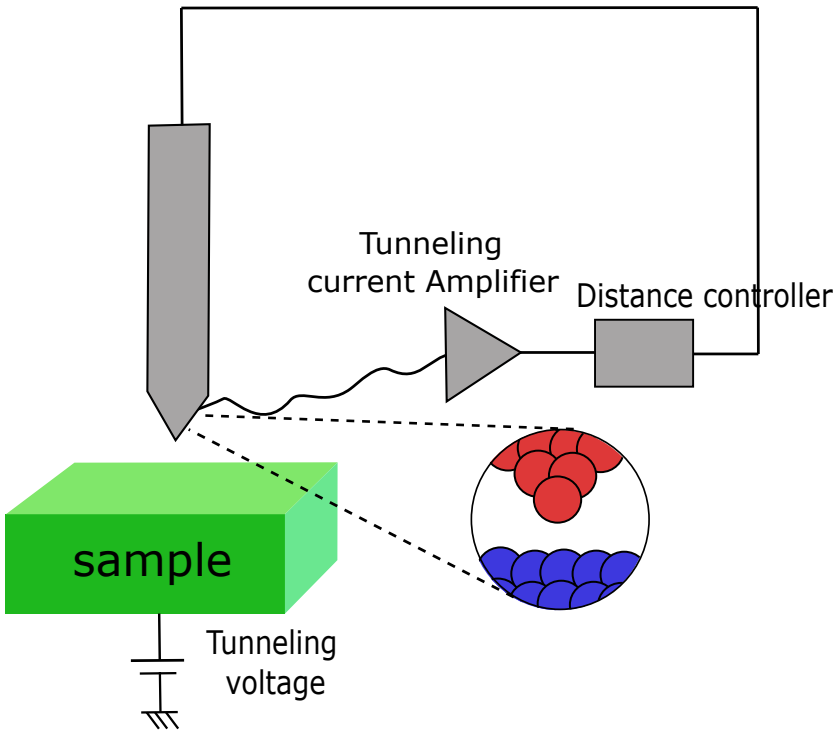

Figure 22: STM illustration. The voltage bias between the STM tip and the sample will cause electrons to tunnel through

We performed STM on graphite firstly. Highly Oriented Pyrolytic Graphite (HOPG) is stuck by silver paste on a steel AFM disc. This AFM disc has a bias wire which needs to be plugged into the sample socket on the scanner's terminal block. The sample is electrically connected to the attached bias wire. The STM tip is cut from a Pr-Ir STM wire by scissors. Before using, the wire needs to be cleaned with Isopropyl Alcohol(IPA). The desired sample bias voltage for HOPG is 50 mV. The setpoint for tunneling current is about 1 nA. Since STM uses log feedback, the integral gain is set to be 0.5 to 1, lower than the typical AFM. The parameters used for graphene/LAO/STO is the same as HOPG. The STM image of

graphene is shown in Figure 24.

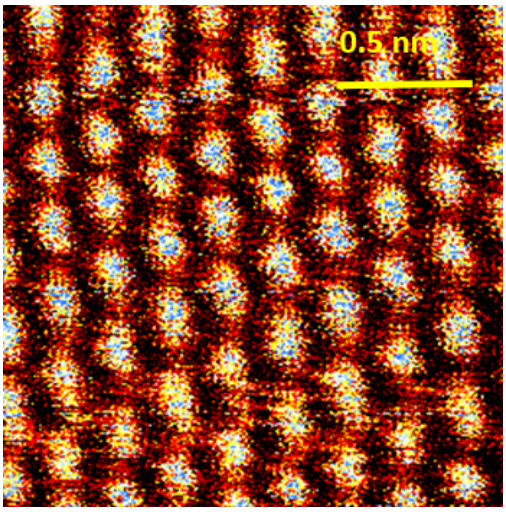

Figure 23: STM performed on graphite. Honeycomb lattice is observed on pure graphite. Scale bar is 0.5 nm.

The residual on graphene/LAO/STO can be further cleaned with AFM tip. Nanoparticles from DI-water, IPA, Acetone, Photoresist, developer and FC-40 leave on the sample surface may suppress the mobility of graphene. Therefore, a contact mode AFM scanning is the extra step of sample cleaning.

The comparison between before and after AFM cleaning is shown in Figure 25. An AFM phase image of the graphene Hall bar is shown in 25. Particles are visible on both graphene and LAO/STO. Figure 15(b) is the zoom in of the graphene Hall bar, as shown by a dash line square in (a). In this small region, graphene is first scanned with contact mode. The contact force is typically ranged from 20-200 nN, varied from sample to sample. Small particles are pushed to the edge of the contact scan region. This region is then imaged by AC mode scanning with a slightly larger range. From figure 15(b), we can clearly see the graphene winkle and LAO/STO terraces. The height of terraces is 4 Å. Wrinkles on graphene are formed during growth due to interaction between graphene and the substrate. Graphene has the opposite polarity of the thermal expansion coefficient compared with the metal. As graphene is cooled (the last step of CVD growth), the number of flexural modes is reduced, which leads to the expansions of graphene in the horizontal direction. Wrinkle can also form

during transferring. In Figure 30, we can clearly see more wrinkles on gold electrodes.

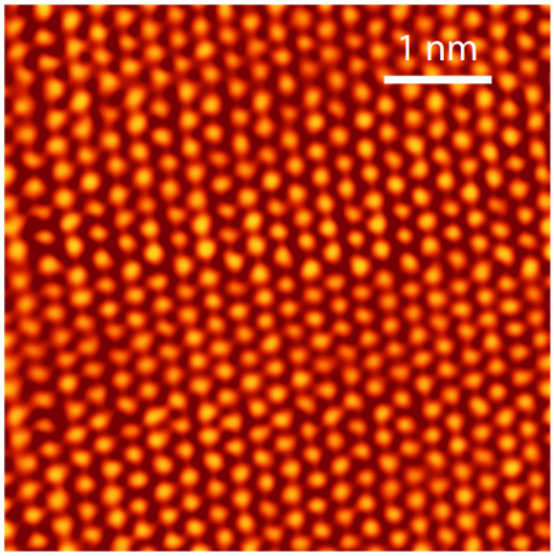

Figure 24: STM image of graphene on LAO/STO after AFM cleaning. Honeycomb lattice is observed clearly.

2.3 Atomic force microscope

The atomic force microscope (AFM) was developed to overcome an essential drawback with STM, which can only image conducting or semiconducting surfaces. Atomic force microscopy (AFM) is a very high resolution type of scanning probe microscopy, with the resolution in the order of fractions of nanometer.

Two fundamental parts of AFM are the probe and the scanner. The tip is the point contact of the AFM and the sample. The scanner is used for controlling the movement of the sample, both vertically and horizontally. When two materials are brought very close together, interactions are present at the atomic level. An AFM tip is particularly sensitive to such interactions. The sensed interaction can be correlated to the distance between the probe and the sample. Since the probe sample distance is a function of interactions, the AFM can map the topography by scanning the probe over the sample surface. Piezoelectric ceramic

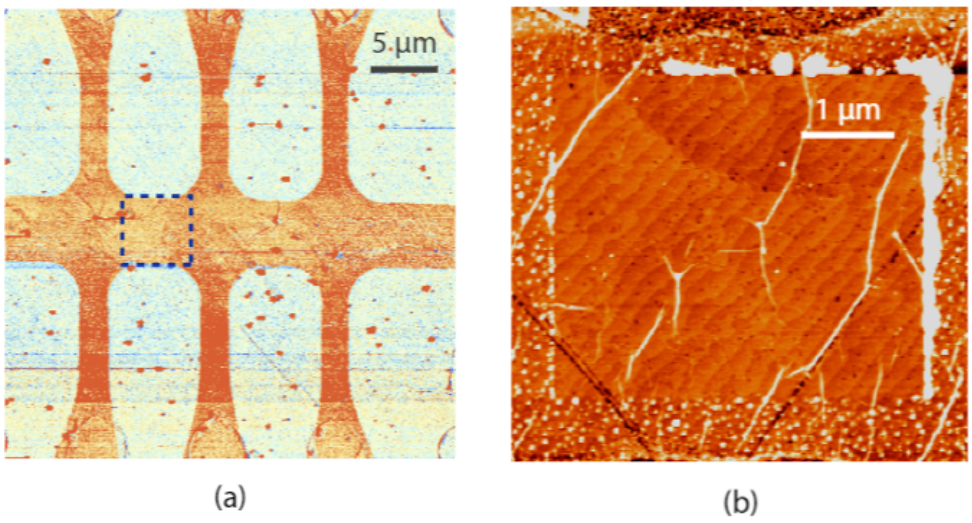

Figure 25: AFM cleaning of graphene. (a) The organ Hall bar region is the graphene, after Hyflon removal in FC-40. Particles on graphene can be observed. (b) Zoomed-in image of the square region in (a). The center has been scanned in AFM contact mode. Particles are pushed to the top and right edges. Terraces of LAO/STO and wrinkles can be observed.

is required for precise positioning control. The voltage applied to piezoelectric ceramic is proportional to the mechanical deformation. Thus, it provides a way of controlling the sample probe distance and the moving of the scanner in a horizontal direction.

The signal can be collected as the probe moves from left to right (called "trace") and from right to left ("retrace"). The ability to collect trace and retrace can be very useful in factoring out specific effects that do not accurately represent the sample surface. This left to right or right to left is referred to as the "fast scan direction". The direction perpendicular to fast scan is "slow scan direction". During scanning, the probe produces a signal representing the magnitude of interaction. AFM probes are usually 5 μm tall and less than 10 nm in diameter at the apex. The tip is located at the free end of a cantilever, typically 100 to 500 um long. Most AFMs use optical techniques to detect the position of the cantilever. The light beam from a laser diode reflects off the back of the cantilever and detected by a position-sensitive photodetector. As the cantilever bends, the position of the reflected laser

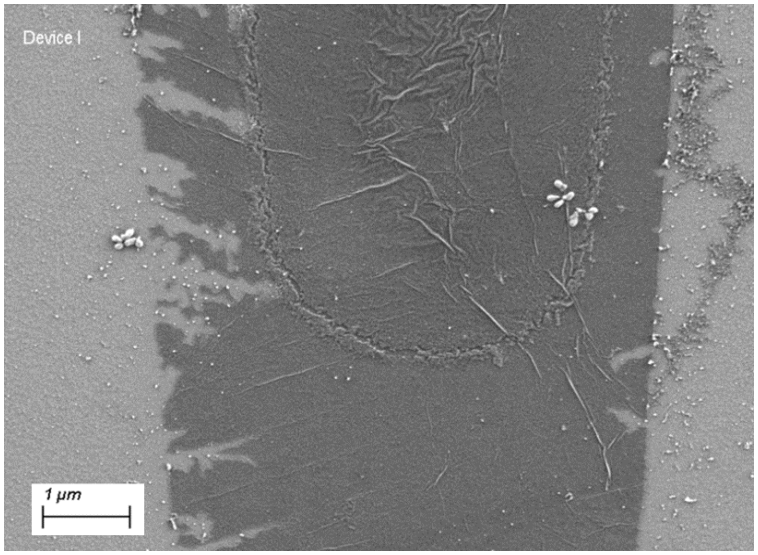

Figure 26: SEM image of graphene on LAO/STO. Gold electrode with "U" shape is visible under graphene. The thickness of gold electrode is 5 nm.

beam on the photodetector changes. Here the position signal is referred to as the detector signal.

A reference value known as the setpoint is established to make the detected signal to be meaningful. The detector signal is compared to the setpoint when the scanner moves the probe into the imaging regime. Scanning will begin only when the detector signal is equal to the setpoint.

The probe moves over the sample surface in a raster pattern. As the probe encounters changes in the topography, the probe-sample distance changes, triggering a variance in the detector signal. The difference between the detector signal and the setpoint is referred to as an error signal, which is the raw data used to generate an image of the surface topography.

AFM employs a method called Z feedback to ensure the probe tracks the sample surface accurately. The method involves continually comparing the detector signal to the setpoint. If they are not equal, a voltage is applied to change the Z position of the probe. This z feedback can be turned on and off. The advantage of feedback is that it can provide high precision measurements on an irregular surface. With z feedback, the scanning can be faster.

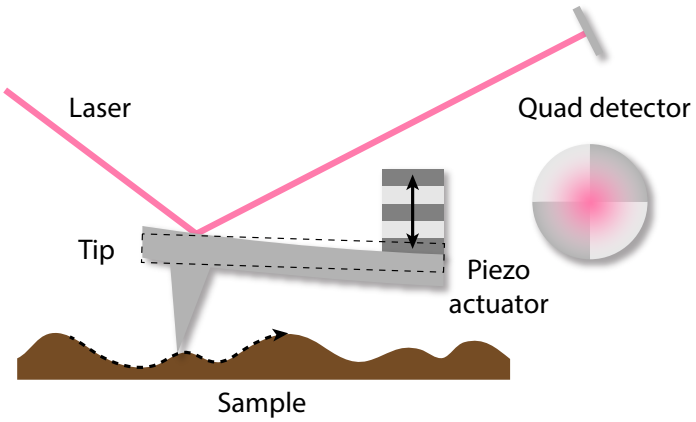

Figure 27: Typical optical detection scheme in AFM. Reflected light is detected by quad detector. Adapted from [47].

2.3.1 Contact mode and non contact mode

As shown in Figure 28, at the right side of the curve, the tip and sample are separated. As the tip approaching the sample surface, their atoms begin to attract each other weakly. This attraction increases until the atoms are too close that the electron clouds start to repel each other. In the contact mode region, the slope of the curve is very steep. In AFM, this means the cantilever bends rather than forcing the tip moving closer. The cantilever is chosen to have a low spring constant. As the tip gently traces across the sample surface, the cantilever bends to accommodate the topography changes.

In non-contact mode, the spacing between the tip and sample is tens to hundreds of Angstroms. The interaction between tip and sample is attractive. Under this mode, the cantilever vibrates near its resonant frequency(typically $100 \sim 400$ kHz) with an amplitude of a few tens to hundreds of Angstroms. The system detects changes in the cantilever's resonance frequency and vibration amplitude. The interaction in non-contact mode is smaller than the contact mode. Thus cantilevers used for non-contact mode must be stiffer those used for contact AFM.

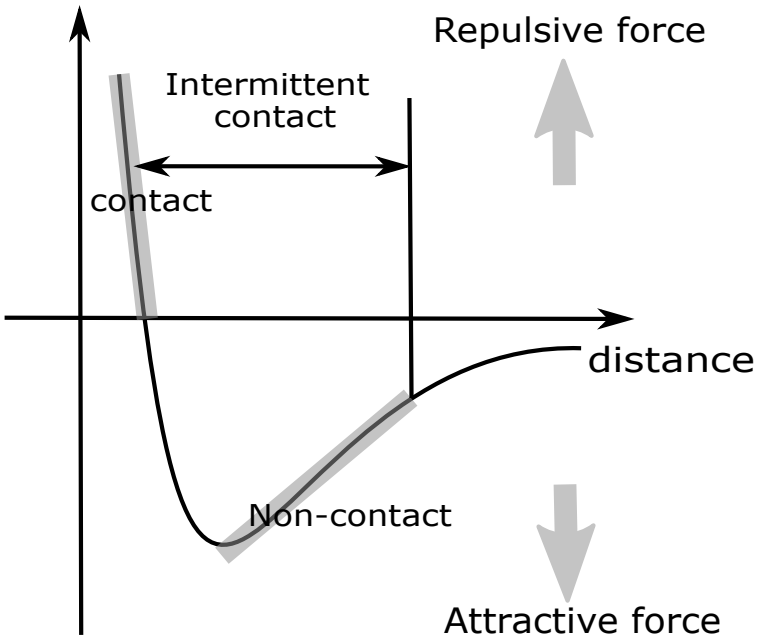

Figure 28: Attractive and repulsive forces. As the distance between the tip and the sample increases, the force is changed from repulsive force to attractive force.

2.3.2 Magnetic force microscopy

Magnetic force microscopy(MFM) is an AFM imaging mode derived from Tapping Mode that maps the magnetic force gradient above the sample surface. This mapping is performed via a two-pass technique, nap mode, which separately measures topography and another property(magnetic property, electric property, etc.). The topographical information is used to track the tip at a constant height above the sample surface during the second pass.

The MFM tip is usually standard Si tip coated with a few nanometers thick ferromagnetic thin layer. After the profile of morphology is constructed, the tip scans the surface at fixed-sample distance Δz, usually tens of nanometers. At such values of Δz, only the long-range tip-sample interaction affects the cantilever motion. The cantilever is set into oscillation at a higher distance at its first free resonance frequency f_0. Due to the magnetic coating, the tip experience a magnetic force. Such a force produces a variation with an amplitude A and

shifts in the phase φ

$$\Delta A = \frac{A_0 Q_c}{2k_c^2}(\frac{\partial F_z}{\partial z})^2 \tag{2.1}$$

$$\Delta\varphi = \frac{Q_c}{k_c}\frac{\partial F_z}{\partial z} \tag{2.2}$$

$$\Delta f_0 = -\frac{f_0}{2k_c}\frac{\partial F_z}{\partial z} \tag{2.3}$$

Where k_c and Q_c are the cantilever spring constant, and the quality factor of the cantilever first resonance in the air. A_0 and f_0 are the free amplitude and resonance. In MFM, the signal is obtained by recording the valves of $\Delta\varphi$ and Δf_0.

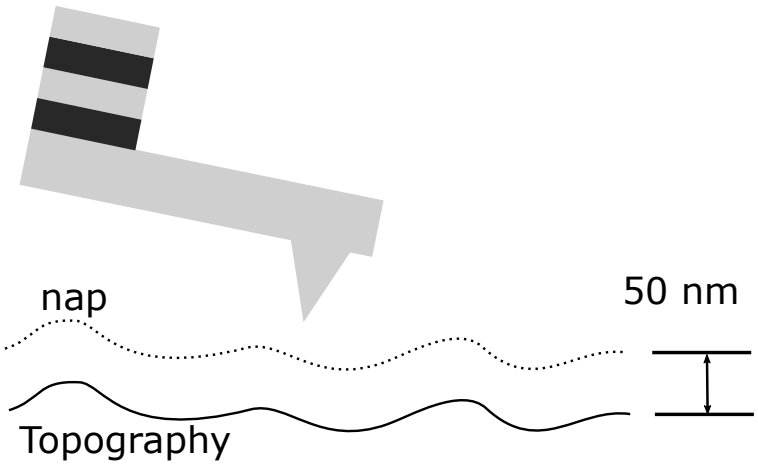

Figure 29: During nap mode, the probe first scan across the sample surface then raised to a delta height defined by the user. This allows for the detection of long-range forces between the tip and sample.

2.3.3 Piezo force microscopy

Piezo force microscopy measures the mechanical response when an electrical voltage is applied to the sample with a conductive AFM tip. The sample may expand or contract

locally in response to the electrical stimulus.

$$\varepsilon_k = \sum_{i=1}^{3} d_{ik} E_i,$$

Where ε_k is the strain tensor, d_{ik} is the piezoelectric tensor and E_i is the electric field. For a tetragonal system,

$$\begin{bmatrix} \varepsilon_1 \\ \varepsilon_2 \\ \varepsilon_3 \\ \varepsilon_4 \\ \varepsilon_5 \\ \varepsilon_6 \end{bmatrix} = \begin{bmatrix} 0 & 0 & d_{31} \\ 0 & 0 & d_{32} \\ 0 & 0 & d_{33} \\ 0 & d_{15} & 0 \\ d_{15} & 0 & 0 \\ 0 & 0 & 0 \end{bmatrix} \begin{bmatrix} E_1 \\ E_2 \\ E_3 \end{bmatrix}$$

The relationship between the strain and the applied electric field is described by a rank-3 tensor. The most essential component of this tensor for vertical PFM is the d_{33} component.d_{33} directly describe the vertical motion of the cantilever. The voltage applied to the tip is

$$V_{tip} = V_{dc} + V_{ac} \cos \omega t \tag{2.4}$$

The applied voltage results in a piezoelectric strain in the material and causes the movement of the cantilever due to the piezoelectric effect.

$$z = z_{dc} + A(\omega, V_{ac}, V_{dc}) \cos \omega t + \varphi \tag{2.5}$$

When the drive voltage is well below the contact resonance of the cantilever, the expression becomes

$$z = d_{33} V_{dc} + d_{33} V_{dc} \cos \omega t + \varphi \tag{2.6}$$

When a voltage is applied across the thickness of the piezoelectric materials

$$\Delta L = d_{31} \cdot V_3 L/t,\ \Delta w = d_{31} \cdot V_3 w/t,\ \Delta t = d_{33} \cdot V_3 \tag{2.7}$$

The magnitude of the oscillating of the tip is a measure of the magnitude of d_{33}. The phase is indicator of the polarization direction of the sample.

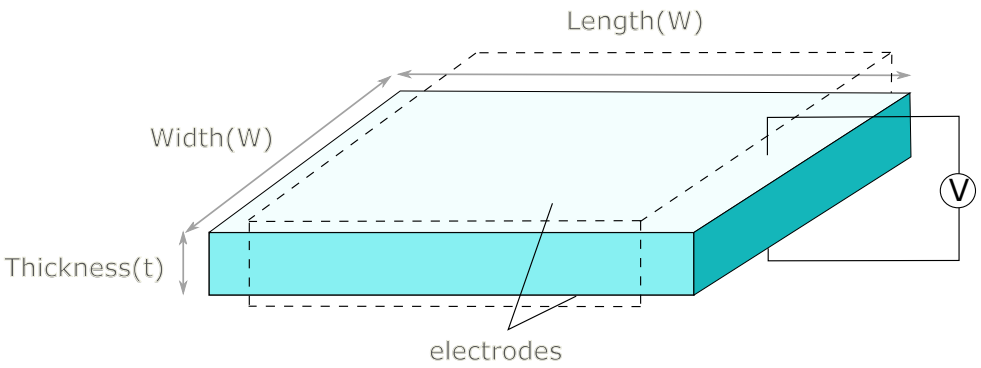

Figure 30: Piezoelectric effect. The sample may expand or contract locally in response to the electrical stimulus.

2.3.4 LAO/STO nano-device c-AFM lithography

Figure 31 demonstrates a c-AFM lithography process. The conductance is monitored during writing process. When a positive voltage larger than 6V is applied to a conductive AFM tip, the sketched region becomes conductive. During writing, a protective resistor of 1 GΩ is added between tip and voltage source. The voltage source is connected to one of the LAO/STO interface electrodes. The other LAO/STO electrode is ground. Meanwhile, graphene is floating. The typical voltage for writing is +15 V. The tip sketching speed is 0.5 μm to 1 μm. The force is ranged from 20 $\sim$ 80 nN. The typical erasing voltage is - 8 V.

The nanostructure on the LAO/STO interface can be imaged by PFM. During PFM imaging, a sinusoidal voltage is applied to a conducting AFM tip while the tip is in contact with the sample surface. The frequency of the sinusoidal voltage is usually three to four times of tip resonance frequency, ranged from 300 kHz to 500 kHz. The sinusoidal voltage alters the carrier density and causes the LAO/STO deformation due to the Jahn-Teller effect. The carrier density in sketched nanowire is different from the rest of the sample. Thus the deformation is visible under PFM mode.

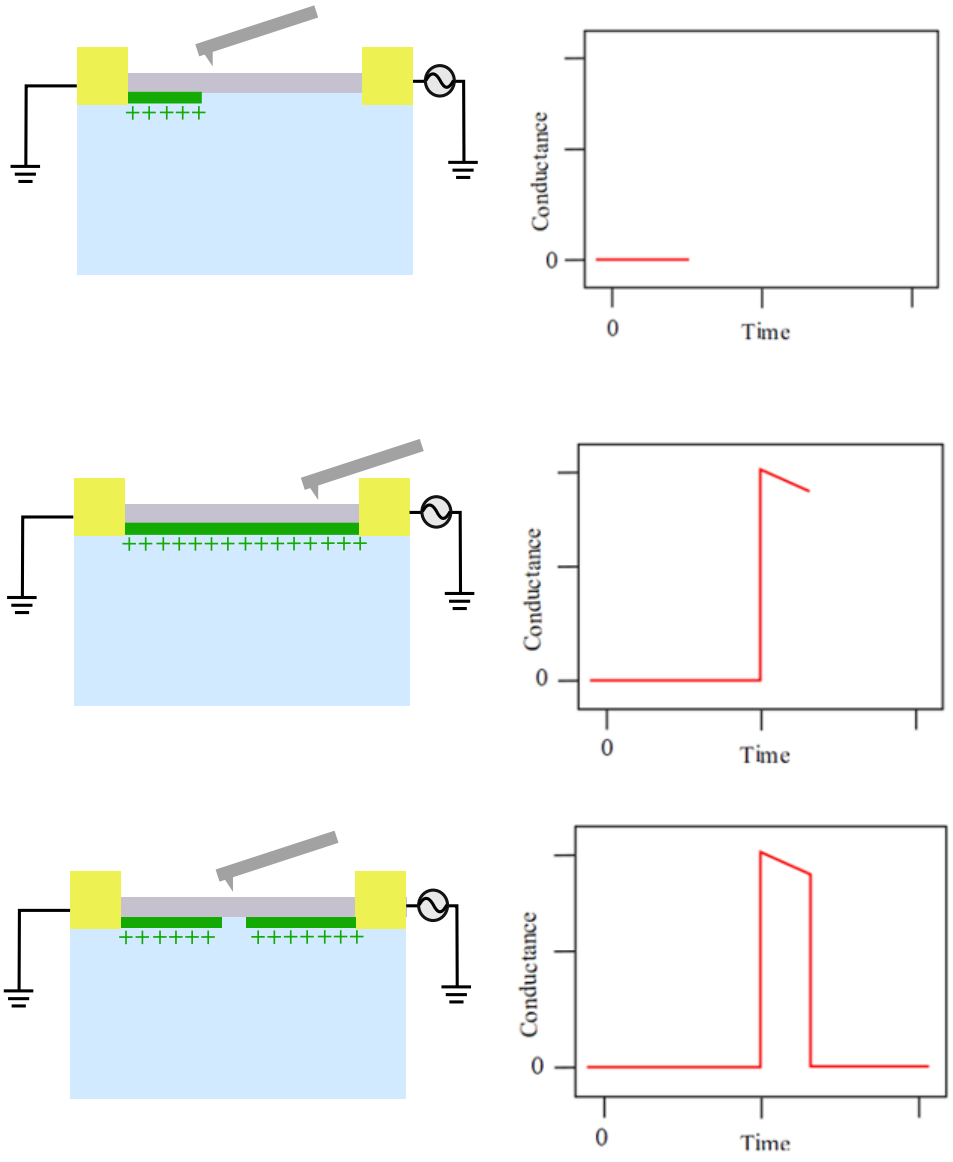

Figure 31: c-AFM lithography at the LAO/STO interface. Top: under contact mode, a positive voltage is applied to a conductive AFM tip. The monitored conductance is zero. Mid: a conductive path is created between two gold electrodes. A typical conductance jump is sketched in the conductance monitor panel. Bot: negative voltage is applied to the tip. An insulating gap is created in the mid of the conducting wire. The sketched conductance drops to zero after the cutting.

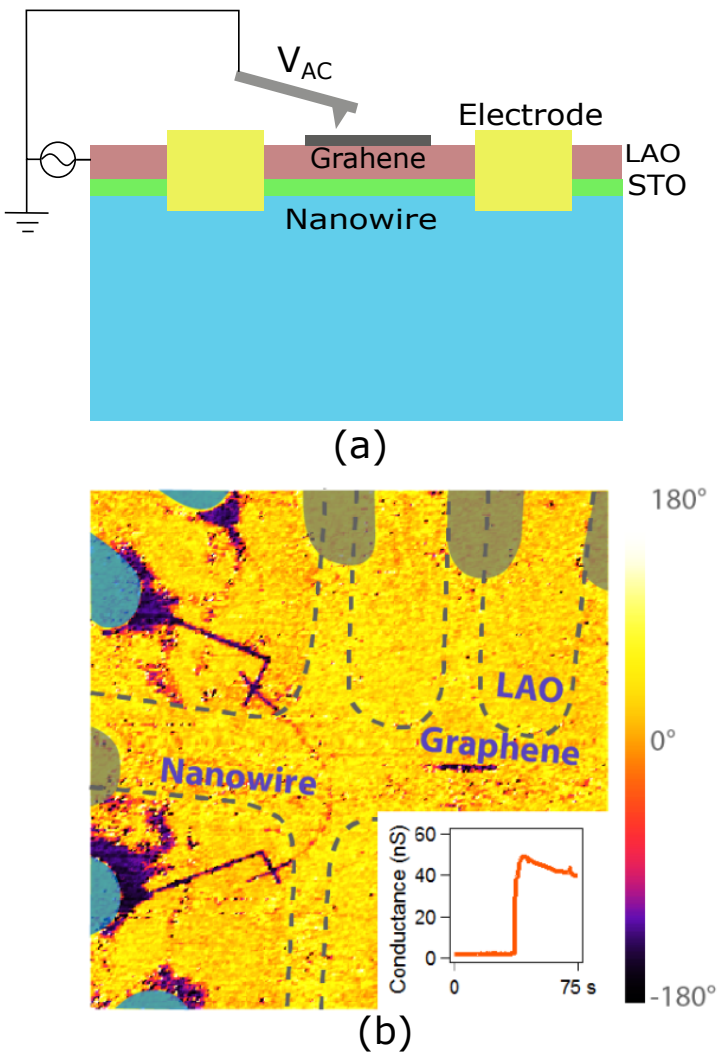

Figure 32: (a) PFM setup for imaging a nanowire on the graphene/LAO/STO device. (b) PFM image of the nanowire underneath the graphene. The inset shows the conductance jump after a conducting nanowire connects the two interface electrodes.

2.3.5 Graphene quantum dot

Quantum dots are of interest because they can bridge the gap between the bulk and molecular levels and leads to new applications, such as electronics, optoelectronics, and biology [4]. During the last two decades, a great deal of attention has been focused on the

electronic properties of quantum dots as many fundamental properties are size-dependent in the nanometer range.

Here we created graphene quantum dot on LAO/STO that can be created by c-AFM lithography. Graphene can be cut through when the tip is applied with negative voltage smaller than -8 V. As shown in Figure 33(a), the whole device is covered with graphene. After the tip scratching on the sample surface with -10 V, graphene is completely removed along the path. The entire graphene is divided into five parts. "S" and "D" denote for graphene source and drain electrodes where current can pass through. "SG1" and "SG2" work as two side gates that can independently tune the chemical level locally.

Transport through a quantum dot system can now be viewed in terms of the energy diagram of a double tunnel barrier. With a small bias and low temperatures, transport through the dot is blocked due to the Coulomb blockade effect, with N electrons on the dot. By decreasing the gate voltage, the chemical potential inside the dot is raised. Until the potential aligns with the drain contact, and an electron can leave the dot. If chemical potential in the source is higher than drain, a current can flow, and the number of electrons on the dot will fluctuate between N and N-1. When the gate voltage further decreases and the source's chemical potential is smaller than the drain, the dot is left with one electron less than N-1, and the current is again blocked.

In Figure 33(b), coulomb blockade is observed. the current is blocked inside the titled diamond-shaped areas. In these areas, the number of electrons in the dot, N, is constant. Conductance peaks occur on the V_{bg} axis at points where neighboring diamonds touch. Excited states move as lines parallel to the diamonds' borderlines in the regions where the current is not blocked.

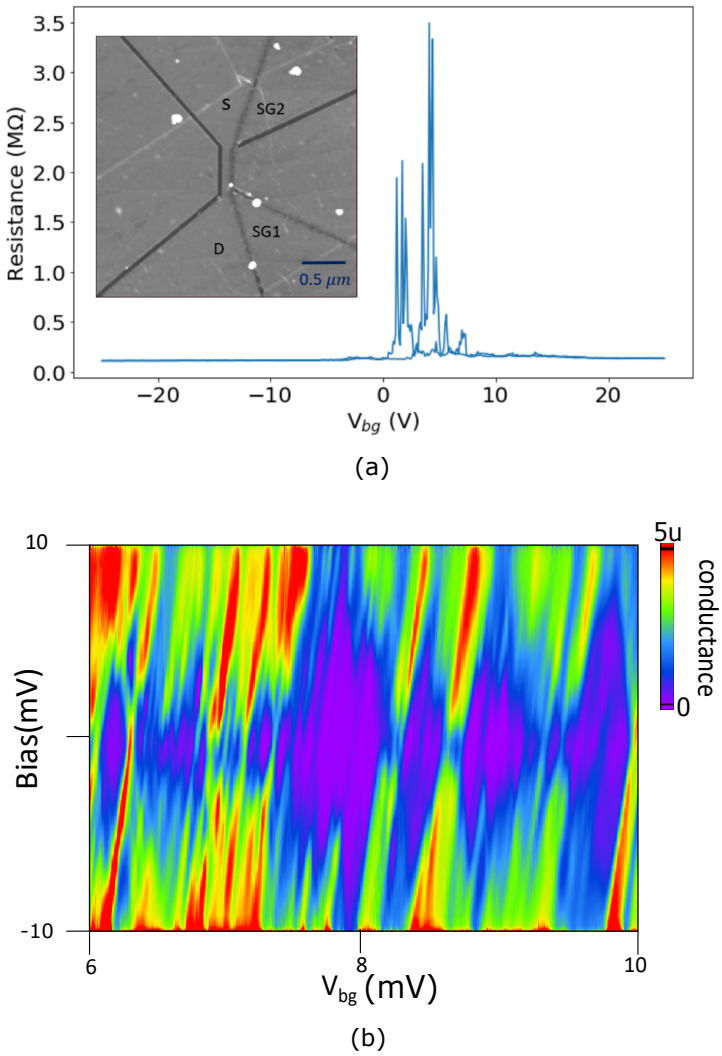

Figure 33: Graphene quantum dot cut by AFM tip. (a) Two terminal resistance of the quantum dot as a function of backgate. Inserted is the AFM image of the device. "S" denotes for "source". "D" denotes for "drain". SG1 and SG2 are two sidegates of the quantum dot. (b) Measurement of Coulomb blockade diamonds in the differential conductance

3.0 Graphene/LAO/STO heterostructure device

Similar to the nanostructure lithography on bare LAO/STO, conducting regions can also be created underneath graphene. Four experiments are discussed here: edge-state mixing on graphene $p-n$ junctions, graphene superlattice patterning, coulomb drag between graphene, and LAO/STO.

3.1 Graphene chemical potential tuning

The schematic of graphene/LAO/STO device is shown in Figure 34. Graphene is patterned into a Hall bar structure. Six gold electrodes are connected to graphene to perform Hall measurements. The global chemical potential can be tuned by applying a backgate voltage to the backside of STO. Local chemical potential can be altered by sidegate sketched by c-AFM lithography on both graphene and LAO/STO.

Compare to Si substrate, the dielectric constant of STO is relatively large. As the temperature goes down, the dielectric constant keeps increase. At 2 k, the dielectric constant of STO is around 20,000. The carrier density of graphene can be efficiently tuned by backgate. Due to the electron-hole symmetry, the density of states of graphene at Dirac point is zero. The resistance of graphene reaches a maximum at Dirac point, namely $\frac{2e^2}{h}$.

Another effect of the LAO/STO substrate is the hysteresis behavior during backgate sweeping. The Dirac point shifts after each backgate voltage V_{bg} cycle. The dipole moment induced by displacement of oxygen atoms would result in ferroelectric-like hysteresis behavior [71]. Similar hysteretical behavior of graphene on LAO/STO has been reported elsewhere [42]. The hysteresis behavior can be reduced by optimizing the backgate sweep rate or replacing the backgate with a sidegate.

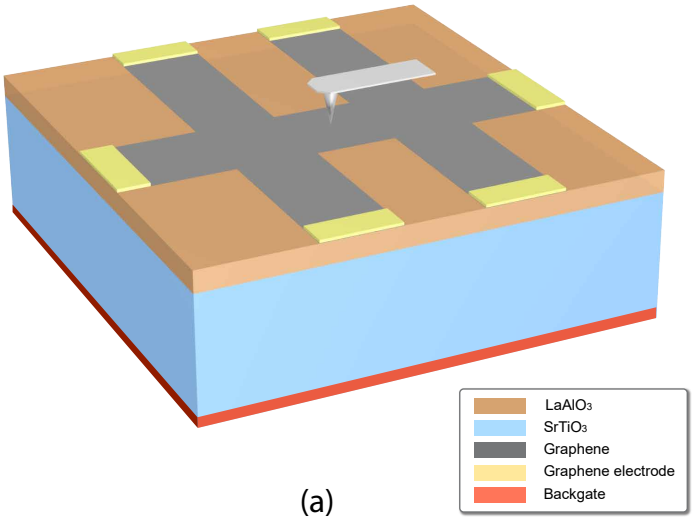

(a)

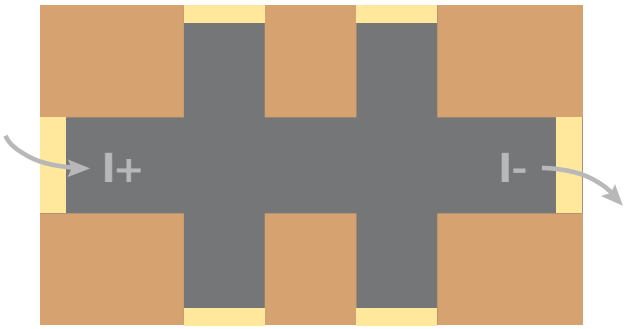

(b)

Figure 34: (a) Graphene/LAO/STO Hall bar device. (b) Current flows through graphene source drain leads. Longitudinal and transverse voltage can be measured by this configuration. Adapted from [47].

3.1.1 Graphene/LAO/STO local doping

At room temperature, one method of monitoring the doping level of graphene is to sweep the back-gate voltage and compare CNP position before and after the doping. However, this method cannot be utilized here. The V_{bg} is subject to significant hysteresis [19, 42] (also

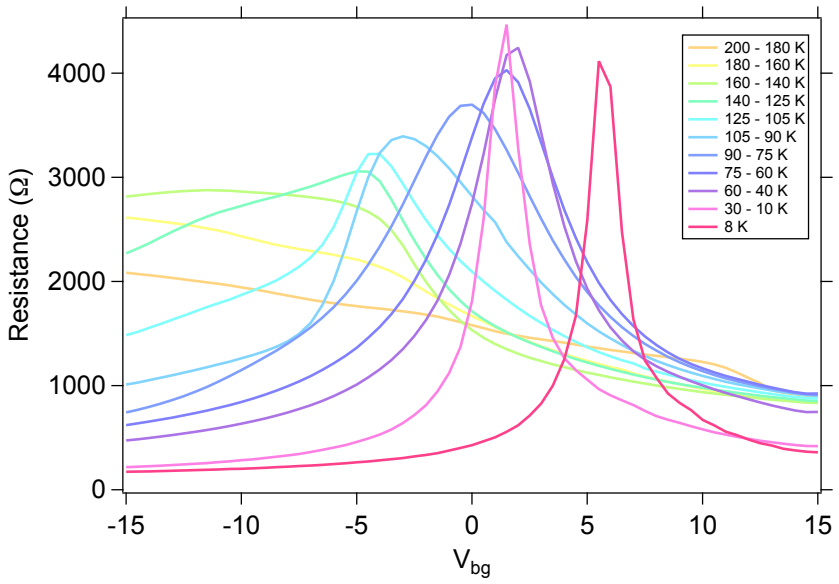

Figure 35: Resistance as a function of V_{bg} sweep at different temperatures. The CNP width clearly shows the change of dielectric constant of STO as a function of temperature. Adapted from [47].

shown in Figure 36) and thus is not a reliable indicator of doping level for CNP. Instead, in Figure 37, the four-terminal resistance of graphene is measured *in situ* to monitor the doping level change during the c-AFM writing process.

A conducting region can be created at the LAO/STO interface underneath the graphene and can be further tuned by a sketched gate locally(Figure 38). A single CNP is observed in the two terminal resistance of graphene as a function of backgate. The green rectangle in 38(c) denotes a conducting region sketched by c-AFM under the graphene. A side peak emerges near the main Dirac point in (d), representing the shift of the chemical potential of the conducting region. The side peak can be further tuned by applying a voltage to the written region. In (e), a conducting wire is sketched to connect the gold electrode and the conducting square. As the voltage V_{sg} applied to the gold electrode varies, the separation of the main peak and the side peak increases.

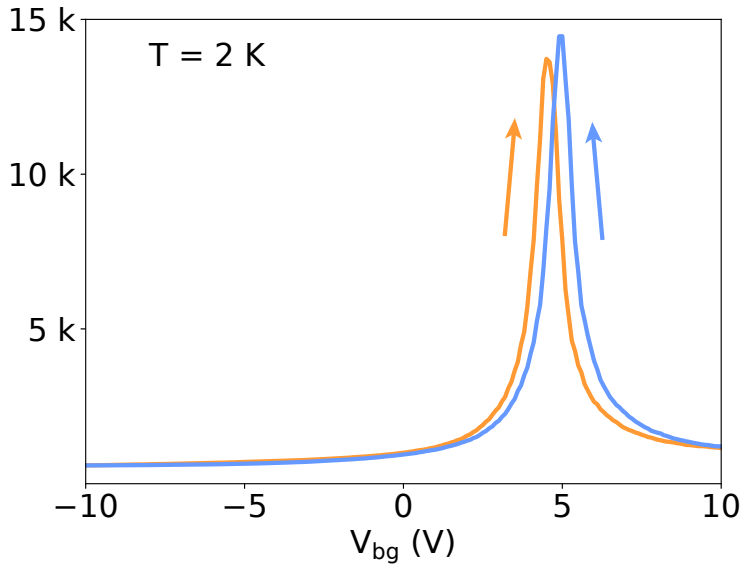

Figure 36: Graphene resistance as a function of backgate voltage. The resistance shows a maximum when the chemical potential reaches the CNP. The positions of the CNP are different for the forward and backward sweeps. The arrows indicate the directions of sweeping. Measured at $T = 2$ K. Adapted from [47].

3.1.2 Graphene/LAO/STO quantum Hall

As we discussed in the previous chapter, electrons under the magnetic field will perform cyclotron motion. If electrons bounce back from the edge, they will collide with the edge and keep moving in the same direction. In this way, chiral edge channels are formed with backscattering being suppressed. The transport along edge states can be quantified by Landauer-Buttiker formalism for 1D waveguides. The resistance of the system with N conducting channels is

$$R = \frac{h}{e^2}\frac{1}{T} \tag{3.1}$$

$T = \sum_{i,j=1...N} T_{ij}$, and T_{ij} is the transmission probability from channel j into channel i.

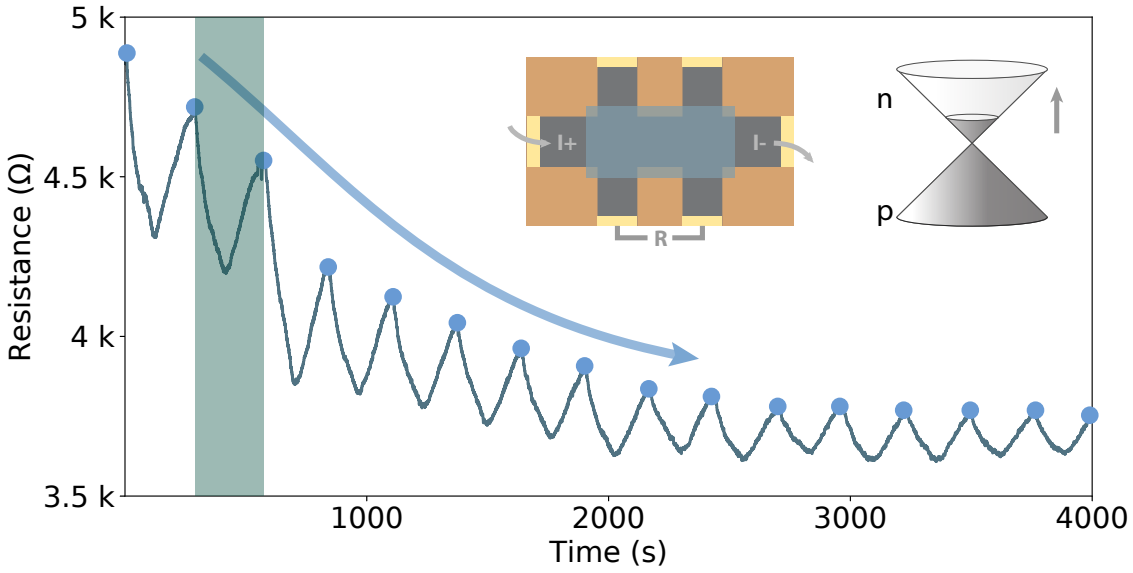

Figure 37: Monitoring the doping level change during the c-AFM writing process. The rectangle in the inset is scanned with a c-AFM tip continuously, while the four-terminal resistance is measured *in situ*. The blue dots mark the beginning/ending of the consecutive scans. The green region marks one complete scan. The resistance drops in the first half of each scan, and then recovers as the scan proceeds. The terminal resistance of each scan decreases as the scan proceeds, indicating increasing n-type doping level of graphene. Adapted from [47].

3.1.3 Edge channel mixing of graphene unipolar/bipolar junction in quantum Hall regime

In the quantum Hall region, when two adjacent graphene regions have different carrier densities, Landau filling factors are different. Thus the different direction or number of edge channels would cause edge mixing. When the carrier type in these two regions are the same, the edge currents flow in the same direction(unipolar), part of the current will be reflected into the interface of the two regions. When the two regions have different carrier types, the edge current flows in different directions(bipolar). The edge channels will mix

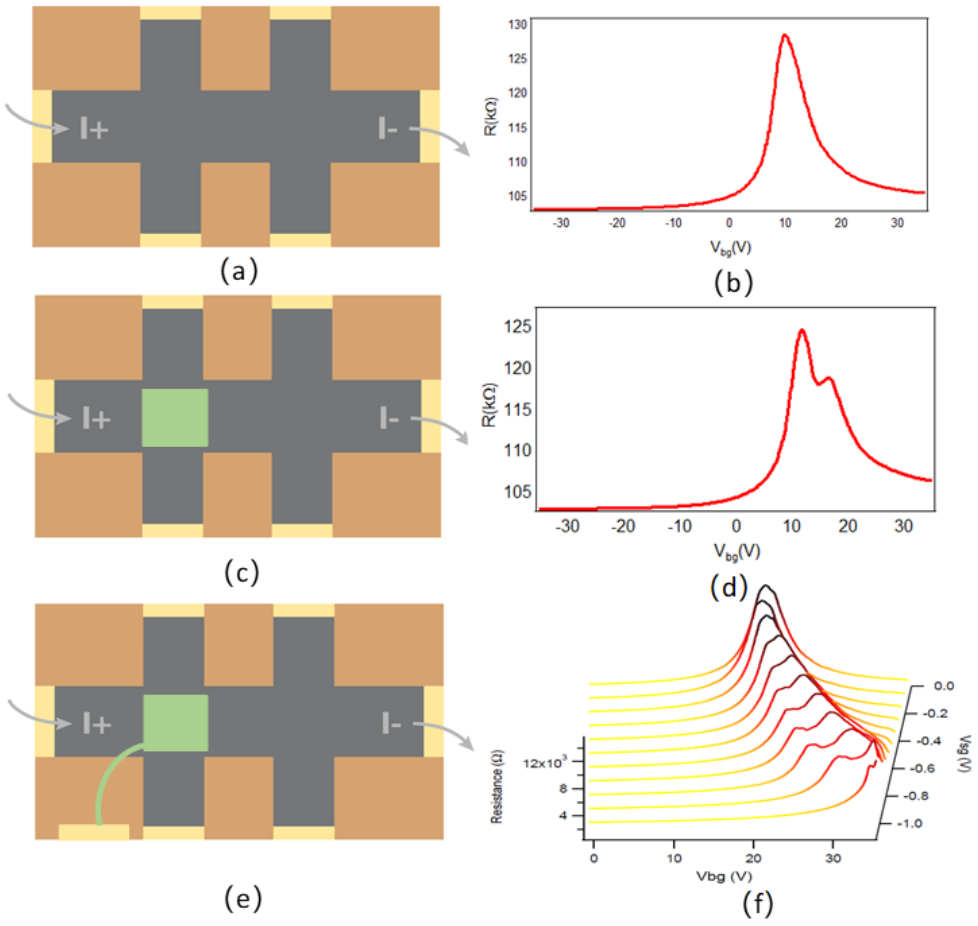

Figure 38: Graphene resistance as a function of a interface gate (Device 2). The resistance shows a maximum when the chemical potential reaches the CNP. The positions of the CNP are different for the forward and backward sweeps. The arrows indicate the directions of sweeping. Measured at $T = 2$ K.

on the interface. These mixes are represented by the non-trivial longitudinal resistance. For unipolar case, the longitudinal resistances are

$$\begin{aligned} R_{AB} &= \frac{\mu_A - \mu_B}{eI} = 0, \\ R_{CD} &= \frac{\mu_C - \mu_D}{eI} = \frac{h}{e^2}\left(\frac{1}{|\nu_2|} - \frac{1}{|\nu_1|}\right). \end{aligned} \tag{3.2}$$

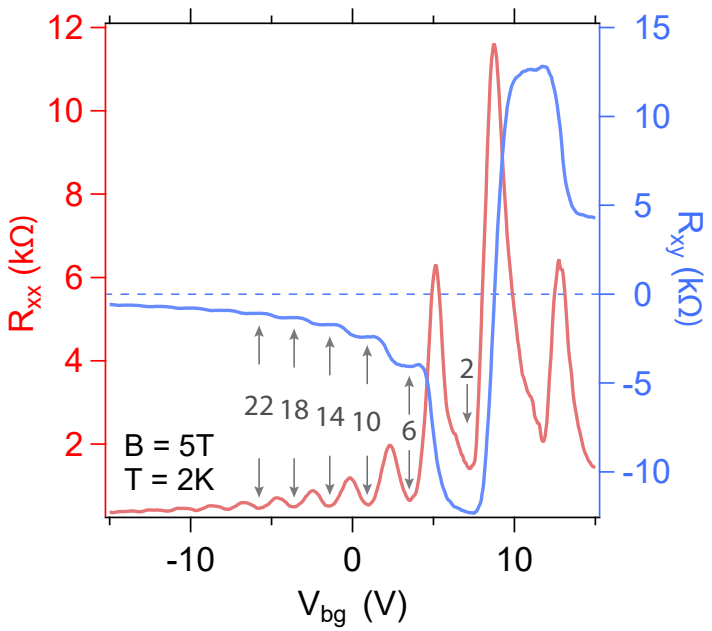

Figure 39: Integer quantum Hall effect of single layer graphene (Device 3). The plateaus in the transverse resistance (blue line) are clearly visible.

For bipolar case, the longitudinal resistances are

$$\begin{aligned} R_{AB} &= \frac{\mu_A - \mu_B}{eI} = \frac{h}{e^2}\left(\frac{1}{|\nu_1|} + \frac{1}{|\nu_2|}\right), \\ R_{CD} &= \frac{\mu_C - \mu_D}{eI} = 0 \end{aligned} \tag{3.3}$$

The local doping of graphene can be achieved by c-AFM technique. The whole device is half written by $V_{\text{tip}} = +17$ V. In Figure 42(b), carrier density of two regions are shown as a function of backgate. After writing, the carrier density of two regions are diffrent. As the backgate is changed from 0 V to 4 V, Device R_{xx1} and Device R_{xx2} are tuned from $p-$type unipolar, p-n bipolar and n-type bipolar. At $B = 7$ T, the longitudinal resistances are measured from the bottom (R_{xx1}) and top (R_{xx2}) pairs of electrodes as functions of V_{bg}. The result is shown in Figure 42(a). R_{xx1} is equal to $h/3e^2$ at around $V_{\text{bg}} = 0$ V, then is suppressed between 1 V and 3 V, and equals to $h/3e^2$ again around $V_{\text{bg}} = 5$ V. R_{xx2} is suppressed around $V_{\text{bg}} = 0$ V and 5 V, and is equal to h/e^2 at 2 V.

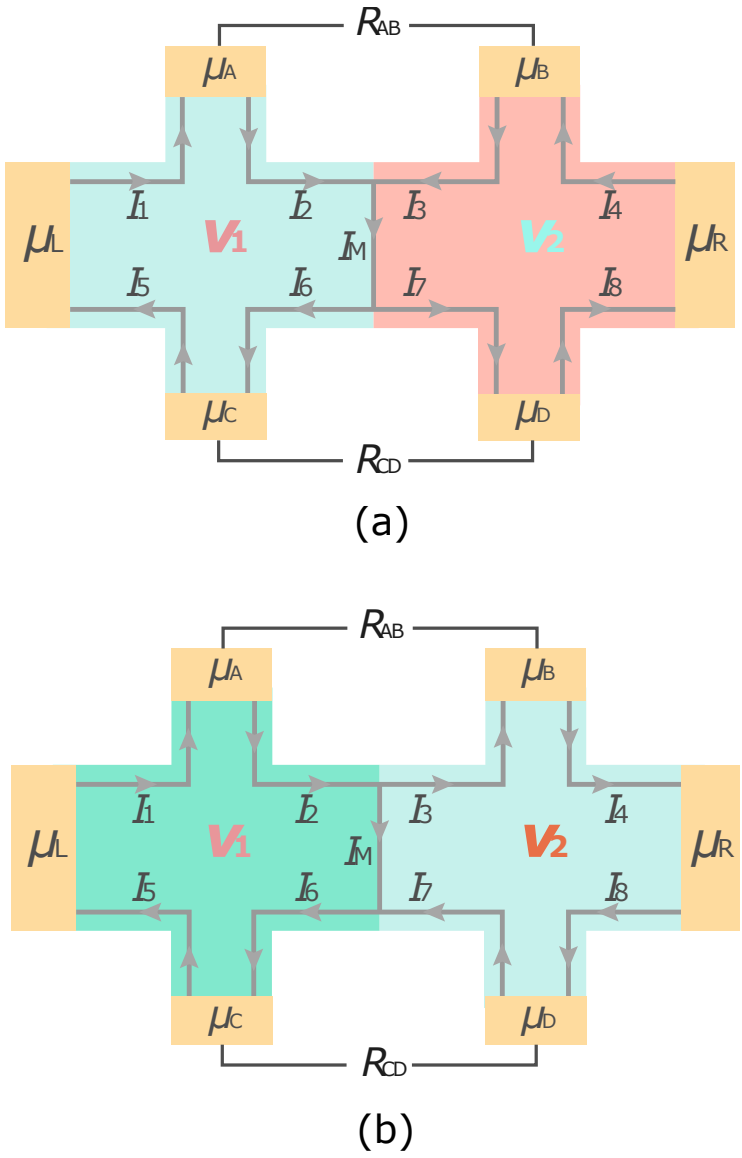

Figure 40: Edge currents of the unipolar junction. Assume $\mu_L > \mu_R$ and the current is flowing towards right. All the voltage leads have zero net currents.

When the magnetic field is reversed, the direction of the current is also reversed. Thus the values of R_{xx1} and R_{xx2} are swapped. Compare Figure 43(a) and (b), we can clearly see the swap of R_{xx1} and R_{xx2} under positive and negative magnetic field.

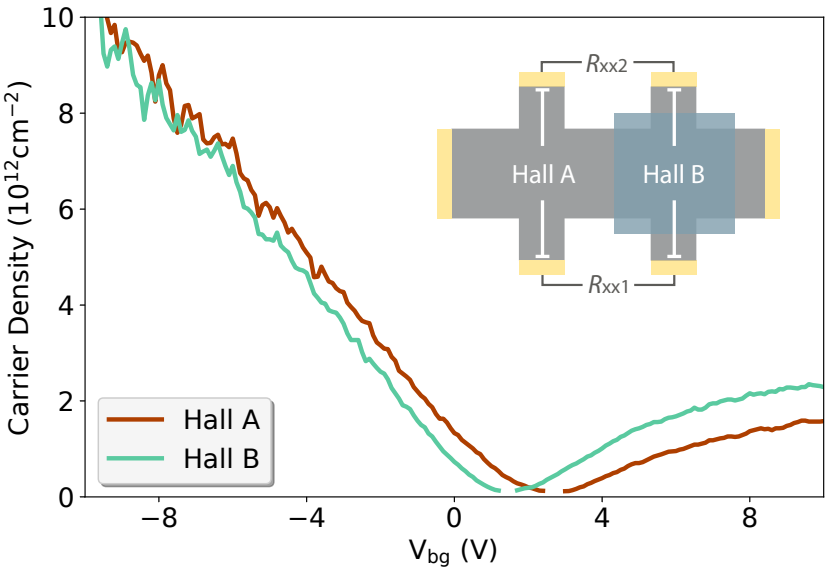

Figure 41: Carrier density of locally doped graphene (Device 1). Carrier densities of the two pairs of Hall electrodes (Hall A and Hall B) are measured at $T = 2$ K. The CNP of the written region (B) is shifted to the left, indicating the doping effect of c-AFM writing. Adapted from [47].

3.2 Graphene band-structure engineering with superlattice

3.2.1 Sketch of superlattice device

When 2D electrons are subjected to both magnetic field and periodic electrical potential, the energy spectrum would exhibit a complex self-similar fractal pattern. This theoretical discovery was first made by Douglas Hofstadter [37]. However, a complete understanding of this spectrum has remained elusive, owing to the stringent experimental condition. The first experimental Hofstadter's butterfly was achieved in GaAs/AlGaAs heterostructures with 100 nm period gates [70]. However, due to the limitation of tuning carrier density, the complete spectrum isn't mapped out. Forty years later after the publication of the theoretical paper, the Hofstadter butterfly was observed in a physical system consisting of two sheets

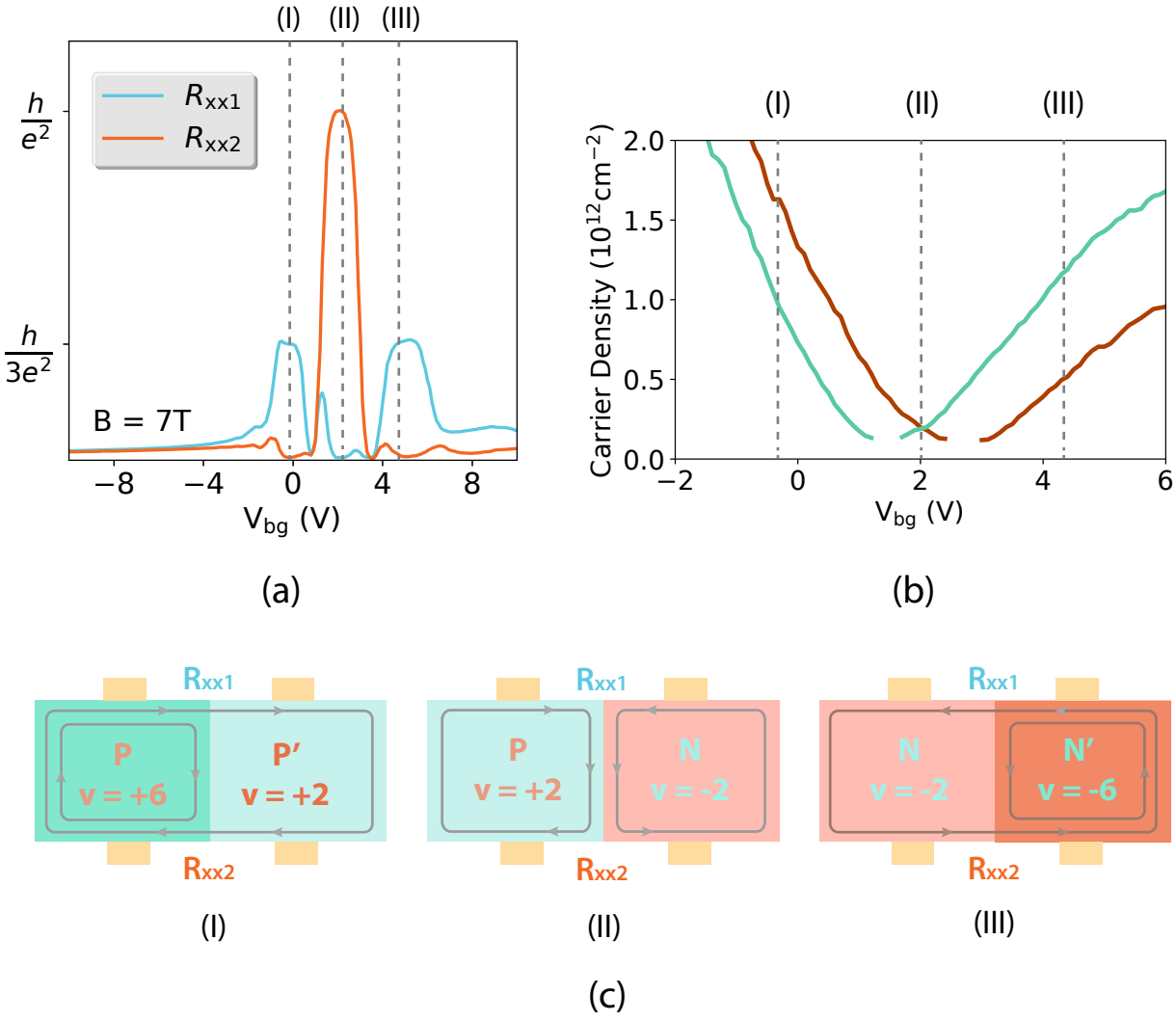

Figure 42: The edge channel mixing changes as V_{bg} is swept from -10 V to $+10$ V (Device 1). (a) R_{xx1} and R_{xx2} are quantized at values predicted by equation 3.2 and 3.3. (b) Zoomed-in plot of Figure 41. (c) Filling factors and edge current directions of the three cases of edge state mixing.

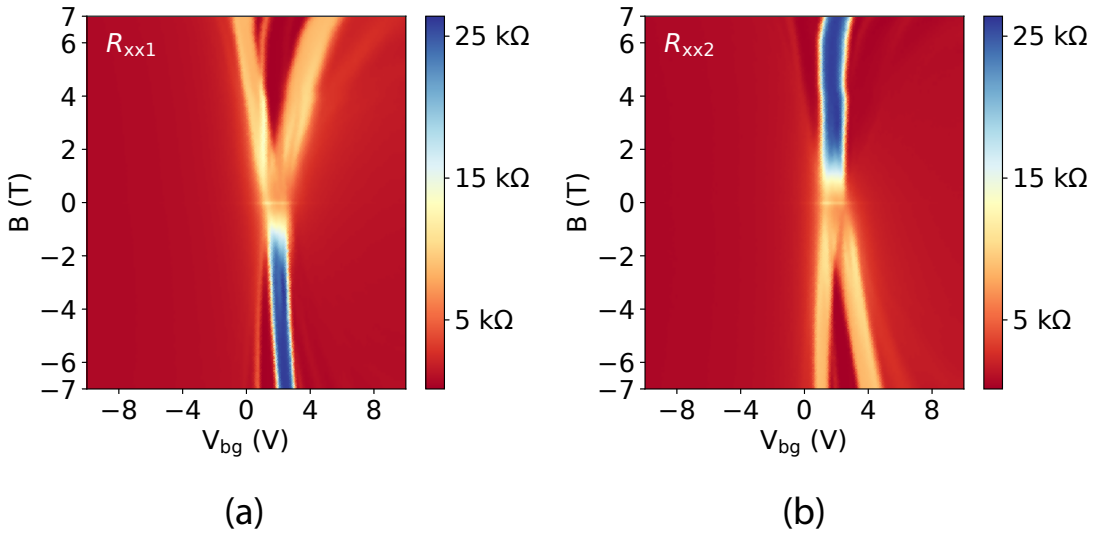

Figure 43: Intensity plot of longitudinal resistance R_{xx1} (a) and R_{xx2} (b) as functions of V_{bg} and magnetic field sweep (Device 1). The values of R_{xx1} and R_{xx2} are swapped when the direction of magnetic field is reversed.

of carbon—graphene—canted at a very small angle to produce a Moire pattern that created the conditions Hofstadter had written about so long ago.

The bilayer graphene coupled to hexagonal boron nitride provides an ideal-sized superlattice size, enabling unprecedented experimental access to the fractal spectrum [22, 39, 64]. In periodic electrical condition, the total number of electron states per area of a completely filled Bloch band is $n_0 = 1/A$. A is the area of the unit cell of the superlattice. In a magnetic field, the number of states per area is B/ϕ_0, where $\phi_0 = h/e$ is flux quantum. Due to the incommensurate periodicity of Bloch and landau sates, the energy diagram yields a butterfly-like self-similar recursive structure known as Hofstadter's butterfly.

Replot the Hofstadter energy spectrum as a function of carrier density and field. All spectral gaps become linear trajectories in the Wannier diagram(density-field diagram). This can be described as:

$$(n/n_0) = t(\phi/\phi_0) + s \tag{3.4}$$

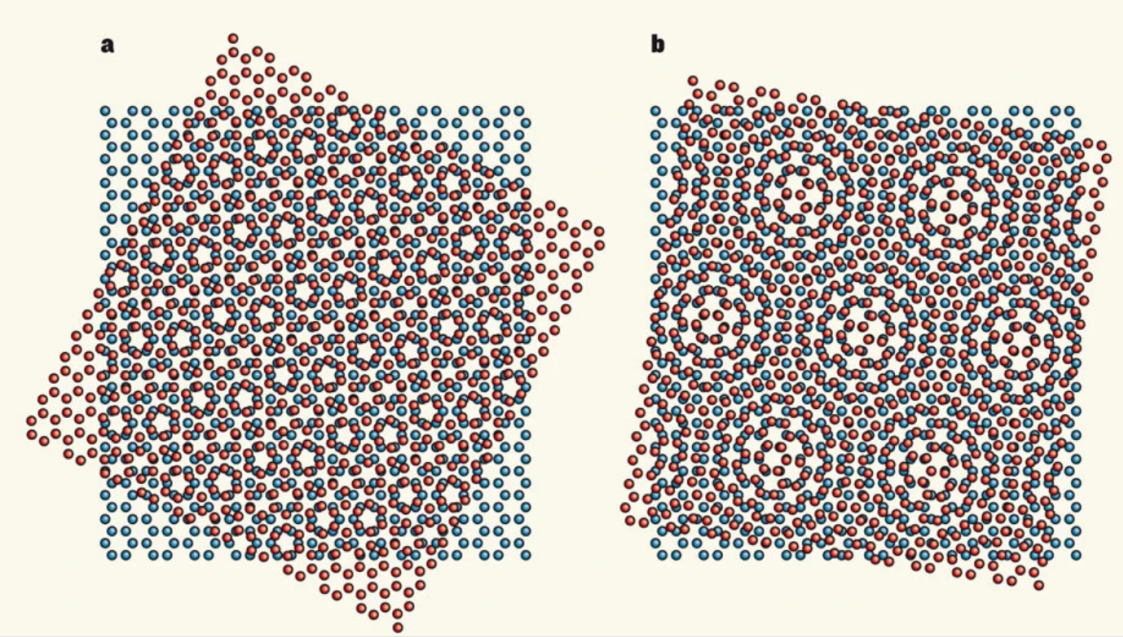

Figure 44: Moiré effect on twisted bilayer graphene. (a) The two lattices are overlaid at an angle of about 27.8°. (b) Lattices rotated by 9°. There are periodic pattern of points in space. Adapted from [51].

Here n/n_0 and ϕ/ϕ_0 are normalized carrier density and flux quantum. Both t and s are integers. t is associated with Landau filling factor since Hall conductivity is quantized as $\sigma_{xy} = te^2/h$. The other quantum number s corresponds to the Bloch band filling index. To observe minigaps clearly, the magnetic length which characterizeds the cyclotron motion, should be the same order as the lattice size. For usual crystal lattices, the required magnetic field would exceed 10,000 T. The main experimental effort is to lithographically fabricate artificial superlattices with the order of tens of nanometers to hundreds of nanometers.

As Figure 45 demonstrates, a graphene device (Device 4) with two Hall bars in series connected is fabricated. The hexagonal pattern is written on the left half of the device, while the other half of the device is measured as control. The current is sourced in the main channel; the resistances for the control device (R_{xx1}) and for the written device (R_{xx2}) are

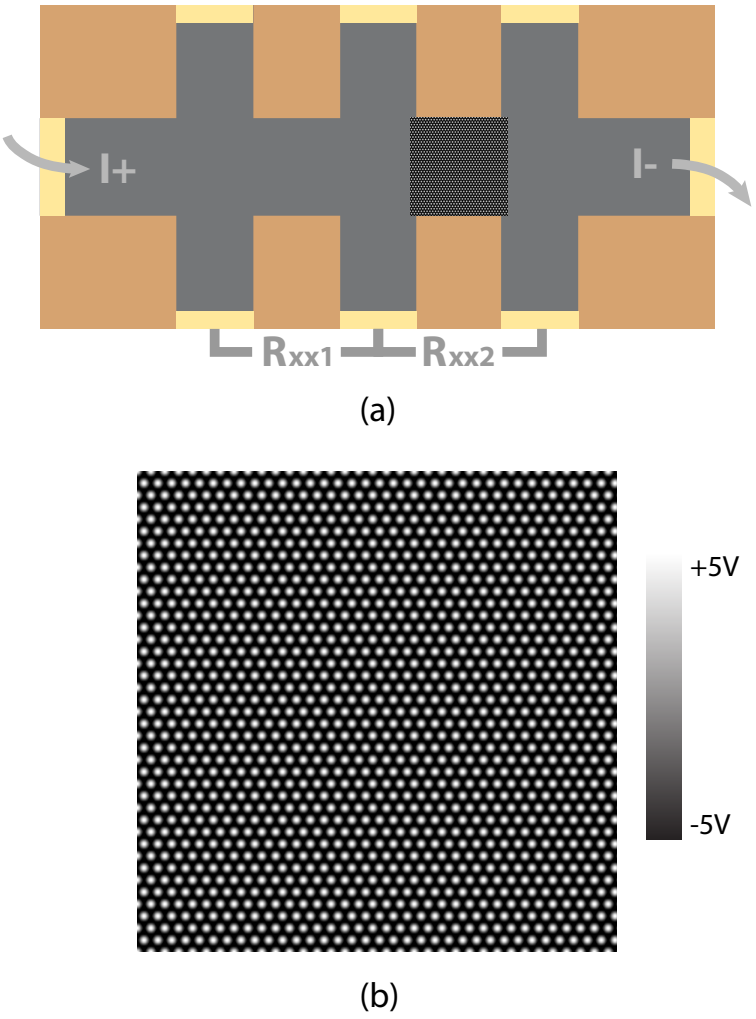

Figure 45: Lithography of hexagonal superlattice on graphene (Device 4). (a) The written and control devices. (b) The hexagonal pattern of superlattice, with $V_{\text{min}} = -5$ V and $V_{\text{max}} = +5$ V. The pattern is generated using equation 3.5. Adapted from [47].

measured. The hexagonal pattern is generated using equation

$$V(x,y) = V_0 \left[\cos(kx) + \cos\left(k \left(\frac{1}{2}x + \frac{\sqrt{3}}{2}y \right) \right) + \cos\left(k \left(\frac{1}{2}x - \frac{\sqrt{3}}{2}y \right) \right) \right] + V_{\text{off}} \qquad (3.5)$$

Where $k = 2\pi/a$ and a is the lattice constant, V_0 is the amplitude of the voltage modulation and V_{off} is the offset (as shown in Figure 45(b)).

The writing of the graphene superlattice is performed with similar parameters in the previous section. The left half of the device is scanned in contact mode, with the bias voltage modulated between -5 V and $+5$ V. For a 5 μm $\times$ 5 μm region, 512 lines are written, at 5 μm/s. The contact force is between 20 nN and 80 nN.

3.2.2 Transport measurement

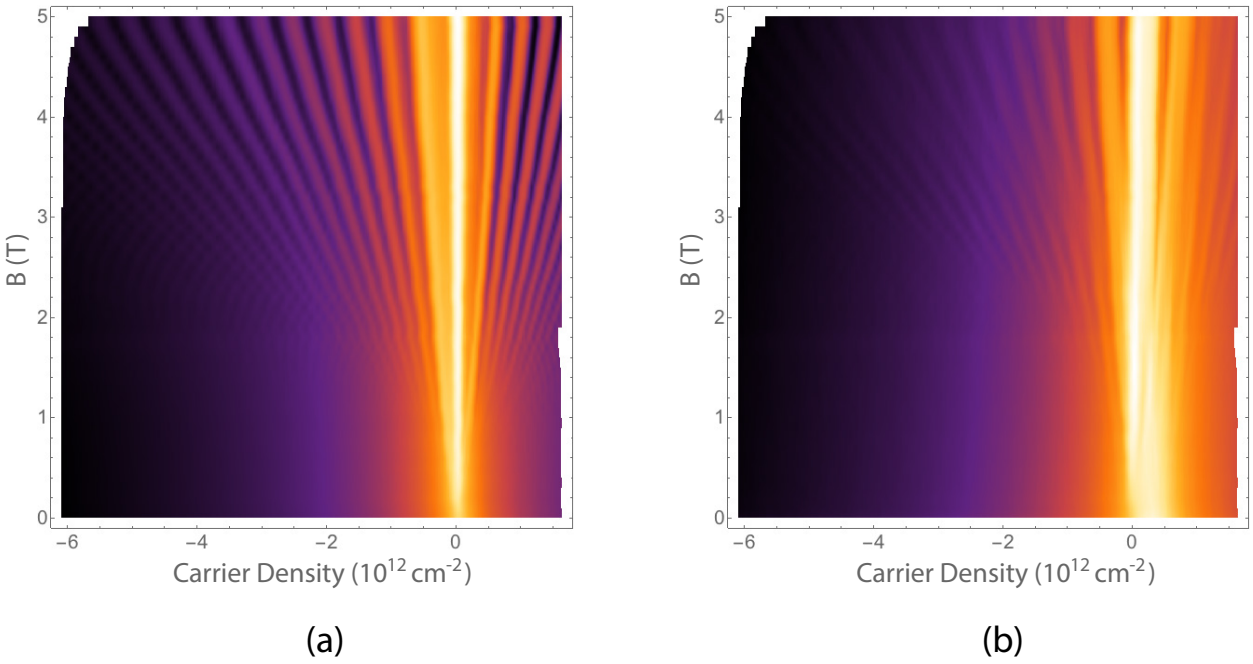

Figure 46: Longitudinal resistance of the control and written Device 4 (R_{xx1} and R_{xx2} in Figure 45(a), in log scale). (a) For the control device, the Landau levels are further apart as the out-of-plane magnetic field increases, and the longitudinal resistance shows a Landau fan diagram. (b) In the graphene with a superlattice written with c-AFM, additional Landau levels are generated from the superlattice and cross the original Landau levels from graphene.

The written and control devices are measured at $T = 2$ K. The results are shown in Figure 46. The longitudinal resistances R_{xx1} and R_{xx2} (as in Figure 45(a)) are plotted as functions of out-of-plane magnetic field and carrier density. The carrier densities are tuned with the back-gate voltage (as in Figure). In Figure 46(a), the Landau fan can be clearly seen in the control device. The superlattice written on graphene is hexagonal, with a lattice

constant of $a = 110$ nm. According to the Wannier theory, the additional Landau fans should start at [22]

$$\frac{n_a}{n_0} = g_s g_v$$

where g_s and g_v are the electron spin and valley degeneracy. In the case of graphene, $g_s g_v = 4$. For hexagonal lattice, $n_0 = 1/A = 2/(\sqrt{3}a^2)$, and therefore the first additional Landau fan should appear at $n_a = 3.8 \times 10^{10}\,\mathrm{cm}^{-2}$. Crossing between the original and additional Lan-dau levels can be observed in Figure 46(b). However, the separation between the origin of the first additional Landau fan and the original Landau fan n_a is smaller than the width of the Dirac peak, and cannot be identified from Figure 46(b). For a typical Dirac peak of graphene on LAO/STO, the full with half maximum (FWHM) is at the order of 10^{11} cm^{-2}. The superlattice constant a has to be smaller than 35 nm so that the first additional Landau fan is clearly observable.

Another factor that complicates the analysis of the data shown in Figure 46 is the permanent writing effect left by c-AFM. When the writing was performed, there was no protection resistor between the voltage source and the c-AFM tip, and the current from the tip to graphene caused permanent structural changes to the graphene (Figure 53). The behavior of electrons in graphene structural superlattice is reported to be different from electrons in graphene potential superlattice [41]. In future experiments, a protection resistor can be connected between the c-AFM tip and tip bias voltage source to avoid accidental oxidation and structural change on graphene to simplify the analysis.

Later on, the MIT team had taken a giant leap by turning two stacked graphene layer into a superconductor by rotating the other sheet to a particular orientation, or 'magic angle' [9, 10]. That twist radically changed the bilayer's properties — turning it first into an insulator and then, with the application of a stronger electric field, into a superconductor. Graphene had previously been turned into superconductor by combining it with materials that were already known to be superconductors, or by chemically doping it with other elements. The development of superconductivity was highly unexpected. At large rotation angle, such misalignment will enlarge the bilayer's unit cell and the energy associated with electron motion between atoms within a layer is dominate. However, at very small rotation

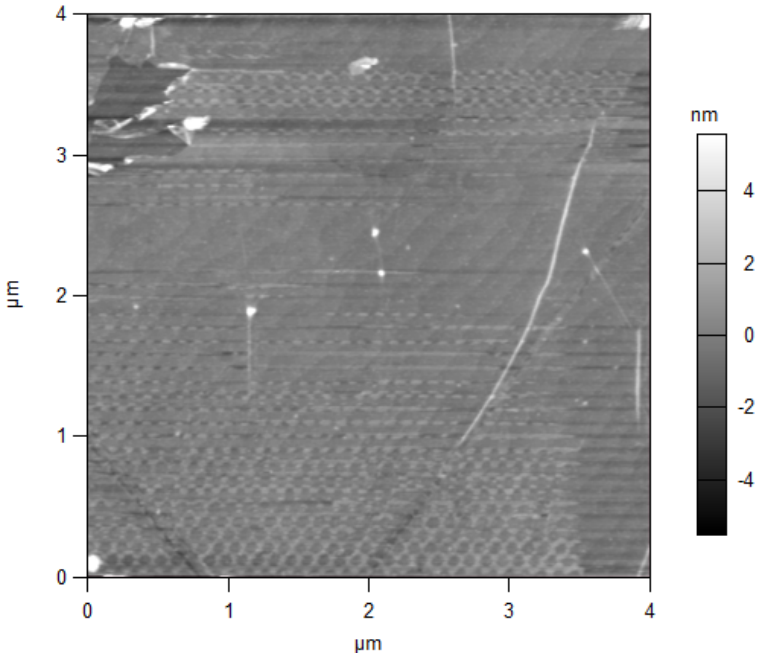

Figure 47: The topographical change of graphene after superlattice c-AFM writing (Device 4). The superlattice pattern written on the graphene is visible on the topography image, and cannot be erased by negative tip voltages, suggesting that permanent structural changes have been caused by c-AFM writing.

angles, the unit cell is greatly enlarged and theory predicts that the low-energy electronic states are entirely reconstructed. Coupling between electrons in the different layers becomes strong. Moreover, electrons can be added or depleted to this twisted bilayer graphene to study the charge transport properties depend on the filling of the energy bands. When the density is corresponding to complete filling of the bands, a robust insulating behavior was observed, which is a strongly correlated, non-conducting Mott insulator state. Even more surprising is what happens when more charge carriers are added to the mott-insulator states. The resistance dropped to zero at about 1.7 Kelvin! Given the very low carrier density, the transition temperature is remarkably high. This twisted bilayer graphene therefore become a new platform to investigate the mechanism of unconventional superconductivity.

3.3 STM doping patterns in graphene/LAO/STO

Local control of charge doping in 2D systems opens the gate of the study of new phenomena including electronic lensing [15, 90], Klein tunneling [93, 95]. The fabrication of nanostructures exhibiting such doping, however, requires sophisticated lithography procedures that compromise sample quality and do not yield flexible control of doping patterns [89, 62, 38, 49, 50, 84], thus hampering advancement in these areas [83]. Some progress has been made in patterning buried GaAs/AlGaAs heterojunctions via a lithography-free conducting AFM tip-based technique [20]. For graphene/BN heterostructures, it has been shown the graphene charge neutrality point can be changed locally in nanoscale [20]. Furthermore, local doping on graphene/BN has also been achieved by the STM tip in an atomic scale [83].

This work is collaborated with Dacen Waters from Dr. Randall Feenstra's group at Carnegie Melon University. The tunability of conductance at LAO/STO interface makes it a great platform for STM doping. Here we use STM to dope graphene with LAO/STO substrate locally. Figure 51 shows the scheme that we used for creating our rewritable doping patterns in a graphene/LAO/STO heterostructure contacted by gold electrodes. A bias voltage V_s is applied to either sample or tip. Tunneling current from tip to sample establishes when the tip is close enough to the sample surface. A backgate voltage V_g applied to the bottom of the STO substrate permits global tuning of the graphene doping level. The interface gate V_{in} allows the tuning doping level of graphene with less hysteresis. Local doping at nanoscale is achieved by the STM tip pulse.

The LAO/STO is 3.4 uc which is the critical thickness of LAO. graphene/LAO/STO is processed with the recipe as describe in Chapter 2. As shown in Figure 51(a), two kinds of gold electrodes are fabricated on the device. One Kind is graphene electrodes which are deposited directly on LAO, only making electrical contact to graphene. The other kind is interface electrode. While doing STM, voltage V_{bias} is applied to the graphene, the tip is grounded. Tunniling current flows from graphene to tip. This is equivalent to applying voltage -V_{bias} to tip and ground the sample. Tip pulsing is performed by add pulsing voltage -V_{s} to sample. This is also equivalent to add pulsing voltage V_{s} to tip. Backgate voltage is

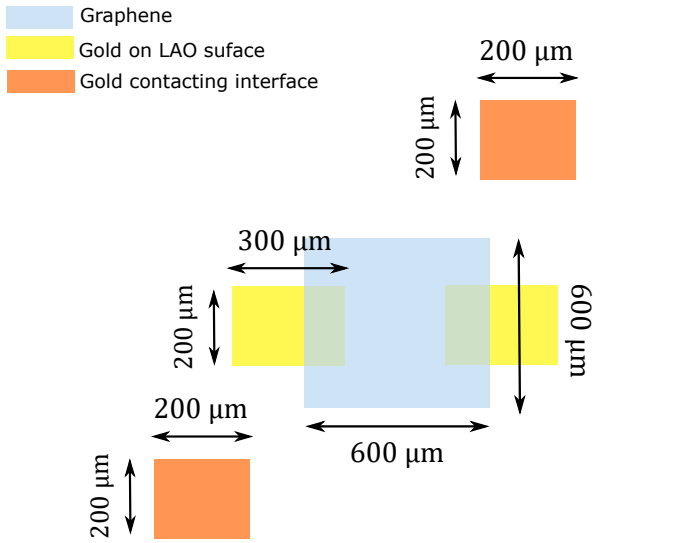

(a)

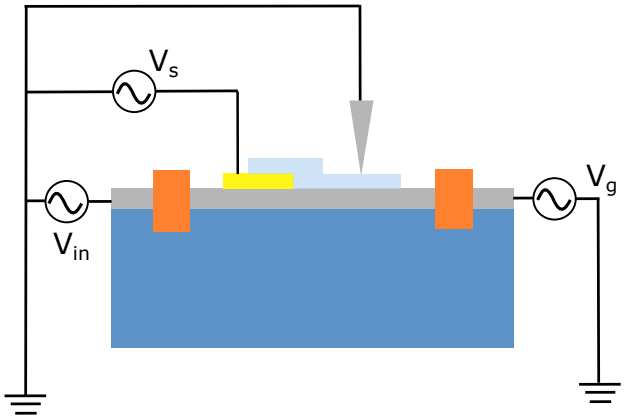

(b)

Figure 48: Schematic for creating rewritable nanoscale doping patterns on graphene and LAO/STO (Device 5). (a) Top view of STM local doping set up. (b) Side view of the set up.

applied to the backside of STO. Due to the hysteresis behavior of the backgate sweeping we metioned before, interface electrodes are used to apply interface gating voltage V_{in}.

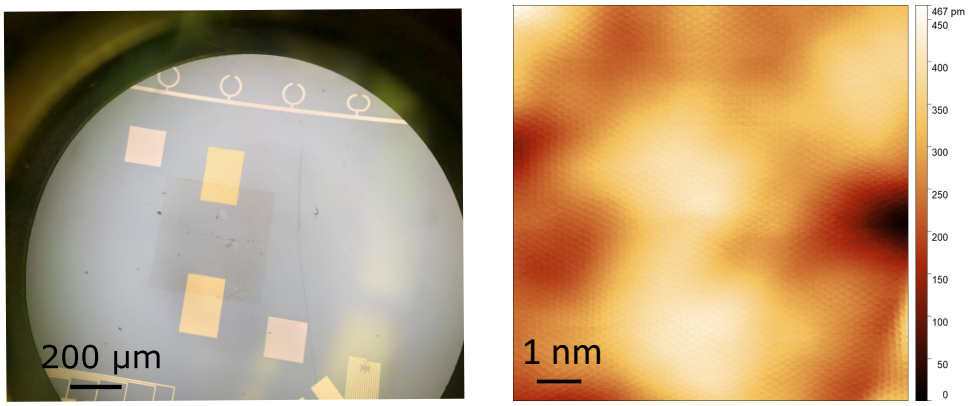

Figure 49: Graphene on LAO/STO (Device 5). (a) Device under optical microscope (b) STM topography at low temperature.

The sample was annealed at 280°C in ultra-high vacuum overnight, then 350°C for 10 minutes. The additional annealing process can effectively remove the residue on top of graphene. The optical image of graphene/LAO/STO is shown in Figure 49. A micro-meter scale CVD grown graphene is transferred on LAO/STO and patterned into a rectangular shape. The dI/dV map of pristine graphene/LAO/STO in Figure 49(b) has clear honeycomb pattern. The charge variance is due to the limitation of the wet transferring method. Otherwise it will exhibit a smooth charge landscape.

We explore microscopic spatial fluctuations of Device 5. In Figure 50, the spectroscopy is studied over a 10 nm distance. The spectroscopy in Figure 50 bottom figure shows the Fermi level of this particular sample is quite uniform, except some variation near when the distance is about 5 nm. This corresponds well with the generally uniform dI/dV map in Figure 49. The valley in the spectroscopy is the phonon mode of graphene.

To directly visualize the nanoscale characteristics of a global Fermi level tuning, we first performed STM measurements on graphene/LAO/STO heterostructure while applying backgate voltage. Figure 49 shows differential conductance (dI/dV) maps obtained at constant sample bias V_s and various backgate voltage $\widetilde{V}_g$. Here $\widetilde{V}_g$ denotes the gate voltage applied during a dI/dV measurement. V_g denotes the gate voltage applied during tip pulsing. These

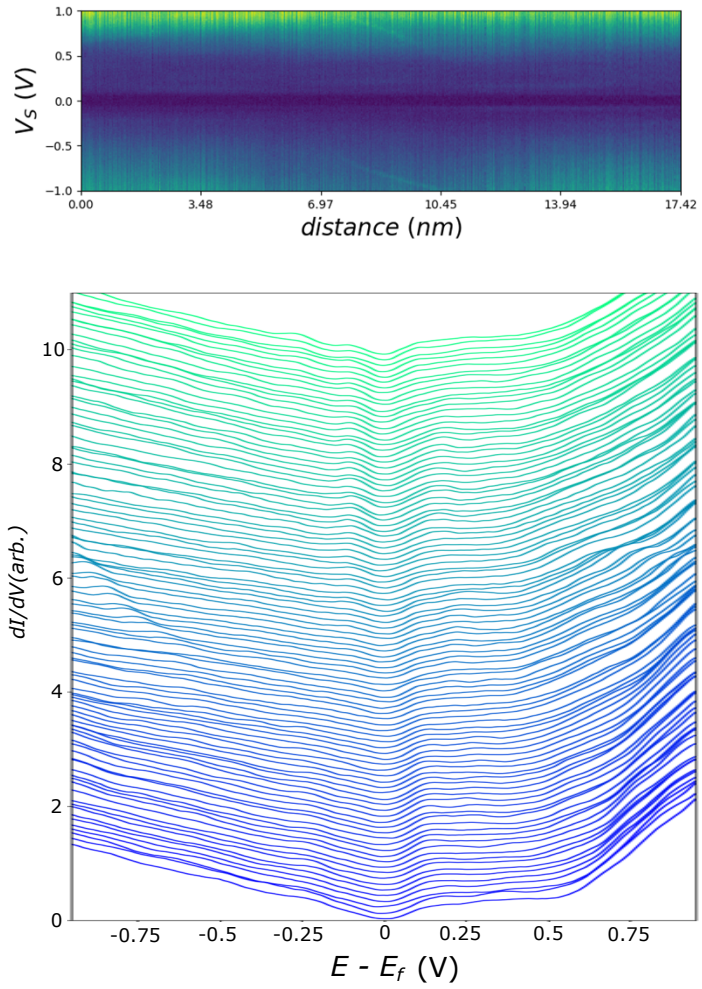

Figure 50: The dI/dV spectroscopy at different locations (Device 5). The curves are vertically offset for clarity. The Fermi level is uniform over this area.

measurements were performed at the same location. We can clearly see the Dirac point is shifted from right to left as the backgate voltage $\widetilde{V}_g$ is varied from 0 V to 30 V and shifted from left to right when $\widetilde{V}_g$ is varied from 30 V to -30 V. The overall feature of each spectroscopy is persevered after a backgate voltage cycle. The Fermi level in graphene can be tuned effectively with backgate and measured by tunneling spectroscopy.

The varying of dopant that results from a tip pulse is studied by performing dI/dV spectroscopy before and after tip pulsing. In Figure 51, dI/dV spectroscopy are all measured

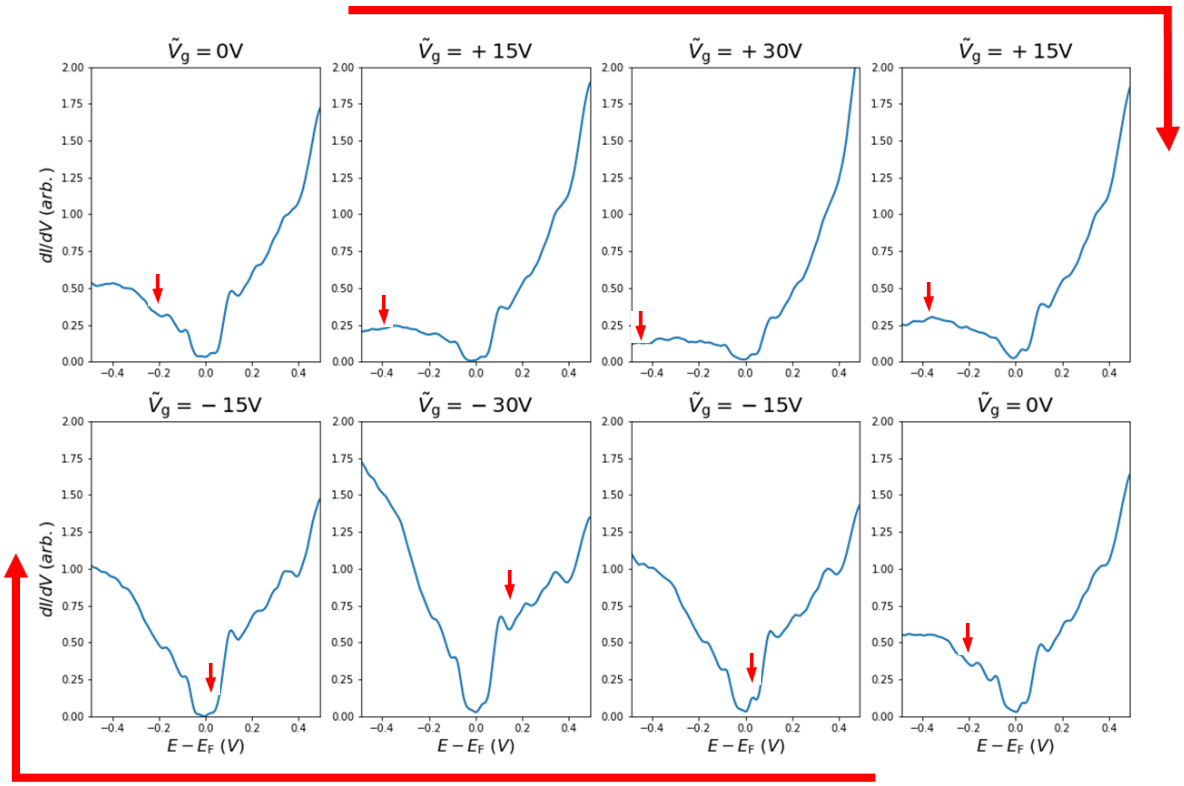

Figure 51: The dI/dV spectroscopy of a pristine surface before a backgate cycle (Device 5): $\widetilde{V_g}$ varies from 0 V, 15 V, 30 V, 15 V, 0V, -15 V, -30 V, -15 V. The small red arrows are indicators of the Dirac point. The Dirac point shifts when the Fermi level is tuned by backgate.

with backgate $\widetilde{V_g} = 0$V. The pulsing time is $t = 5$ s. When tip pulse $V_s = 3.5$ V and backgate $V_g = -30$ V, the tip pulse can successfully shift the Dirac point. In the third graph, with tip pulse $V_s = 3.5$ V, and backgate $V_g = 0$ V, the Dirac point remains the same. The Fermi level reverse to the pristine state when $V_s = 4.0$ V. Thus a erasing process is achieved. In the future, the shape of the doping pattern can be imaged by performing a dI/dV map before and after tip pulsing.

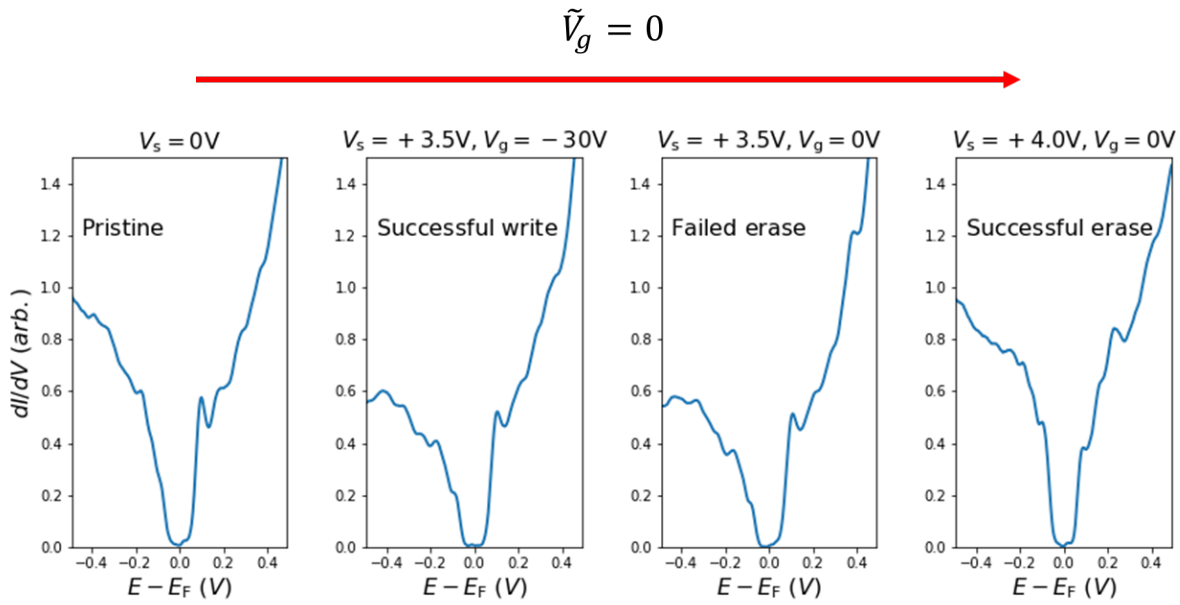

Figure 52: Tip pulse for writing and erasing (Device 5). The dI/dV spectroscopes are measured with backgate $\widetilde{V}_g = 0$. When tip pulse $V_s = 3.5$ V, and backgate $V_g = -30$ V, the tip pulse can successfully shift the Dirac point. In the third graph, with tip pulse $V_s = 3.5$ V and backgate $V_g = 0$ V, the Dirac point remains the same. In the last graphene, by increase tip pulse voltage, the Fermi level reverse to the pristine state.

3.4 Magneto-optical kerr effect on LAO/STO interface

Even though both LAO and STO are non-magnetic materials, the magnetism is observed within the interface of LAO/STO. This emergent property of LAO/STO has attracted researchers for a long time. The explanations are still controversial.

The first signature of magnetism at the LAO/STO interface is reported in 2007 by Brinkman *et.* al [7]. Beside, magnetism is reported by other observations of anisotropic magnetoresistance [5,7-13], anomalous Hall effect [11,14-16], and direct observation of magnetization with tools from cantilever magnetometry [17], scanning SQUID magnetometry and susceptometry [18-20], magnetic force microscopy [21,22], and x-ray magnetic circular

dichroism [23,24]. The magnetic phases involve local magnetic moments and their coupling to itinerant electrons.

The oxygen vacancies at the interface localize electrons in nearby Ti 3d states. Similar oxygen vacancies at the surface of STO may also introduce ferromagnetic order [59]. These localized states are located either in the Ti d_xy orbitals [60,61], or the Ti e_g orbitals [62-64].

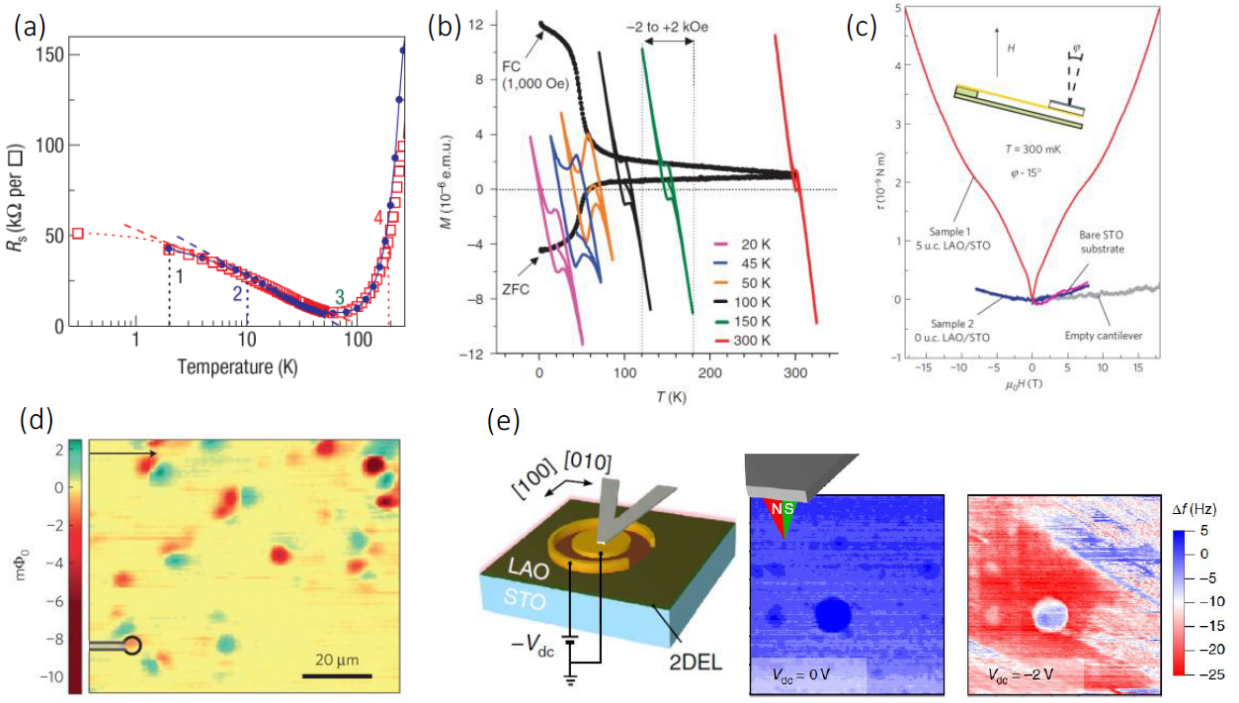

Figure 53: Experimental evidence for ferromagnetism at the LAO/STO interface. (a) Kondo resistance minimum. (b) SQUID measurement: hysteresis loops took at different temperature superimposed on top of the temperature dependence of magnetic moments. (c) Cantilever-based magnetometry: the magnetic moment induced a torque under an external magnetic field, the magnetization of the sample is inferred accordingly. (d) With a micrometer-sized SQUID on a probe tip, microscopic magnetization can be imaged. Dipole-shaped patches are observed. (e) Electrically-controlled ferromagnetism observed with a magnetic force microscope. The magnetism signal is observed only when the interface is insulating. Adapted from [63].

3.4.1 Magnetic force microscopy at LAO/STO interface

It has been proved that the magnetism at LAO/STO has thickness dependence. The LAO thickness window for ferromagnetism is from 8 u.c to 25 u.c. This thickness exceeds the critical thickness of 2DEG gas formation. Therefore the interface is conducting as grown. The magnetism is found to be gate-tunable at room temperature by magnetic force microscopy(MFM). The itinerant electrons will screen the interface magnetism so the in-plane magnetism can only be observed when the interface is insulating. MFM experiment setup is shown in Figure 54. The gold topgate is patterned into a circular shape, and the interface is patterned to a concentric arc. By applying a voltage to the interface electrode or topgate electrode, the electrons are depleted at the interface. As shown in 54(b) and (c), top-gate is grounded while -3 V to 0.5 V voltage is applied to the interface electrode. When interface voltage is smaller than -0.5 V, the capacitance and leakage current between interface and topgate is nearly zero. When the interface is insulating, a stripe-like Magnetic signal is shown in 56. When the voltage exceeds -0.5 V, iterate electrons screen the magnetism, the strip-liked feature disappears.

MFM can be used for finding magnetic patches on a sample. Later on, the magnetism on this sample can be further verified by magneto-optic Kerr measurement. With the femoto pulse laser, magneto-optic Kerr measurement can perform time-resolved experiments.

3.4.2 Magnetic circulardichroism spectroscopy at LAO/STO interface

The magnetism has been discovered in oxygen-deficient STO with magnetic circular dichroism(MCD) spectroscopy [69]. Circularly polarized light can induce long-lived magnetic moment in slightly oxygen-deficient but otherwise nominally pure STO crystals. These magnetic signals, which are induced at zero applied magnetic field and at temperatures below 18 K, can be controlled utilizing the circular polarization and wavelength of sub-bandgap illumination.

The bare STO substrates show only the band-edge absorption at 380 nm. In contrast, oxygen-deficient STO develops an additional sub-bandgap absorption peaked at around 430 nm with a weak shoulder at 400 nm. At zero magnetic field, the STO sample is pumped

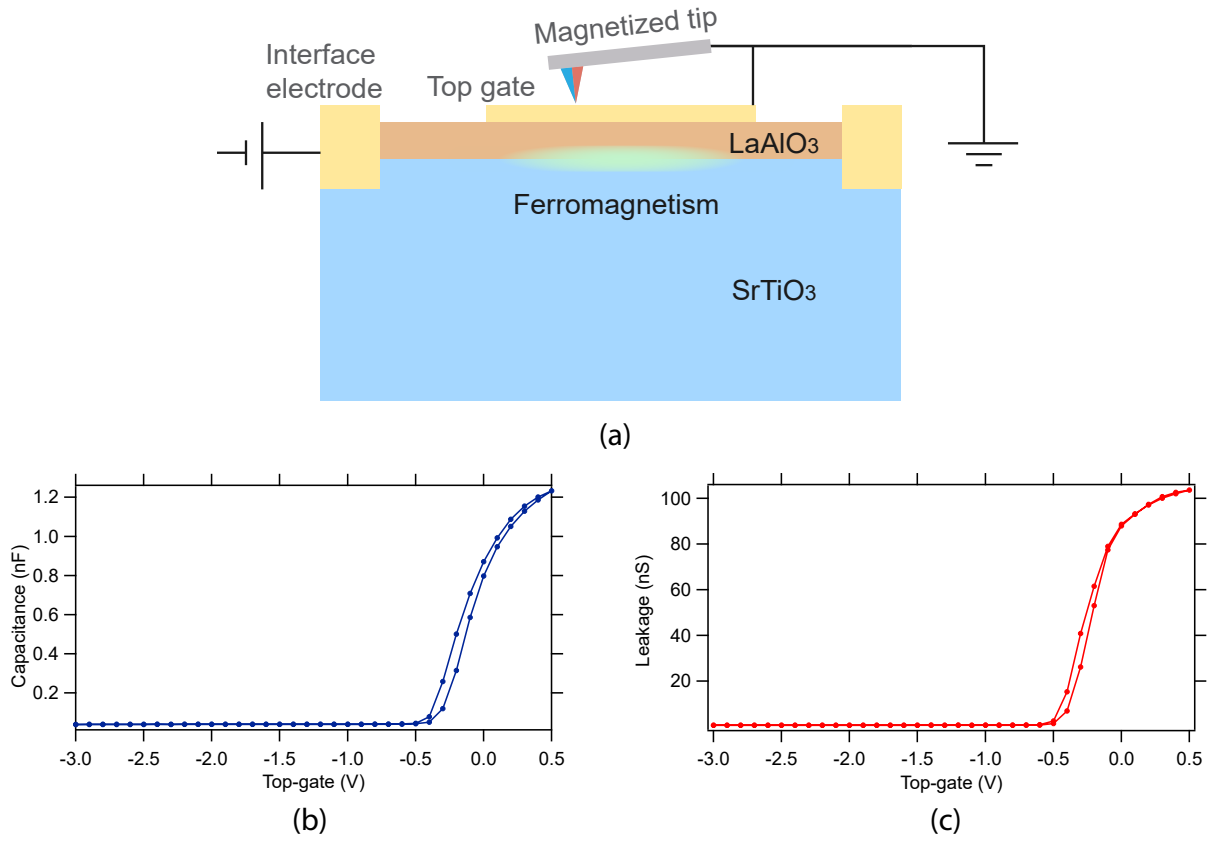

Figure 54: MFM measurement (Device 6). (a) Experiment setup. The sample within the ferromagnetism thickness window of LAO (8 u.c. to 25 u.c.) is patterned with a top gate electrode and interface electrode [6]. The top gate is grounded. The interface and top gate form a capacitor. A positive voltage of +1 V to +3 V is applied to the interface. The interface electrons at the interface are depleted. The MFM tip coated with 50 nm of Co/Fe alloy is magnetized in the in-plane direction. The MFM signal is measured when the tip is 50 nm away from the sample surface. (b) and (c) are the capacitance and leakage current between the interface and top gate, as functions of the voltage difference between the interface electrode and top gate. The top-gate voltage in (b) and (c) is equal to the potential on the negative voltage since two gates is grounded. When the top-gate voltage is smaller than −0.5 V, both the capacitance and leakage are close to zero, which means the interface carriers are depleted. Adapted from [47].

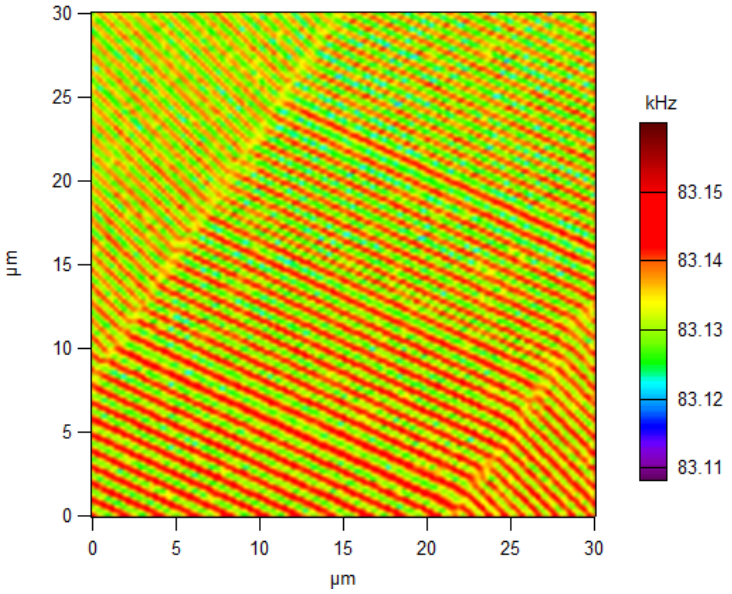

Figure 55: MFM Tip test. Before performing MFM on LAO/STO, the tip by magnetized by a electromagnet and tested by scanning on a magnetic tape.

with a sub-bandgap circularly polarized light at $\lambda_{\text{pump}} = 405$ nm through the entire sample thickness. A robust MCD signal is observed at 400 nm, 425 nm, and 455 nm. The MCD signal only exists when pump light is circularly polarized and inverts when pump light changes from left-circularly polarized to right-circularly polarized. This pump-induced magnetism appears only at $T < 18$ K.

3.4.3 Magneto-optical Kerr effect

Unlike MCD, magneto-optical Kerr requires the detection of the reflected light. Magnetism is induced at the LAO/STO interface by applying a gate voltage. The light reflected from a magnetic LAO/STO interface is measured and responds reversely to LCP and RCP pump light.

The Jone's matrix is a convenient tool for describing polarized light. Suppose a monochromatic plane wave travels in z direction with angular frequency ω, the complex amplitude of $\mathbf{E}$ in x, y plane is:

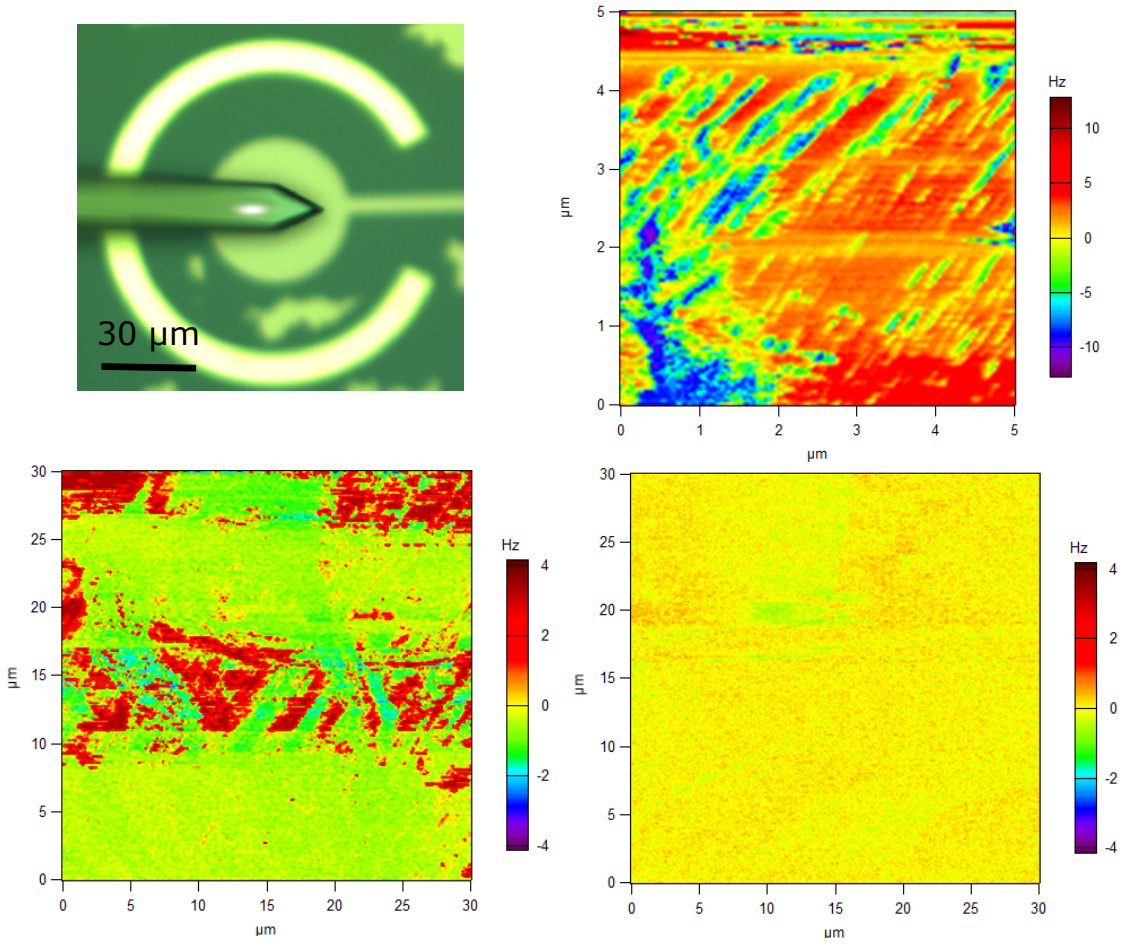

Figure 56: Optical image of the MFM device and MFM signal for interface magnetism (Device 6). The circular shape region is the top gate, and the arc-shaped electrode is the interface electrode. Top right: MFM image is scanned on a 5 μm $\times$ 5 μm region on the top gate while the electrons are depleted. Diagonal stripes are visible in the MFM image. Bottom left: MFM in 30 μm scale. When electrons are depleted from the interface, magnetic patches emerge. Bottom right: Magnetism is screened by the electrons when the interface is conducting.

$$\mathbf{E} = \begin{pmatrix} E_x \\ E_y \end{pmatrix} = \begin{pmatrix} E_{0x} e^{i\phi_x} \\ E_{0y} e^{i\phi_y} \end{pmatrix} e^{i(kz-\omega t)}$$

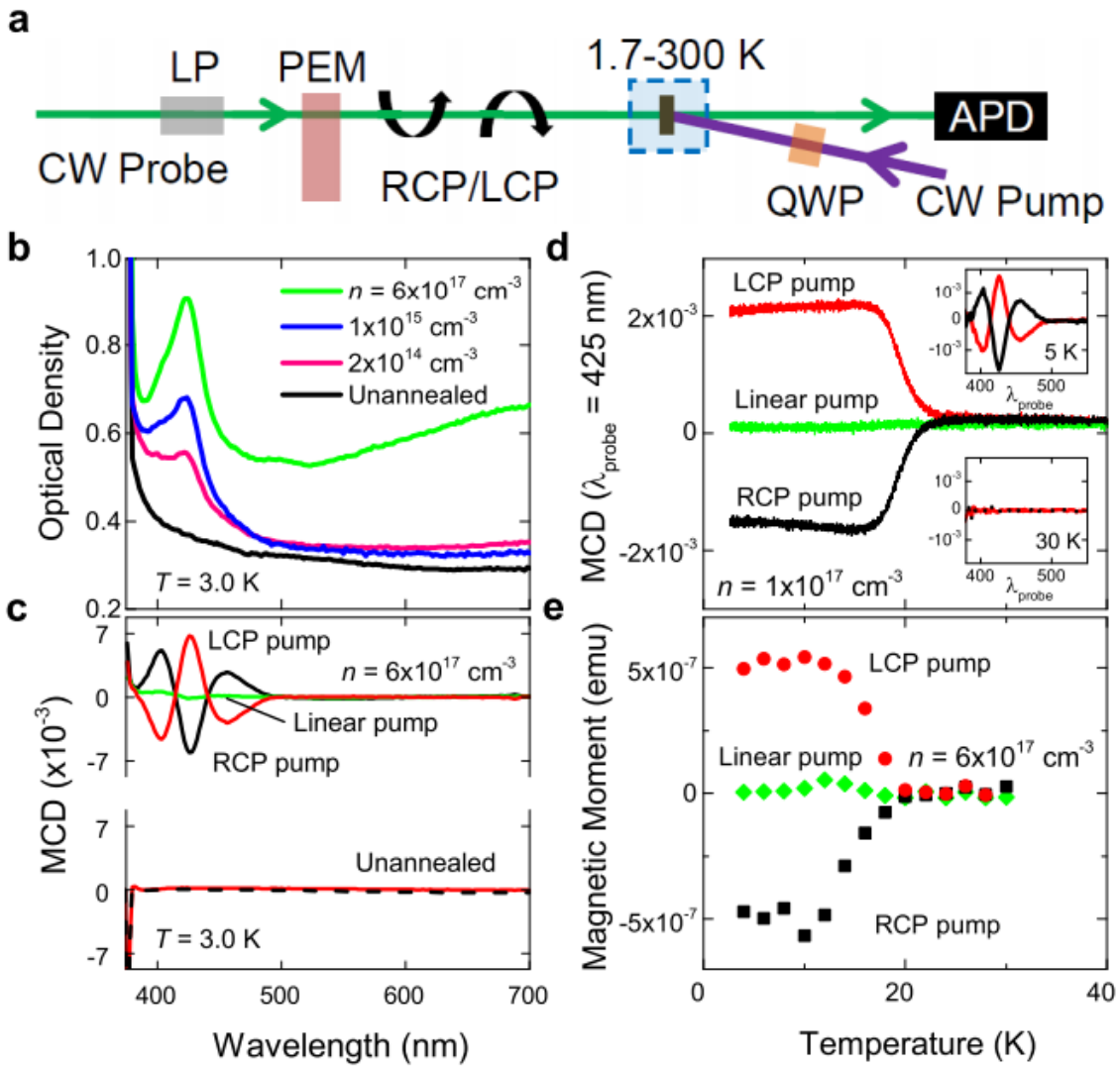

Figure 57: (a) Pump-probe measurement of MCD signal in oxygen-deficient STO at zero applied magnetic field. (b) Optical absorption spectrum of oxygen-deficient STO. The samples are denoted by their carrier densities. (c) MCD spectrum of LCP and RCP pump light. (d) MCD as a function of temperature. (e) Corresponding magnetic moment as measured by SQUID magnetometry, showing similar behavior as (d). Adapted from [69].

The time independent part is called the Jones vector, which can be used to describe the phase and amplitude of the electric field in x and y direction. Increase ϕ_x or ϕ_y introduces

retardation in phase. Linearly polarized light in the x direction and y direction can be written as:

$$|H\rangle = \begin{pmatrix} 1 \\ 0 \end{pmatrix}, \quad |V\rangle = \begin{pmatrix} 0 \\ 1 \end{pmatrix}$$

the left- and right-hand circular polarized (LCP and RCP) light can be written as

$$|L\rangle = \frac{1}{\sqrt{2}} \begin{pmatrix} 1 \\ i \end{pmatrix}, \quad |R\rangle = \frac{1}{\sqrt{2}} \begin{pmatrix} 1 \\ -i \end{pmatrix}$$

The Jones matrices are operators that act on the Jones vectors. For example, linear polarizer at $\pm 45^\circ$

$$\frac{1}{2} \begin{pmatrix} 1 & \pm 1 \\ \pm 1 & 1 \end{pmatrix}$$

and a phase retarder

$$\begin{pmatrix} 1 & 0 \\ 0 & e^{i\delta} \end{pmatrix}.$$

Light can change intensity and polarization when reflected from a magnetic surface. Kerr effect results from the off-diagonal components of the dielectric tensor ϵ. The permittivity is anisotropic in different directions. The speed of light in a material is affected:

$$v_p = \frac{1}{\sqrt{\epsilon\mu}} \tag{3.6}$$

The light speed depends on different directions. This causes the phase retardation of polarized light in different directions.

The photoelastic modulator(PEM) offers a very sensitive method of measuring low levels of retardation. PEM is made by mechanically stressed birefringence material that has a different refractive index along different axes. A current is sent through to vibrate the optical elements through stretching and compressing. Thus the birefringence of the transparent material changes with a certain frequency. A PEM is limited to a single frequency, usually around 50 kHz. After PEM, a phase is added to the light.

$$\begin{pmatrix} e^{-i\delta/2} & 0 \\ 0 & e^{i\delta/2} \end{pmatrix}.$$

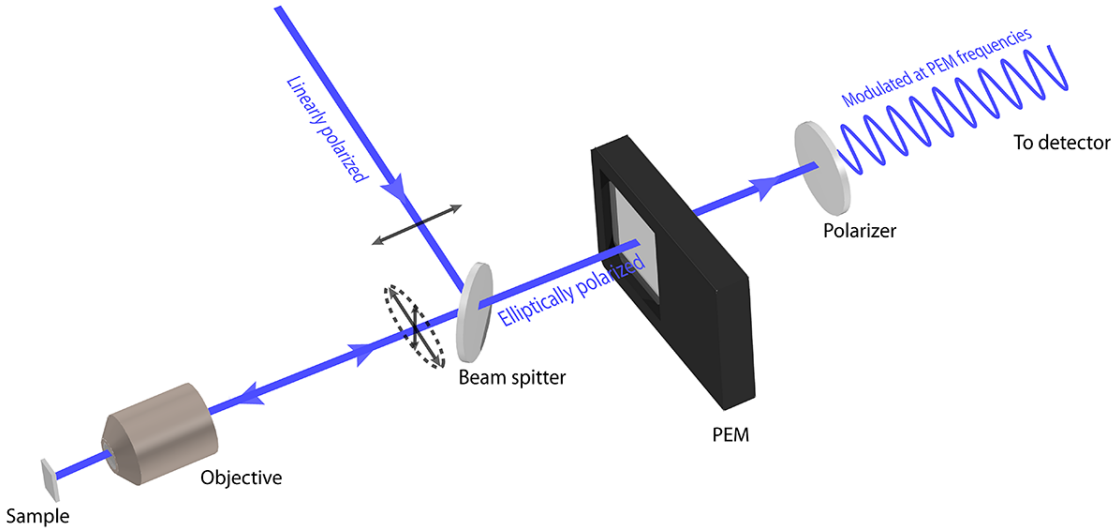

Figure 58: The PEM measurement setup. Linearly polarized light is reflected by a beam splitter and travels towards the sample. The reflected light is elliptically polarized due to the magnetization of the sample surface. A PEM then modulates the reflected polarized light. The polarization modulation is converted to intensity modulation. After PEM, the light intensity is detected by a quad detector. Adapted from [47].

with $\delta = A_0 \sin(\omega t)$. A_0 is the amplitude of phase modulation, and ω is the oscillation frequency of PEM. After PEM, the light beam is modulated between LCP and RCP at the modulator frequency of $1f$.

As Figure 59 shows, the incident laser is linearly polarized and reflected by a beam splitter towards the sample. The beam is focused by an objective and reflected from the magnetized surface, and the becomes elliptically polarized. The reflected beam goes through the beam splitter again and is then modulated by the PEM. The polarization modulation is then converted to intensity modulation with another polarizer. The signal is finally measured with a silicon detector.

Using Jone's matrix formalism, the intensity is described by [3],

$$I(t) = I_0[1 + 2\theta_k \cos(A_0 \cos(\omega t)) - 2\epsilon_k \sin(A_0 \cos(\omega t))]$$

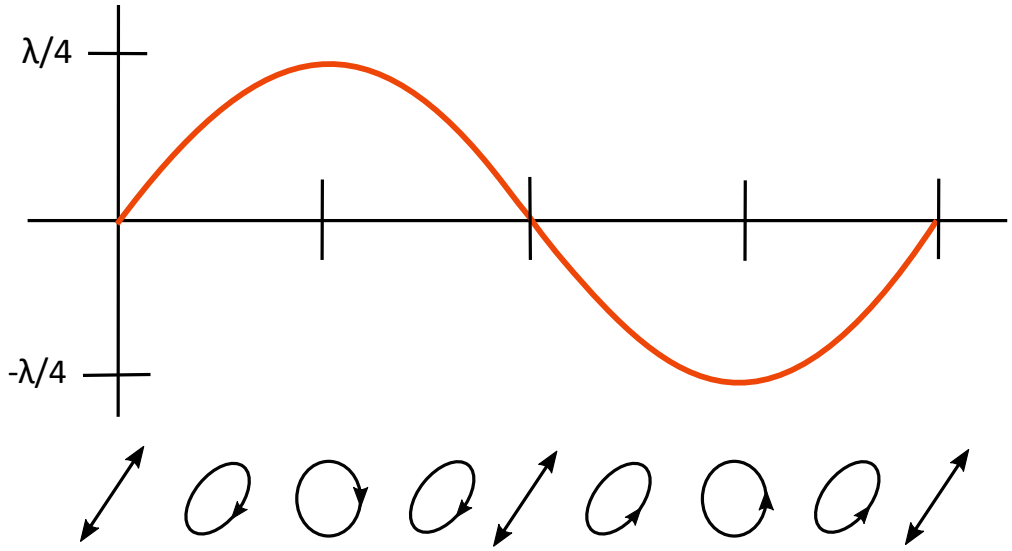

Figure 59: The light is modulated into linear polarized light, LCP, linear polarized light, RCP, linear polarized light etc. as a function of phase retardance.

assuming the phase retardation from the PEM is $\delta_p = A_0 \sin(\omega t)$. The above expression can be expanded using Fourier series

$$I(t) \approx I_0[1 + 2\theta_k J_0(A_0) - 4\epsilon_k J_1(A_0)\sin(\omega t) + 4\theta_k J_2(A_0)\cos(2\omega t)]$$

where J_0 and J_1 are the 1st and 2nd order Bessel functions. The rotation angle θ_k and ellipticity ϵ_k can be distinguished using lock-in amplifiers modulated at ω and 2ω,

$$\theta_k = \frac{\sqrt{2}}{4J_2(A_0)}\frac{V_{2f}}{V_{\mathrm{DC}}}, \quad \epsilon_k = \frac{\sqrt{2}}{4J_1(A_0)}\frac{V_{1f}}{V_{\mathrm{DC}}},$$

where V_{1f} and V_{2f} are the voltage signals at 1st and 2nd harmonic of the PEM modulation frequency, and V_{DC} is the DC voltage offset.

3.4.4 Magnetic-optical kerr at LAO/STO interface

The set up for measuring magnetism at the LAO/STO interface is shown below. To match the in gap state of oxygen vacancies, the incident light wavelength is chosen to be 425 nm. Pulsed laser centered at 850 nm with a power of 1.4 w is generated from a spectra-physics Millennia 532 nm laser with a power of 9.6 W. The pulse laser's frequency is doubled after a beta barium borate (BBO) crystal. The generated 425 nm laser has a maximum power about 20 mW. The second harmonic generation process requires high input intensity, so the light is focused before BBO and collimated after BBO. The isolator between BBO and 850 nm pulsed laser prevents the back reflection of 850 nm laser from BBO. The reflected light might unstablize the pulsed 850 nm laser.

After BBO crystal, 850 nm laser is attenuated by a 400 $\sim$ 430 nm filter. A higher signal to noise ratio can be reached with higher incident light intensity on the LAO/STO surface. Here a Berek's compensator is added before 0° polarizer. Berek's compensator consists of a plate of uniaxial crystalline material with faces perpendicular to the optic axis. The retardance can be set from 0 to π. Thus the 425 nm laser after Berek's compensator can be set almost parallel to the 0° polarizer to reduce loss. After the polarizer, light splits into two paths. One goes directly to the detector path as a reference. The other one goes to the sample surface, reflected with a phase retardance. Behind beam splitter, two branches of light merge together and go through a PEM. After polarization modulation with PEM at $f = 42$ kHz, the light is again split into two paths. One path goes through a 45° polarizer, the other goes through a 135° polarizer.The two paths are sent into a balanced detector. The subtraction of the parts is measured at $2f$ frequency of PEM by a lock-in amplifier.

The Kerr set-up is firstly verified by a magnetic disk cut from a used hard drive. The small magnetic regions are different magnetic domains magnetized in a different direction. Information is stored in magnetic domains. With our Kerr set-up, we can observe the strip-liked magnetic domains. The optical signal is mapped to each spot of location by utilizing a scanning piezo stage. The scanning speed needs to be carefully chosen. To avoiding thermal drifting, a fast scanning speed is preferred. However, the scanning speed is also limited by the resonance frequency of PEM. The time constant t_c of lock-in amplifier is set to be 1 ms.

Thus scanning a typical 50 μm device takes 6 minutes with a speed of 60 μm/s.

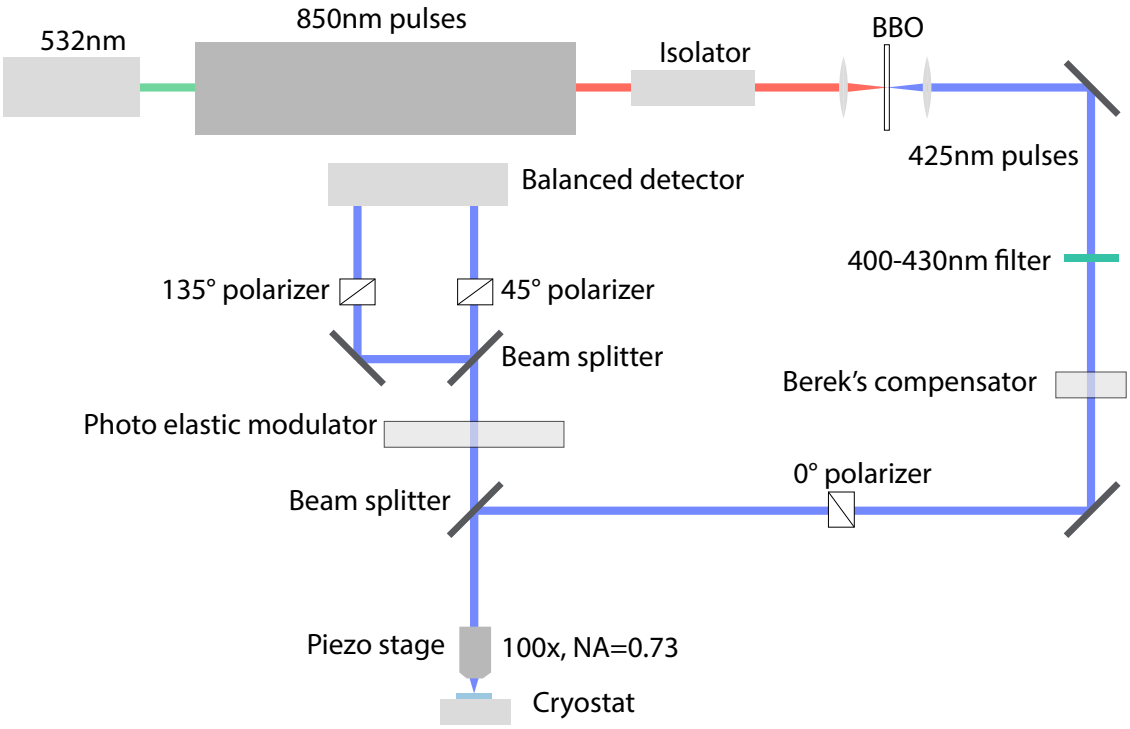

Figure 60: The Kerr rotation measurement setup. $\lambda = 850$ nm pulsed laser is generated from a Tsunami laser and doubled by BBO crystal. $\lambda = 425$ nm laser passes through a band-pass filter and is then horizontally polarized. The laser is focused onto the sample with a 100 $\times$ objective. The objective is fixed on a piezo scanner. The reflected laser is modulated by a PEM and then split into two branches that pass through two polarizers at 45° and 135°. The intensity signal is detected with a balanced detector.

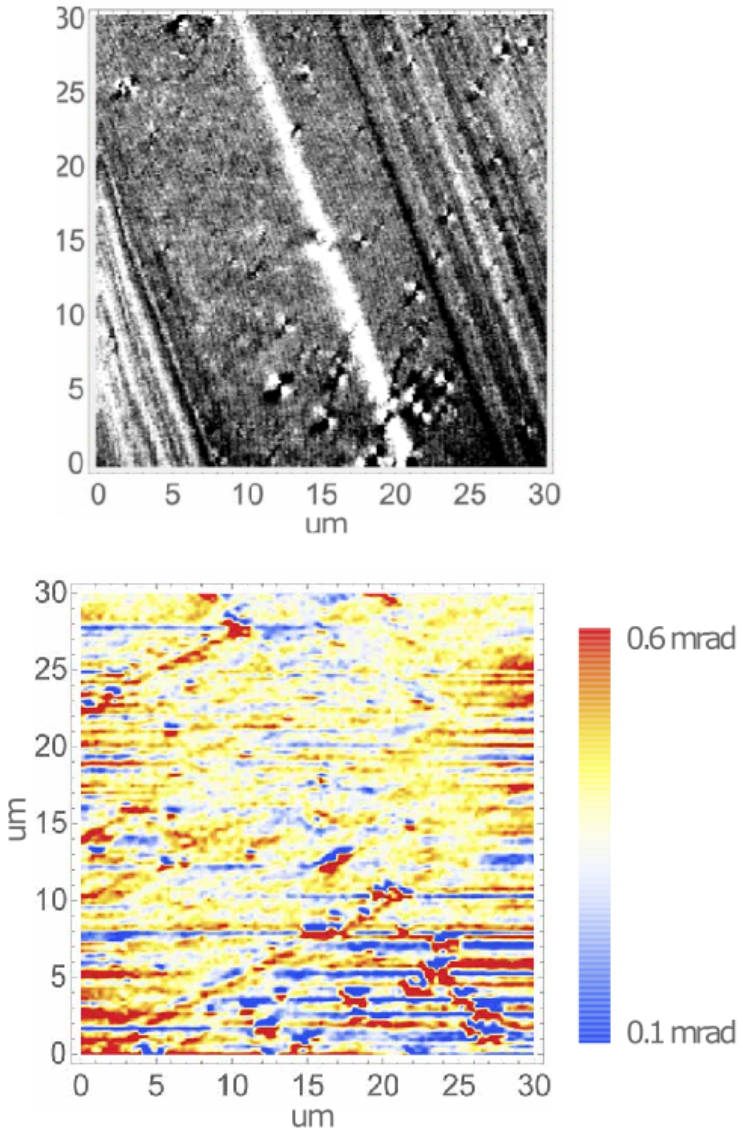

Figure 61: Top: Kerr rotation signal from hard disk. Bot: Kerr rotation signal from LAO/STO (Device 6).

3.5 Coulomb drag between graphene and LAO/STO

3.5.1 Coulomb drag experiments

Heterostructures composed of different layered materials provide novel opportunities to investigate the electronic correlations between them. In this chapter we investigate frictional drag between graphene and $LaAlO_3/SrTiO_3$ (LAO/STO) heterostructures. The LAO/STO layer underneath the graphene is rendered conductive using conductive atomic force microscopy (c-AFM) lithography, creating a two-layer system in which the LAO serves as an ultrathin (< 2 nm) insulating barrier. By sourcing current in the STO layer, strong stripe-like voltage oscillations appear in the graphene Hall bar, both along the main channel and the transverse (Hall) configuration. The behavior is consistent with energy and momentum transfer from the STO layer taking place. In the configuration where current is sourced in the graphene layer, behavior similar to that found in LAO/STO nanowire pairs is observed. Additionally, a large enhancement of drag resistance is observed when the STO becomes superconducting.

3.5.2 Coulomb drag in ballistic region

The full nature and consequences of electronic correlations in two-dimensional electron systems (2DES) remains elusive, even after many decades of intense investigation. Electronic correlations are generally more prevalent in low-dimensional systems, and are known to give rise to phases that are not predicted by electronic band structure considerations alone. In many cases, such as cuprate high-temperature superconductors, it is challenging to "peer inside" these systems, or significantly tune their electronic properties other than through growth. However, relatively new materials 2DES platforms such as graphene and complex-oxide heterostructures offer new opportunities to investigate the effects of strong correlations.

One particularly powerful approach to revealing correlated properties involves a method commonly known as "Coulomb drag", or more precisely, "frictional drag", when the mechanism of interaction is non-Coulombic or unknown. When two electrical conductors are situated in close proximity, current driven through one conductor (the "drive") may transfer

both energy and momentum to the second ("drag") conductor, resulting in a measurable voltage (or current) [55, 79]. The resulting frictional drag provides a uniquely sensitive way to measure the electronic correlations since the drag response depends on interactions without direct exchange of charge carriers. Coulomb drag was extensively studied in GaAs quantum wells [32, 26, 34, 33, 74, 75, 76], where the observations are well explained by momentum drag mechanism. The realization of small separation (only a few nanometers) between bilayer of two-dimensional electron gases (2DEGs) in semiconductor heterostructures lead to the observation of much stronger interactions and the discovery of a superfluid exciton condensate [34]. Both hexagonal boron nitride (h-BN) encapsulated graphene and bilayer-graphene systems have allowed access to a new strong-interaction regime where the interlayer energy transfer dominates [31].

The LAO/STO interface exhibits a hysteretic metal-insulator transition [61, 80], which can be controlled locally using conductive atomic force microscopy (c-AFM) lithography and used to create a range of mesoscopic devices [13, 14]. The LAO/STO interface properties are dominated by the electrons from STO, which exhibit a rich variety of electronically-tunable properties such as superconductivity [12, 68], magnetism [7], and spin-orbit coupling [11] and more [63].

The G/LAO/STO (G stands for graphene) hybrid system allows the study of coulomb drag between superconducting STO and non-superconducting graphene, separated by a thin (<2 nm) LAO layer. Frictional drag has been investigated in $LaAlO_3/SrTiO_3$ (LAO/STO) heterostructures [61], where it is possible to create quasi-one-dimensional conducting channels in the STO layer through the technique of conductive atomic force microscopy (c-AFM) lithography [13]. In this technique, LAO/STO structures with LAO thickness near the metal-insulator transition [80] are positively charged with protons coming from adsorbed water [5], and the STO layer just beneath becomes conductive at room temperature and superconducting [68] at lower temperatures ($T < T_c \approx 300$ mK). Tang et al. have shown that strong frictional drag effects exist between LAO/STO nanowires, and that the interactions are non-Coulombic in nature [79] and significantly enhanced in the superconducting state [78].

Heterostructures formed between graphene and LAO/STO heterostructures provides

novel opportunities to investigate the electron-electron interaction within and between these two rich systems. To create the frictional drag geometry, rectangular areas of LAO/STO are created underneath the graphene using c-AFM lithography. In this case, the LAO layer serves as an ultrathin insulating barrier. Frictional drag measurements are performed between the two conducting layers; when the LAO/STO is the drive layer, frictional drag for both the longitudinal and transverse (Hall) configuration are measured. Experiments where graphene is the drive layer and LAO/STO is the drag layer are performed under conditions where the LAO/STO system is in the superconducting and non-superconducting states.

The device geometry is illustrated in Figure 62. The devices consist of a graphene layer and two-dimensional electron layer (2DEL) in the STO, near the LAO/STO interface. 2DEL is formed during c-AFM writing. Graphene is scanned with a doped silicon AFM tip in contact mode with a contact force of 15 $\sim$ 20 nN and scanning speed between 2 μm/s and 20 μm/s. A bias voltage $V_{\text{tip}} = 20$ V is used to create a conductive LAO/STO interface underneath the graphene [48]. The graphene and STO layers are separated by 8 unit cells (2.8 nm) of insulating LAO, which grown on STO by pulsed laser deposition (PLD). The graphene is grown by chemical vapor deposition (CVD) on oxygen-free electronic grade copper flattened with a diamond turning machine [24]. Graphene is transferred onto the LAO surface with the wet-transfer technique by using perfluoro polymer Hyflon AD 60 as a transferring layer. Graphene is patterned into Hall bars by standard photolithography. The photoresist (AZ4210) is spin-coated on the graphene film (4000 rpm for 30 sec, heating at 95°C for 2 min). Reactive ion etching (RIE) with O_2 plasma is used to etch the exposed area of the graphene sheet except for the graphene bar. Particles and contaminants on graphene from wet transfer and photolithography are brushed away using a contact-mode AFM scan sequence. The typical mobility of graphene Hall bars created in this fashion exceeds $10,000$ $\text{cm}^2\text{V}^{-1}\text{s}^{-1}$ at $T = 2$ K [48].

Figure 62 illustrate the c-AFM lithography technique used to create conductive areas in the STO. The conducting pattern sketched underneath the graphene is rectangular in shape with a width of 2 μm and length of 5 μm. This conducting region extends outside the graphene, and connects to one of the edge electrodes (Figure 62(a)). The graphene can subsequently gate the STO layer via a field effect [48], and there is a local shift in the

graphene CNP by 10^{12} cm^{-2} due to the c-AFM lithography writing process.

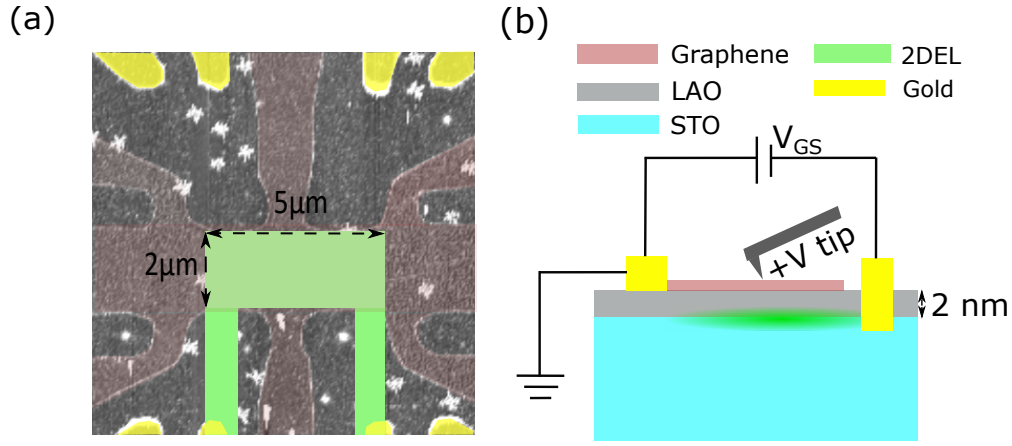

Figure 62: AFM image and schematic of the G/LAO/STO device (Device 7). (a) AFM image of the G/LAO/STO Device 7. graphene is patterned into a Hall bar structure on top of the LAO surface. The green shaded areas represent regions where the STO is locally patterned by c-AFM lithography into a conductive state. The conducting region makes electrical contact to Au electrodes that are etched through the interface. (b) Side-view schematic of the c-AFM lithography process. The conductivity of the LAO/STO interface is mediated by protons ("+" charges) that can pass through the graphene layer.

Coulomb drag measurements are performed by sourcing current in one layer and measuring a voltage in the other layer. Here we abbreviate the two layers as follows: graphene = "G", and STO = "S". We first describe experiments in which we source current $I_{\rm G}$ in the graphene and measure a voltage $V_{\rm S}$ in the STO. The source current $I_{\rm G}$ consists of a dc component $I_{\rm G}^0$ and an ac component $I_{\rm G}^\omega$ at angular frequency ω: $I_{\rm G} = I_{\rm G}^0 + I_{\rm G}^\omega \cos(\omega t)$. Sourcing current in this way generally yields a combined dc and ac voltage in the STO: $V_{\rm S} = V_{\rm G}^0 + V_{\rm S}^\omega \cos(\omega t)$. The (differential) drag resistance in STO may then be calculated as: $R_{\rm SG} \equiv V_{\rm SG}^\omega / I_{\rm S}^\omega$, where V_S^ω and $I_{\rm S}^\omega$ are separately measured using lock-in amplification. Here we explore the dependence of $R_{\rm SG}$ on a variety of parameters including $I_{\rm G}^0$, $V_{\rm GS}$, and plane-perpendicular magnetic field B. Except where noted otherwise, all measurements are performed below $T = 100$ mK. We similarly perform experiments in which current is sourced in

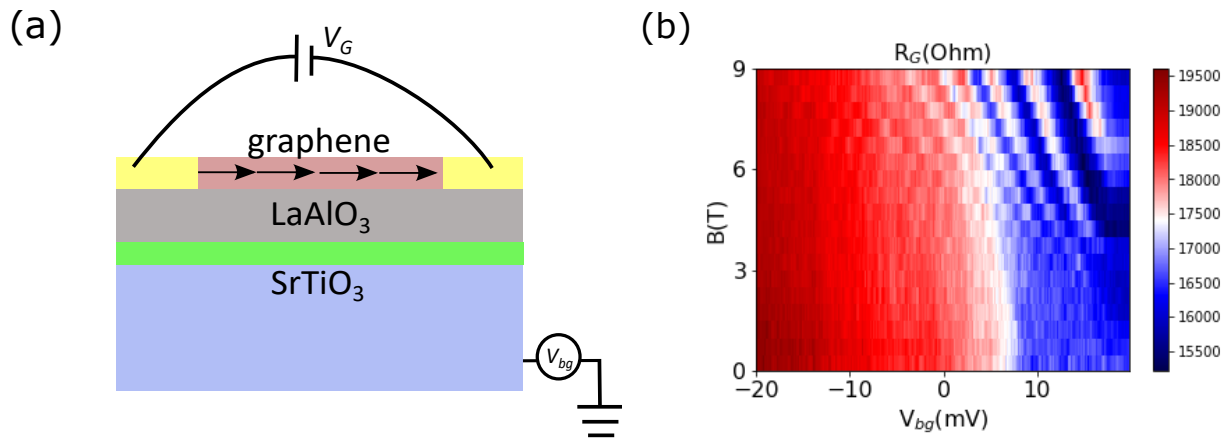

Figure 63: Graphene resistance as function of magnetic field and carrier density (Device 7). Landau levels are visible. Graphene is p-type doped.

the STO layer $I_{\rm S} = I_{\rm S}^0 + I_{\rm S}^\omega \cos(\omega t)$, yielding voltages in the graphene $V_{\rm GS} = V_{\rm GS}^0 + V_{\rm GS}^\omega \cos(\omega t)$, and define $R_{\rm GS} \equiv V_{\rm GS}^\omega / I_{\rm G}^\omega$, which corresponds to the (differential) drag resistance in graphene due to currents sourced in the STO layer. Meanwhile, $R_{\rm G} \equiv V_{\rm G}^\omega / I_{\rm G}^\omega$ corresponds to two terminal resistance in graphene and $R_{\rm S} \equiv V_S^\omega / I_S^\omega$ corresponds to two terminal resistance in STO. Both graphene and STO are connected to metallic electrodes and share a common ground. In order to ensure that the drag resistances are not influenced by electron tunneling between layers, leakage tests are performed before all measurements.

The impact of $V_{\rm bg}$ on the doping level of graphene is shown in Figure 63. Due to the shielding effect of LAO/STO, the carriers in graphene cannot be tuned to n-type. In the p-type region, the Landau levels are visible. The density of the graphene layer can be tuned with the interlayer gate-voltage ($V_{\rm GS}$) utilizing LAO as the dielectric layer.

Figure 64 is the typical leakage test for Device 7 and 8. $V_{\rm GS}$ is applied between graphene and STO, the leakage current is measured between graphene and STO. To ensure the drag resistances are not influenced by electron tunneling between the two nanowires, all measurements are performed well below the measured inter-wire breakdown voltage of each device.

The physics of the Coulomb drag can be well explained if both layers are in the Fermi liquid state [56]. The current in the passive layer is created by exciting electron-hole pairs in

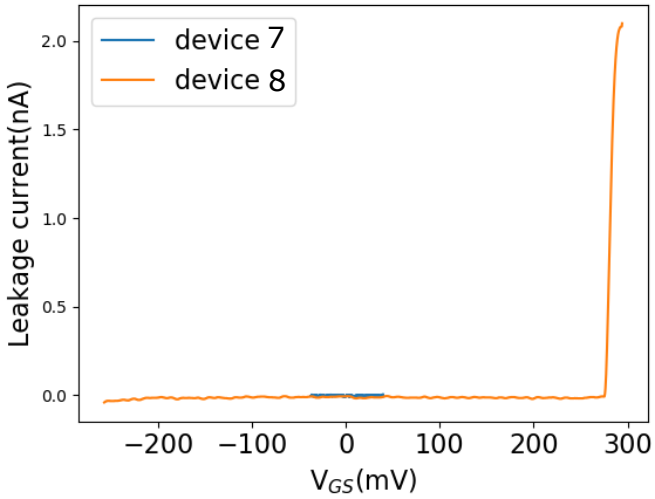

Figure 64: Leakage test across graphene and STO (Device 7 and Device 8). All measurements are performed well below the measured inter-wire breakdown voltage of each device.

a state characterized by finite momentum. The momentum comes from the carriers in driving current. The momentum transfer is due to the inter-layer coulomb interaction. Therefore the drag resistance follows from the usual quadratic temperature dependence $\rho_{\mathrm{D}} = T^2$. This approximate form of the interlayer Coulomb interaction is valid only in the "ballistic" regime, where the dominant interlayer relaxation processes are characterized by relatively large momentum transfers. A smaller momentum transfer will lead to a plasmon mode. At higher temperature $T > T_{\mathrm{C}}$, coulomb drag is dominated by the plasmon, drag resistance will decrease after T_C. In Figure 65, the drag resistance diverges below 20 K. From 20 K to 50 K, the drag resistance increase with temperature. Beyond 50 K, the drag resistance starts dropping down to zero. This temperature dependence is inconsistent with either coulombic interfaction or other non-coulombic interactions, such as virtual phonon exchange [34, 81, 82].

Figure 66 shows typical drag results for G/LAO/STO device (Device 7). Both drag resistance in STO and drag resistance in graphene are measured for this device as a function of the applied bias V_{GS} at low magnetic fields ($|B| < 0.1$ T). V_{GS} is varied between 0 mV to 30 mV. To estimate the change of carrier density in graphene, we employ a capacitive model,

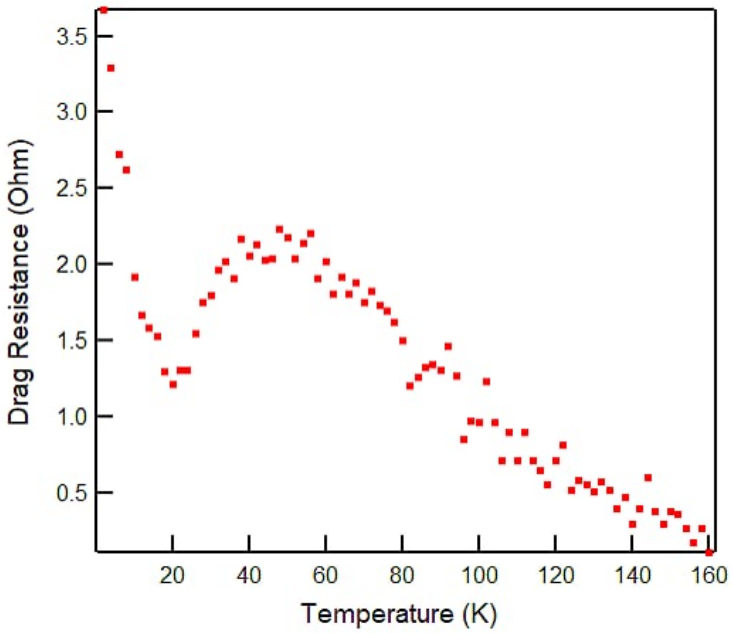

Figure 65: Drag resistance in STO as a function of temperature (Device 7). The temperature dependence is inconsistent with the usual quadratic temperature dependence.

with an estimated capacitance between graphene and LAO layer C = 4.5 μF/cm^2. With this model, the change of carrier density in graphene can be calculated as $\Delta n = C \cdot V_{\mathrm{GS}}/e$. For measuring R_{SG}, current is sourced in the graphene at frequency $\omega/2\pi$ = 9.468 Hz and I_{G}^{ω} = 28 nA(with V_{GS} = 0 mV).

Figure 66 shows typical drag results for G/LAO/STO device (Device 7). Both drag resistance in STO and graphene are measured for this device as a function of the applied bias V_{GS} at low magnetic fields ($|B| < 0.1$ T). V_{GS} is varied between 0 mV to 30 mV. For measuring R_{SG}, current is sourced in the graphene at frequency $\omega/2\pi$ = 9.468 Hz and I_{G}^{ω} = 28 nA (with $\mathrm{V_{GS}}$ = 0 mV). The measured drag resistance is in phase with the drive current, with negligible out-of-phase response. The drag resistance R_{SG} exhibits two main features: (1) a stripe-like modulation as the carrier density Δn is changing, and (2) a large drag resistance near zero magnetic field. The strip-like feature is also manifested in graphene resistance as a function of B and Δn in Figure 66 (c), which can be attribute to the universal

conductance fluctuations (UCF) effect [1]. At low temperatures, the quantum transport of electrons becomes coherent and leads to quantum interference. The UCF take place when a coherent electron wave scatters while traversing a disordered conductor. As the same electrons are responsible for Coulomb drag, it is natural to expect that the drag resistivity also exhibits mesoscopic fluctuations [65, 55]. The drag fluctuations change sign randomly but reproducibly between positive and negative. The large drag resistance in STO is correlated with the superconducting state in the STO, decaying when the upper critical magnetic field is reached. Typically $\mu_0 H_{\rm C} \sim 0.3$ T [18]; however, in this instance the critical field is strongly suppressed, around 50 Oe . Drag resistance $R_{\rm SG}$ is also studied in graphene while current is running in STO. Drive current $I_{\rm S} = I_{\rm S}^{\omega} \cos \omega t$ with $\omega/(2\ \pi) = 9.468$ Hz and $I_{\rm G}^{\omega} = 18$ nA is applied in STO. However, the drag in graphene isn't enhanced in the STO superconducting region.

The drag resistance $\rm R_{SG}$ in STO as a function of DC current in graphene is also studied. As shown in Figure 67, Drive current $I_{\rm G} = I_{\rm G}^{0} + I_{\rm G}^{\omega} \cos \omega t (I_G^{\omega} = 28$ nA) is running through graphene with $I_{\rm G}^{0}$ varied from -650 nA to 650 nA. Giant drag resistance is observed at zero magnetic field (Figure 67(b)). This corresponds well with the superconducting region of STO in Figure 66(b). In Figure 66(f), STO is conducting when $|B| < 0.005$ T. STO drag resistance is only enhanced within this magnetic field region.

Drag resistance is not only enhanced in the superconducting region, but also in the high magnetic field (9 T). In Figure 68(a), drag resistance in STO as a function of driving current and magnetic field is plotted (Device 8). The drag signal in a high magnetic field is larger than in a zero magnetic field. Also, unlike drag resistance in Figure 68(b), the drag resistance is anti-symmetric for driving current, which is non-intuitive. One explanation is that this drag resistance contains Hall component, which is discussed later.

Drag resistance in graphene is investigated in a lager magnetic field range for a second device (Device 9). Drive current $I_{\rm S} = I_{\rm S}^{\omega} \cos \omega$ with $\omega/2\pi = 9.468$ Hz and $I_{\rm S}^{\omega} = 5$ nA is running through STO. In small magnetic field (Figure 69(b)), drag resistance in Device 9 is also showing the giant fluctuation, quite consistent with Device 7 (Figure 66(e)). We observe magneto-drag resistance oscillations that are tuned by carrier density and magnetic field. The drag signal is strong in both low magnetic field and high magnetic field. In the

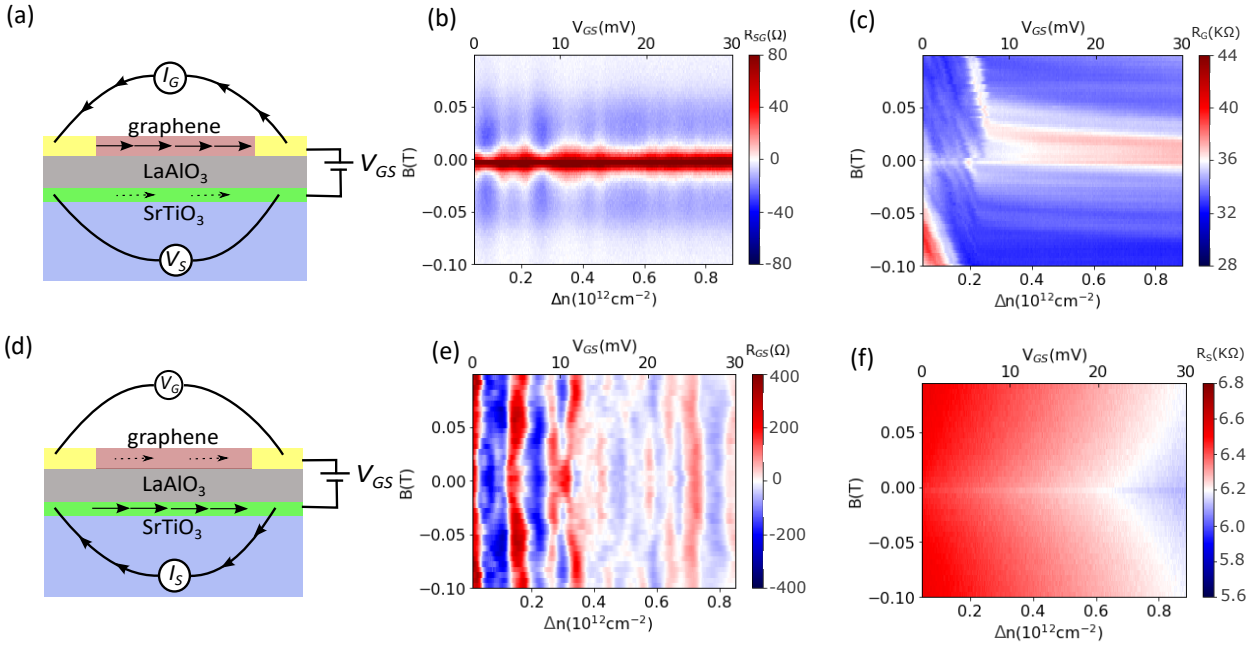

Figure 66: Drag resistance measured in Device 7. (a) Schematic diagram for measuring drag signal in STO. Drive current is running through graphene. A bias voltage $V_{\rm GS}$ is maintained between graphene and STO. graphene carrier density will change as $R_{\rm GS}$ varies. (b)The drag resistance in STO measured at T=50 mK versus the magnetic field. The frictional drag resistance is enhanced in a low magnetic field. (c) Two terminal measurements of graphene resistance. (d) The schematic diagram for measuring drag resistance in graphene. Drive current $I_{\rm S} = I_{\rm S}^{\omega} \cos \omega t$ with $I_{\rm S}^{\omega}$ around 18 nA. (e) Drag resistance in graphene. Drive current is running through STO. (f) Two terminal measurements of STO resistance.

intermedia magnetic field region, the drag signal decreases to zero. In the high magnetic field region (3 T $\sim$ 5 T), the magnitude of the drag fluctuations as a function of Δn is roughly the same as that as a function of B. Conductance of graphene calculated using the kwant package[35] is shown in Figure 69(d). The numerical simulation result shows higher conductance of graphene in low and high magnetic field, which reproduces the measurement of drag resistance in Figure 69(c). Given the fact that drag resistance is usually proportional to drive current, we can say the magneto drag resistance in STO is basically following the

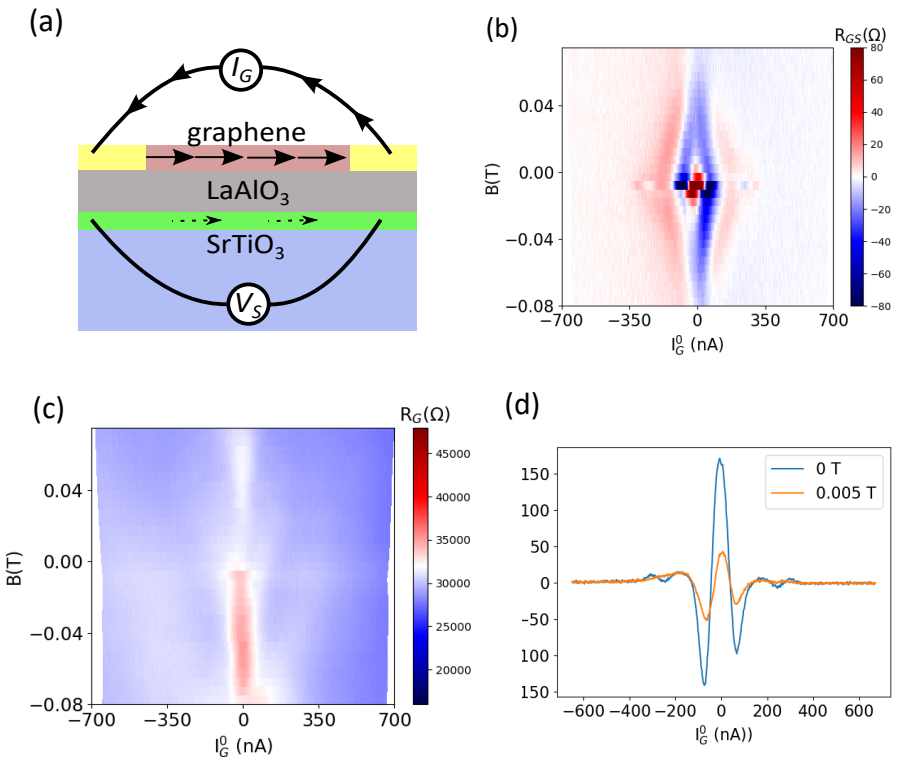

Figure 67: Drag resistance in STO affected by driving current (Device 7). (a) Schematic diagram for measuring drag resistance in STO. (b) Drag resistance R_{GS} in STO as a function drive current under magnetic field. (c) Corresponding graphene resistance while drag resistance is measured (d) line cut from (b) under zero magnetic field and 0.005T. Drag resistance is greatly enhanced at zero field.

tendency of conductance in graphene.

Meanwhile, the STO resistance R_{S} shown in Figure 66(a). The dark blue region at the zero magnetic field in (a) indicates the superconductivity of STO. Unlike drag resistance in STO, drag resistance in graphene is not enhanced in STO superconducting region. To our knowledge, the drag signal in graphene at the small magnetic field is not correlated with STO superconductivity. The drag features in graphene remain almost the same when we increase the DC drive current to destroy the superconductivity in STO (see figure 70).

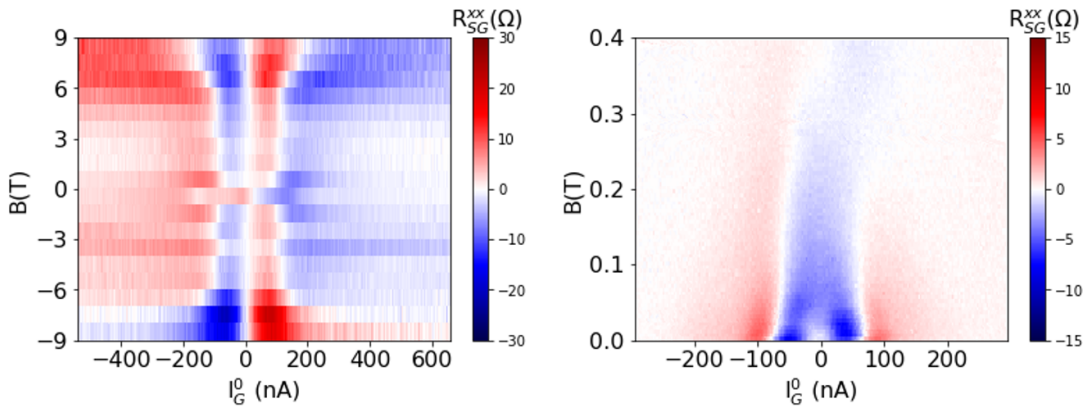

Figure 68: Drag resistance in high and low magnetic field (Device 8). (a) Schematic diagram for measuring drag resistance in STO. (b) Drag resistance R_{GS} in STO as a function drive current under magnetic field. (c) line cut from (h) under zero magnetic field and 0.005 T. Drag resistance is greatly enhanced at zero field.

In Figure 70, drag resistance in graphene is shown when the drive current is in the superconducting and non-superconducting region. The set up for this experiment is the same as in Figure 66(d). Drive current $I_{\mathrm{S}} = I^0_{\mathrm{G}} + I^{\omega}_{\mathrm{S}} \cos \omega t$ with $\omega/2\pi = 9.468$ Hz and $I^{\omega}_{\mathrm{S}} = 16$ nA is running through STO. The only difference is the DC component of sourcing current in STO. Here in Figure 70, the drive current I^0_{G} is 140 nA. The superconductivity still exists, but weaker. In Figure 70(d), the I^0_{G} increases to 350 nA, completely destroy the conductivity in STO. The drag resistances in Figure 70 (a) and (b) are almost the same, which demonstrates the superconductivity does not determine the drag feature in graphene.

In Device 9, we observed similar fluctuation features in graphene resistance (Figure 71). More interestingly, this device has more features. Near zero magnetic field, the drag resistance shows a triangular shape pattern. Figure 71(c) is the zoom in of Figure 71(b), (d) is the corresponding drive current in STO.

We investigate the longitudinal and transverse drag resistance in graphene using an LAO/STO pattern shown in Figure 72. Drive current $I_{\mathrm{S}} = I^{\omega}_{\mathrm{S}} \cos \omega t$ with $\omega/2\pi = 9.468$ Hz and $I^{\omega}_{\mathrm{S}} = 16$ nA is applied in STO. The longitudinal drag resistance exhibits more

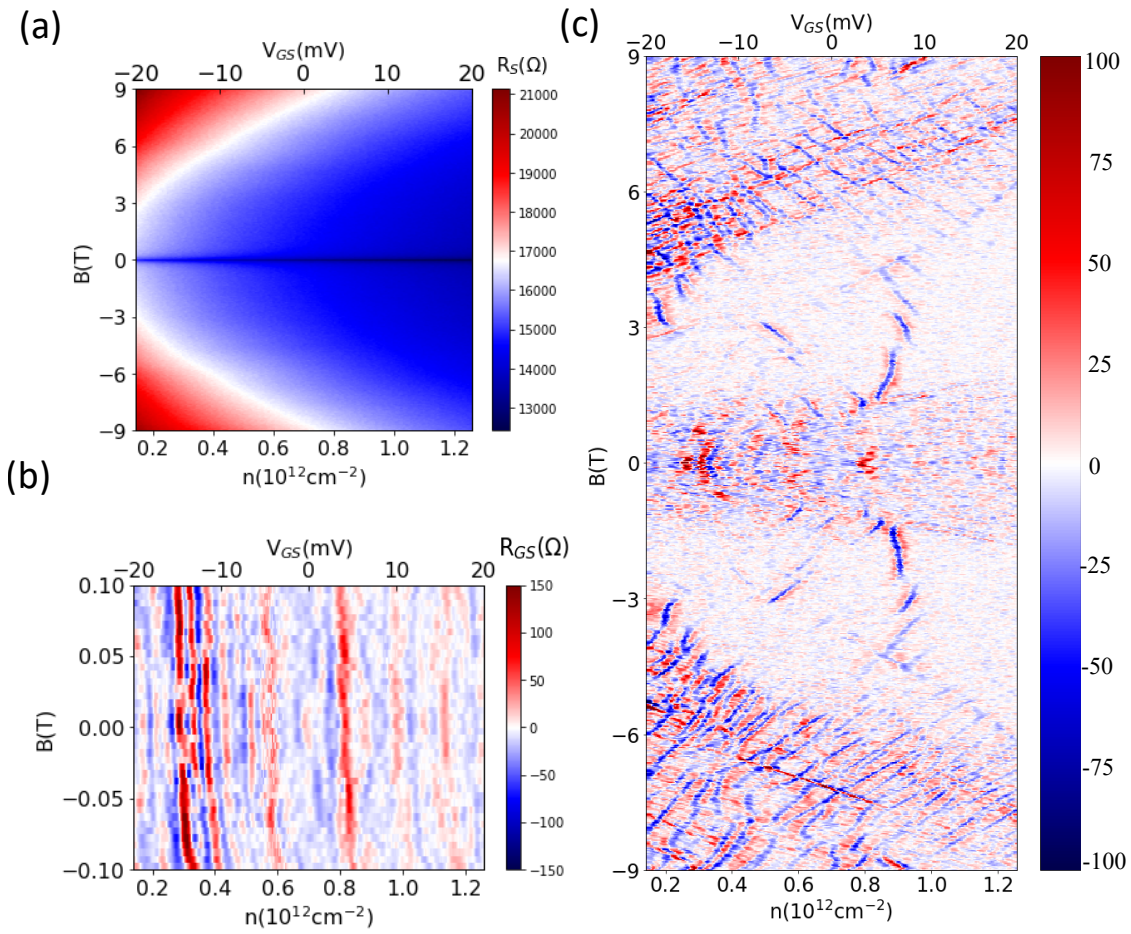

Figure 69: Drag resistance in graphene under a larger magnetic field range from Device 9. (a) STO resistance R_{S}. (b) Drag resistance R_{GS} is measured in graphene from $B = -0.1$ T to 0.1 T, which is quite consistent with Device 9. (c) Drag resistance R_{GS} is measured in graphene from $B = -9$ T to 9 T. (d) Conductance of graphene is calculated by a tight-binding quantum transport calculation(Kwant) based on the designed geometry of the measured device.

obvious fluctuation from –2 T to 2 T. In the high magnetic field region, the longitudinal drag resistance is almost zero. However, the transverse drag resistance shows giant fluctuations in the high magnetic field region. In the small magnetic field, electrons in the drive layer have a larger cyclotron radius such that momentum along the current direction will be transferred to the drag layer. On the other hand, in the high magnetic field, electrons in the drag layer

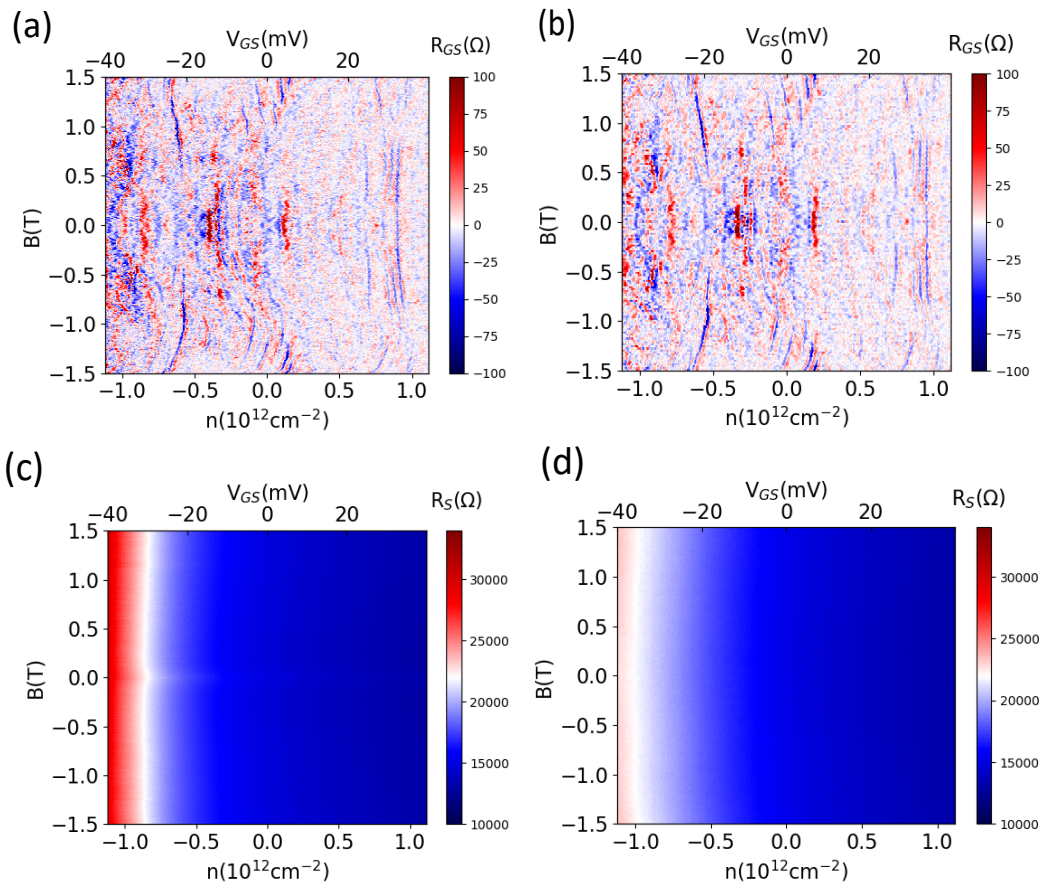

Figure 70: Drag resistance is measured in graphene (Device 9) at $T = 50$ mk from $B = -1.5$ mk to 1.5 T when LAO/STO is in superconducting state shown in (C). (b) Drag resistance is measured in graphene at 50 mK from -1.5 T to 1.5 T when LAO/STO is no longer in superconducting state shown in (d). (C) AC current measured in graphene when $I_{\mathrm{G}}^{0} = 140$ nA is applied to one of the STO lead. (d) AC current measured in graphene when a small $I_{\mathrm{G}}^{0} = 350$ nA is applied.

have a smaller cyclotron radius and move perpendicular to the current direction. Momentum perpendicular to the current direction is then transferred to electrons in the drag layer. In such a way, drag resistance is more prominent in Hall direction under a high field.

Figure 73 shows the nonlinearity of drag in STO from Device 12. The drive current $I_{\mathrm{G}} = I_{\mathrm{G}}^{0} + I_{\mathrm{G}}^{\omega} \cos \omega t (I_{\mathrm{G}}^{\omega} = 60$ nA) is running through graphene. The longitudinal drag $R_{\mathrm{SG}}^{\mathrm{xx}}$

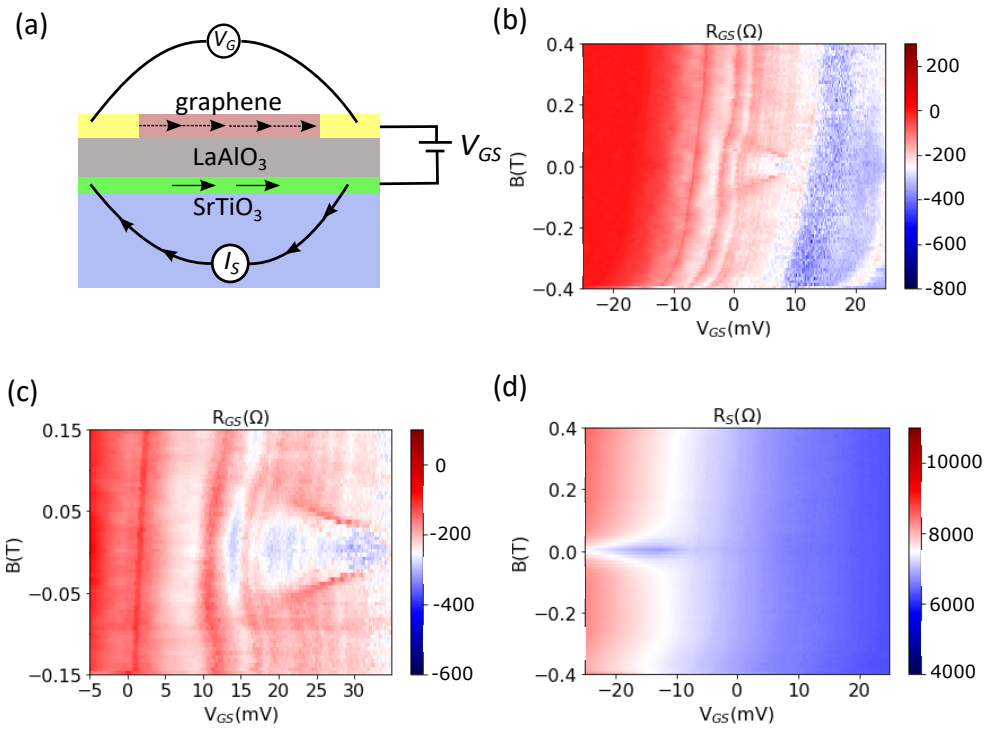

Figure 71: Drag resistance in graphene under larger magnetic field range from Device 10. (a) Schematic of the graphene drag resistance measurement. (b) Drag resistance R_{GS} is measured in graphene from B = -0.4 T to 0.4 T, which is quite consistent with Device 7, except the triangle feature. (c) Zoom-in of (b). (d) The conductance of STO is measured while performing drag in graphene. The bright part around a zero magnetic field corresponds to the superconductivity of STO.

is mainly symmetric under magnetic field with small portion of antisymmetric part. The antisymmetric part might come from the transverse drag signal. Meanwhile, the transverse drag $R_{\mathrm{SG}}^{\mathrm{xx}}$ is mainly asymmetric under magnetic field.

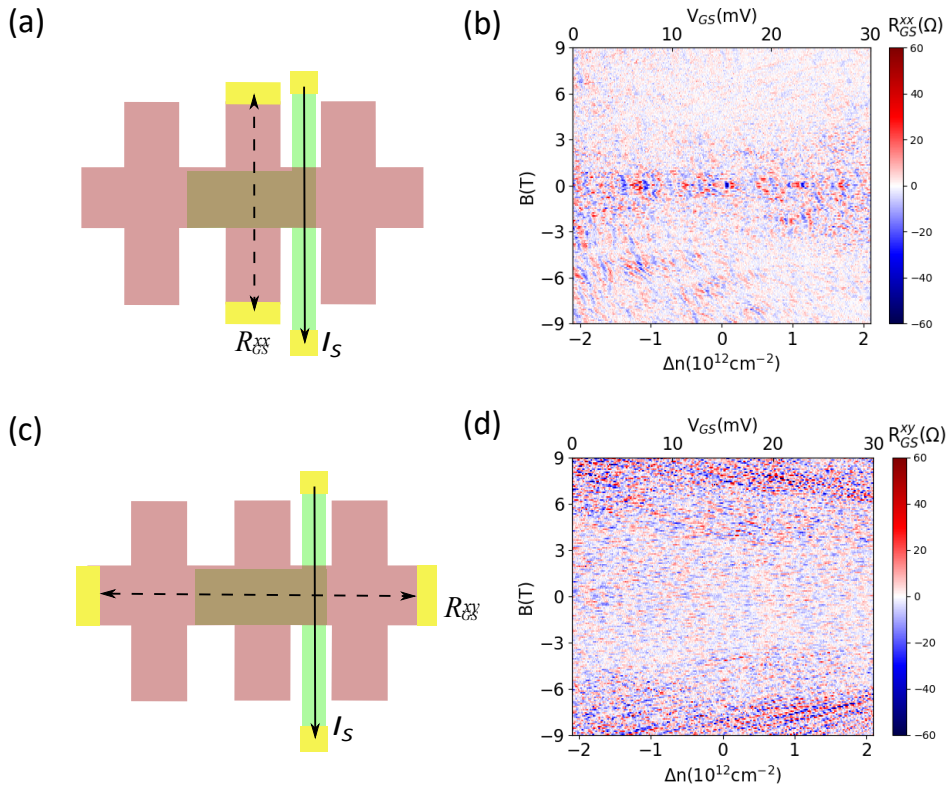

Figure 72: Graphene drag resistance R_{GS} in longitudinal direction and Hall direction from Device 11 at $T = 2$ K. (a) is the configuration for longitudinal drag. (b) Graphene drag resistance measured in Longitudinal direction. (c) is the configuration for transverse drag. (d) Graphene drag resistance measured in transverse direction.

3.5.3 Tight-binding model and Kwant simulation

To better understand the doped graphene region's transport properties, we employ Kwant, an open-source python package for quantum simulation, to simulate the system [35]. For a few atoms and electrons, we can solve the many-electron wavefunction accurately. When the system contains up to a few hundred of a few thousand atoms, we can use density functional theory(DFT) techniques to solve ground state density without explicitly solving the wavefunction. For an even larger system with atoms more than 10,000, we adopt the tight-binding model. In an insulator or semiconductor, we assume the states in the

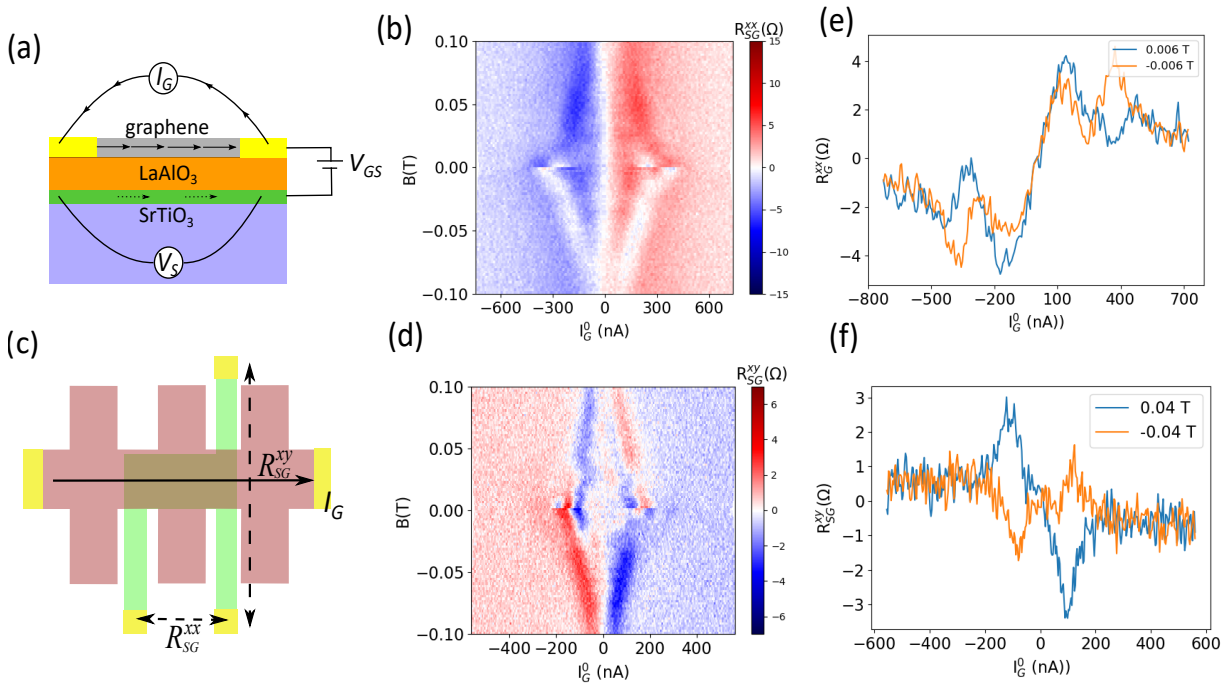

Figure 73: Drag signal in STO as a function of the drive current (Device 12). (a) Schematic diagram for measuring drag signal in STO. Drive current $I_{\rm G} = I^0_{\rm G} + I^\omega_{\rm G}\cos\omega t$ is running through graphene. (b) Schematic diagram for measuring drag signal $R^{\rm xx}_{\rm SG}$ and $R^{\rm xy}_{\rm SG}$ in STO. (c) Drag resistance $R^{\rm xx}_{\rm SG}$ in STO as a function of DC drive current $I^0_{\rm G}$. (d) Drag resistance $R^{\rm xy}_{\rm SG}$ in STO as a function of DC drive current $I^0_{\rm G}$. (e) Line cuts from (c) at $B = 0.006$ T and -0.006 T. The drag signal is mainly symmetric under magnetic field. (f) Line cuts from (d) at $B = 0.04$ T and -0.04 T. The drag signal is mainly asymmetric under magnetic field.

crystal are combinations of wavefunctions of isolated atoms. The wavefunction of the lattice as a form of Bloch wave function expanded as a linear combination of isolated atoms,

$$\Psi_{k,j}(r) = \frac{1}{\sqrt{N}} \sum_R e^{ik\cdot r} \Phi(j) \tag{3.7}$$

Here N is the number of unit cells, $\mathbf{R}$ is the real-space lattice vector. $\Phi_j(\mathbf{R}, \mathbf{r})$ is constructed from atomic orbitals of all electrons in the unit cell. α, β, s stands for different sublattices, different orbitals and different spins. $\Phi_j(\mathbf{R}, \mathbf{r})$ is composed of atomic orbitals of

all electrons in the unit cell with all these different degrees of freedom,

$$\Phi_j(r) = \sum_{\alpha,\beta,s} \phi(r - r_\alpha), \tag{3.8}$$

here $\mathbf{r}_\alpha$ is offset of atom from sublattice α. $\phi_{\beta,s}$ is the wave function of each individual atomic orbital. Schrödinger equation is written as,

$$H\Psi_k(r) = E\Psi_k(r), \tag{3.9}$$

with wavefunction $\Psi_k(\mathbf{r})$ written as a combination of on-site Bloch wave functions,

$$\Psi_k(r) = \sum_j c_{k,j}\Psi_{k,j}(r) \tag{3.10}$$

Considering the orthogonality of the Bloch functions, the Schrödinger equation can be written as,

$$\sum_{i,j} c^*_{k,i}c_{k,j}[\left\langle \Psi^*_{k,i}(\mathbf{r})\right| H \left|\Psi^*_{k,i}(\mathbf{r})\right\rangle] - E_k \left\langle \Psi^*_{k,i}(\mathbf{r})\right| H \left|\Psi^*_{k,i}(\mathbf{r})\right\rangle = 0. \tag{3.11}$$

the transfer matrix element is,

$$H_{i,j}(k) = \frac{1}{N}\sum_{R,R'} e^{ij}(R - R^{'}) \int dr\phi^*_i(r - R^{'})H\phi_j(r - R), \tag{3.12}$$

the overlap matrix element is,

$$S_{i,j}(k) = \frac{1}{N}\sum_{R,R'} e^{ij}(R - R^{'}) \int dr\phi^*_i(r - R^{'})H\phi_j(r - R), \tag{3.13}$$

the energy spectrum for fixed $\mathbf{k}$ is

$$E(k) = \frac{\sum_{i,j} H_{i,j}(k)c^*_{k,i}c_{k,j}}{\sum_{i,j} E_{i,j}(k)c^*_{k,i}c_{k,j}} \tag{3.14}$$

Take a partial derivative, the local minimum of the energy is,

$$\sum_j [H_{i,j}(k) - E_k S_{i,j}(k)]c_{k,j} = 0 \tag{3.15}$$

in the case of graphene there is only one electron per p_z orbital for each carbon atom

$$\begin{pmatrix} H_{AA} & H_{AB} \\ H_{BA} & H_{BB} \end{pmatrix} - E_K \begin{pmatrix} S_{AA} & S_{AB} \\ S_{BA} & S_{BB} \end{pmatrix} = 0 \tag{3.16}$$

If we assume only the nearest-neighbour hopping term is non-zero, we can calculate the elements as follows,

$$H_{AA} = \frac{1}{N} \sum_{i=1}^{N} \langle \Psi_A(\mathbf{r} - \mathbf{R}_{A,i}) | \, H \, | \Psi_A(\mathbf{r} - \mathbf{R}_{A,i}) \rangle \tag{3.17}$$

The integral is the same for each atom in sublattice A or B represents the energy of the p_z orbital, which we mark it as ϵ_{2p}. H_{AA} can be rewritten as,

$$H_{AA} = \frac{1}{N} \sum_{i=1}^{N} \epsilon_{2p} = \epsilon_{2p} = H_{BB} \tag{3.18}$$

Overlap matrix element S_{AA} is calculated as,

$$S_{AA} = \frac{1}{N} \sum_{i=1}^{N} \langle \Psi_A(\mathbf{r} - \mathbf{R}_{A,i}) \Psi_A(\mathbf{r} - \mathbf{R}_{A,i}) \rangle = \frac{1}{N} \sum_{i=1}^{N} 1 = 1 \tag{3.19}$$

The off diagonal matrix elements are,

$$H_{AB} = \frac{1}{N} \sum_{j=1}^{N} \sum_{i=1}^{3} e^{i\mathbf{k}(\mathbf{R}_{B,i} - \mathbf{R}A,j)} \langle \phi_A(\mathbf{r} - \mathbf{R}_{A,j}) | \, H \, | \phi_B(\mathbf{r} - \mathbf{R}_{B,i}) \rangle \tag{3.20}$$

From symmetry we know $\langle \phi_A | \, H \, | \phi_B \rangle$ is independent of indices and we mark it to be t. The off-diagonal term is written as,

$$H_{AB} = \frac{1}{N} \sum_{j=1}^{N} \sum_{i=1}^{3} e^{i\mathbf{k}(\mathbf{R}_{B,i} - \mathbf{R}A,j)} t = \frac{1}{N} \sum_{j=1}^{N} \sum_{i=1}^{3} e^{i\mathbf{k}\delta_i} t = t f(\mathbf{k}) \tag{3.21}$$

δ_i is vector between sublattice A to nearest B. $f($**k** is given by,

$$f(\mathbf{k}) = e^{ik_y a/\sqrt{3}} + 2e^{-ik_y a/2\sqrt{3}} \cos(k_x a/2) \tag{3.22}$$

In the same way, the off-diagonal overlap matrix elements are calculated as,

$$S_{AB} = \frac{1}{N} \sum_{i=1}^{N} e^{i\mathbf{k}(\mathbf{R}_{B,i} - R_{A,j})} \langle \phi_A(\mathbf{r} - \mathbf{R}_{A,i}) \phi_A(\mathbf{r} - \mathbf{R}_{B,i}) \rangle = s f(\mathbf{k}) \tag{3.23}$$

The dispersion relation for graphene is

$$E(\mathbf{k}) = \pm\sqrt{3 + 2cos(k_x a) + 4cos(k_x a/2cos(\sqrt{3}k_y a/2)} \tag{3.24}$$

Kwant is suitable for both finite and infinite system consist of a finite scattering region. The semi-infinite periodic electrodes act as waveguides leading plane wave into and out of the scattering region. The Hamiltonian of the system is,

$$\hat{H} = \sum_{i,j} H_{i,j} c_i^+ c_j, \tag{3.25}$$

Where $c_i^+ c_j$ are the fermionic creation(destruction) operators. Kwant focuses on the wavefunction approach due to its simpler structure compare to non-equilibrium Green's functions. Here we consider a case with one lead. Several leads can be treated as single lead with disjoint sections. In this system, the sites are ordered according to the reverse distance to the scattering region. The Hamiltonian can also be written as,

$$H = \begin{pmatrix} \ddots & V_L & & \\ V_L^+ & H_L & V_L & \\ & V_L^+ & H_L & V_{LS} \\ & & V_L^+ & H_S \end{pmatrix} \tag{3.26}$$

Where H_s is the Hamiltonian of the scattering region, H_L is the lead Hamiltonian. V_L is the Hamiltonian connecting one lead site to the next lead site. $V_L S$ is the Hamiltonian from the scattering region to lead.

The wavefunction of an infinite system is defined as $(..., \phi^L(2), \phi^L(1), \phi^S)$, where ϕ^S is the wavefunction of the scattering region, ϕ^L is the wavefunction of the lead. Due to the transitional invariance of the leads, the wave function of them is a superposition of plane waves. The eigenstates of the translation operator in the lead can be written as,

$$\phi_n(j) = (\lambda_n)^j \chi_n, \tag{3.27}$$

They obey the Schrödiner equation,

$$(H_L + V_L \lambda_n^{-1} + V_L^\dagger \lambda)\chi_n = E\chi_n, \tag{3.28}$$

Where χ_n is the nth eigenvector, λ_n is the nth eigenvalue. The propagating modes are with $\lambda_n = e^{ik_n}$. They can be normalized according to the expectation value of the particle current, such that,

$$\langle I \rangle \equiv 2Im \langle \phi_n(j)|V_L|\phi_n(j-1)\rangle = \pm 1. \tag{3.29}$$

The modes are sorted into incoming ones, outgoing ones and evanescent ones. The scattering states in the leads can be written as,

$$\psi_n(i) = \psi_n^{in}(i) + \sum_{mn} \phi_m^{out}(i) + \sum_p \tilde{S_{pn}} \phi_p^{ev}(i), \tag{3.30}$$

The scattering wave function inside the system is,

$$\psi_n(0) = \phi_n^s \tag{3.31}$$

The main output of kwant is the scattering matrix S_{nm} and the wave function inside the scattering region ϕ_n^S. They can be calculated by solving equation (2.32), with H given by (2.33).

The differential conductance $G_{ab} = dI_a/dV_b$ is given by the Landauer formula,

$$G_{ab} = \frac{e^2}{h} \sum_{n\in a, m\in b} |S_{nm}|^2. \tag{3.32}$$

The local density of states or current density can be obtained,

$$\left\langle c_i^\dagger c_j \right\rangle = \int \frac{dE}{2\pi} \sum_n f_n(E) \phi_n^s [\phi_n^s(i)]^*, \tag{3.33}$$

here $f_n(E) = 1/[1 + e^{(E-\mu_n)/kT_B}]$ is the Fermi distribution of the nth lead.

3.5.4 Kwant workflow

To define a tight-binding model, it is natural to consider it as a mapping with vertices and edges, which is analogous to the Hamiltonian for the sites and hoppings. This mapping is represented by a Builder object. It is implemented as a hash table (Python dictionary). In such a way, we can efficiently add or remove sites and hoppings. Sites are classified by type of atom or the sublattices they belong to. In Kwant, a site is defined to be a combination of a family and a tag. Family is the class of the site, tag identifies a unique site within this family. For a real crystal system, many sites belong to the same family. In this case, we can define a site family to represent the sublattices and use tuples to tag different sites within a family. The site tuples can be integer coefficients $(n_1, ..., n_d)$ on the basis of the Bravais lattice vectors $\mathbf{a}_1, ..., \mathbf{a}_d$, with d the dimensionality of the lattice.

To better illustrate how to use Kwant, a workflow is shown in Figure 76. Despite the various type of systems, the procedures can be fit into this framework. The first step is to include the Kwant package. As described before, we need to create the builder object. Also, we need to define the lattices. For example, define the honeycomb lattice for graphene. We continue by creating a scattering region. Kwant allows us to specifies the shape of the scattering region. We proceed to add sites to the scattering region and set the onsite potential. A potential well can be added by modifying the onsite potential of a certain region. We then set the hopping term between nearest neighbors. To complete the initializing, we need to make leads. The procedures for creating leads are very similar to making a scattering region. The only difference is that the symmetry will be automatically maintained. The last step for making a system is to finalize the system.

Now Kwant solver is used to obtaining physical quantities. Real physical quantities such as energy and magnetic field can be passed to the system by an initial dictionary. The function kwant. Smatrix calculates the scattering matrix of the system at given energy and magnetic field. This scattering matrix is then used to calculate the transmission from one lead to another. The function kwant.ldos returns the local density of states in the scattering region.

We employ the Kwant software to calculate the conductance of a graphene device with

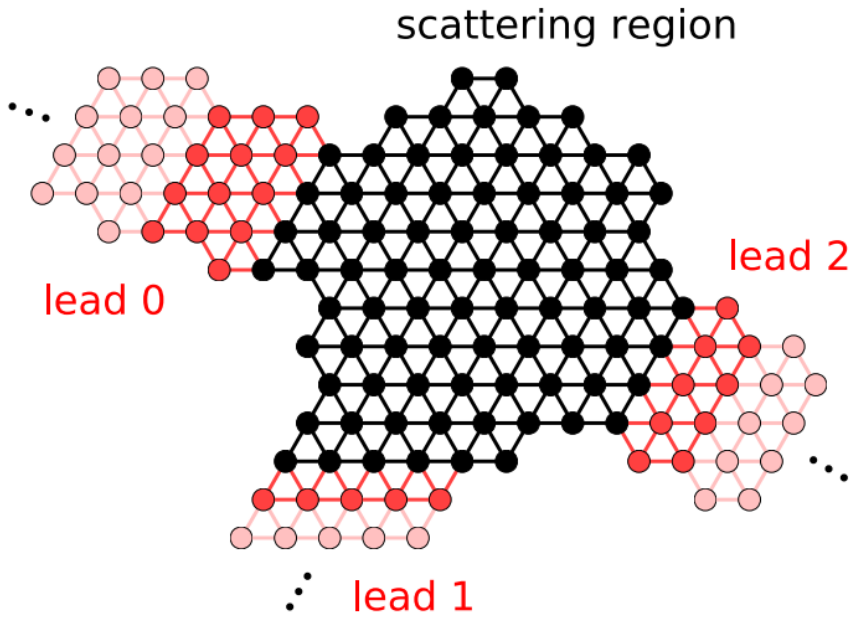

Figure 74: A structure example of the tight-binding model build by kwant. Black dots denote for the scattering region while red dots denote for the semi-infinite region. The line connections between dots correspond to the non-zero hopping from one site to the other. In this device, all the sites in the scattering region belong to the same site family. Adapted from [35].

the dimensions L x H. L is 100 a and H is 20 a, where a $\approx$ 1.42 Å is the length of the carbon-carbon bond. Two graphene leads are attached to graphene to obtain the conductance of graphene. Our device is depicted in Figure 77(b). The honeycomb lattice has two basis atoms. A potential well is added to graphene in the center, as shown in (b). The height of the well is 0.3 eV. In Figure 78(a), the simulated conductance recorded as a function of Fermi level (gate voltage) and magnetic field. The simulated conductance at a low magnetic and high magnetic field is qualitatively comparable to the measurements shown in Figure 69. Wave function density is shown in from (c) to (e), with magnetic field varied from 0 T to 2 T. At zero magnetic field, the wavefunction is distributed in the whole device while it vanishes at 1 T. As magnetic field increases to 2 T, the wavefunction is more localized at

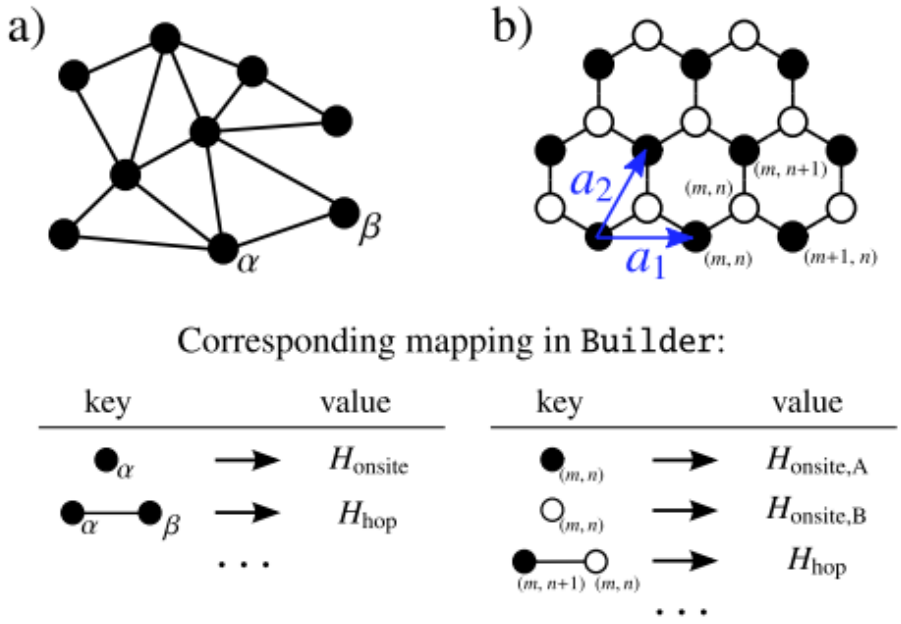

Figure 75: Examples of tight-binding systems and a pictorial representation of the corresponding mapping in Kwant. (a) Example of an irregular tight-binding lattice with a single site family (filled circles) and site tags α,.. β. (b) Example of a regular honeycomb lattice. The two sublattices A and B are mapped to two site families (filled and open circles), and site tags are given as tuples of integers (lattice indices). Adapted from [35].

the edge of the device. These density plots in graphene also give us an insight into how edge states evolve under the magnetic field and affect the drag signal in STO. Typically, the drag signal is proportional to driving current. This can explain why the drag signal in Figure 78 is stronger in the high and low magnetic field than the intermediate magnetic field.

In this section, we have shown the essential features of our frictional drag results. We fabricated G/LAO/STO heterostructures and measured the drag signal in both graphene and STO layers. Both R_{GS} and R_{SG} can be tuned as a function of carrier density. Numerical simulation shows the localization of edge states in graphene under a magnetic field, which corresponds to the dismiss of drag signals in STO in the intermedia magnetic field. Drag resistance in STO R_{SG} is greatly enhanced in the superconducting region of STO. The drag

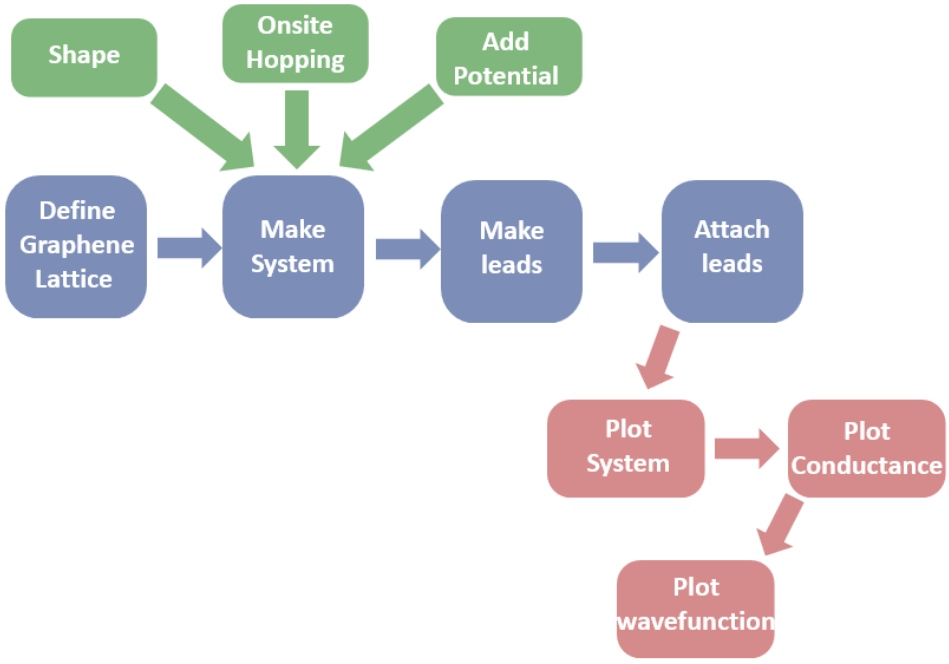

Figure 76: Kwant workflow. The procedure includes making a system, attaching leads and plotting the wave function.

resistance R_{SG} as a function of drive current in graphene also exhibits superconducting features that originate from STO. Moreover, the magneto drag resistance in graphene has different behavior in a longitudinal direction and Hall direction. The longitudinal drag resistance shows more features from –2 T to 2 T, while the Hall drag resistance has more prominent features in a high magnetic field. Hybrid G/LAO/STO offers a novel platform for studying coulomb drag between normal conductor and superconductor. The sketching process on STO allows performing different geometries of frictional drag. Our system is flexible, making it important to study carriers interaction.

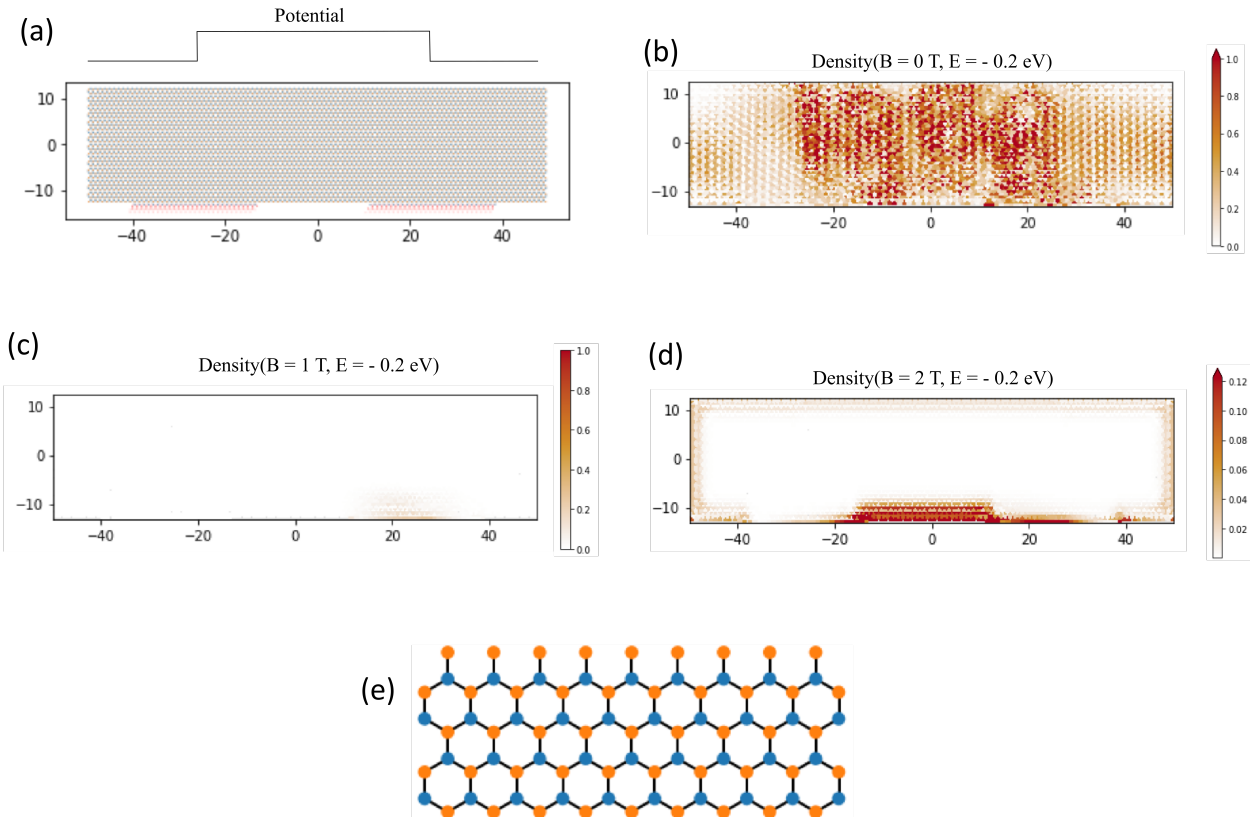

Figure 77: Kwant simulation of graphene (Device 9). (a) The conductivity of graphene as evaluated numerically using the Kwant package. (b) Graphene device with two leads attached. Inserted is a zoom in of graphene lattice. (c), (d), (d) Wave function density plot under $B = 0$ T, 1 T, 2 T.

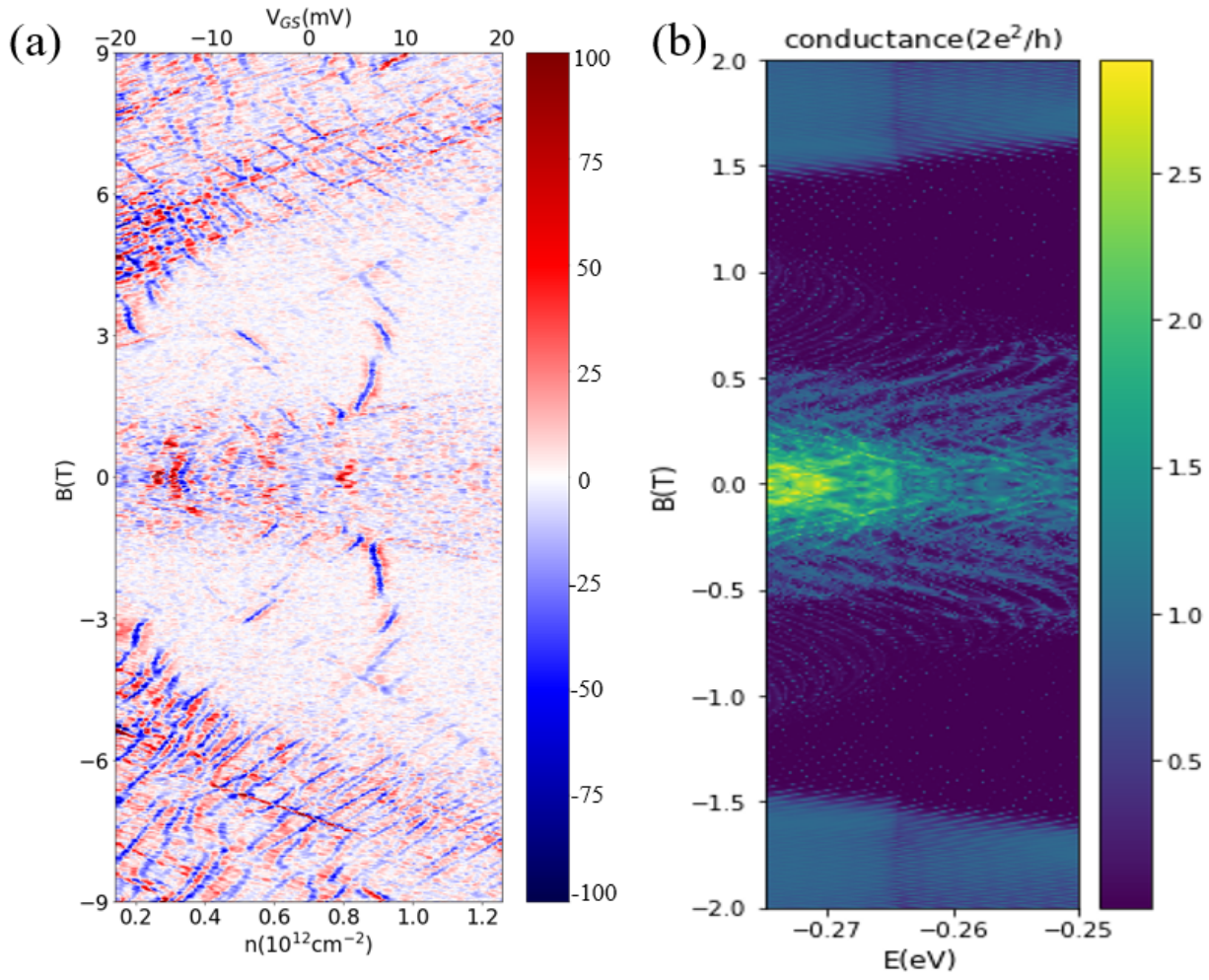

Figure 78: Kwant simulation of graphene resistance under magnetic field (Device 9). (a) Experimental graphene drag resistance. (b) Conductivity of graphene as evaluated numerically using Kwant package.

4.0 Conclusions and outlook

Enormous researches have been done in the two dimensional systems in recent years due to their unique structures and excellent electronic properties. These 2D materials, including semimetallic graphene, and their various heterostructures, show a wide distribution in transport values. The integration of graphene and LAO/STO offers excellent opportunities for studying the correlated system.

In this thesis, graphene with large domain size is obtained by CVD grown method. Copper substrate for growth is cleaned by DTM to reach nanometer-scale flatness. New graphene transferring recipe using Hyflon is developed to improve mobility by reducing the transferring residue. Other processing parameters of the recipe are carefully calibrated, such that the electrical connections are ohmic at low temperature while the writability of the LAO/STO interface is preserved. The graphene etching process with oxygen plasma is also optimized. Graphene/LAO/STO devices show higher mobilities than silicon substrate at low temperature.

Various graphene/LAO/STO devices have been sketched and studied in low temperatures. Graphene quantum dot can be created with a large negative voltage. With moderate tip-voltage, the CNP of graphene on LAO/STO substrates can be shifted locally on the nanoscale with the c-AFM writing technique. $p-n$ junctions can be formed as a result of positive charge doping from c-AFM writing. Edge-state engineering in quantum Hall regime and the observation of quantized longitudinal resistances are direct proofs of the doping effect. The preliminary results of the reversible c-AFM writing technique opens a gate to the fabrication of more complicated nanoscale devices on graphene. A superlattice writing experiment is performed on graphene/LAO/STO. Further studies such as "magic angle" related to graphene superconductivity can also be studied with more precisely controlled c-AFM parameters. The high transparency and conductivity also make graphene an ideal topgate to study the magneto optical effects at LAO/STO interface.

The coulomb drab between graphene and LAO/STO interface is also studied here. The superconductivity of STO offers an ideal platform to study the Coulomb drag between a

superconducting and non-superconducting material. The giant fluctuation of drag resistance, the enhanced drag resistance in STO and the quantum Hall-like behavior of drag in graphene leaves us lots of puzzles and mysterious that need further study. Considering the strong electron-electron pairing in LAO/STO and the electron-hole duality of carriers in graphene and the flexibility of device fabrication using c-AFM also makes it possible to study the interaction between 1D and 2D systems with distinct carrier natures.

Graphene/LAO/STO is configurable on the nanoscale and hosts both superconductivity and strong, tunable electron-electron interactions, making it a very promising platform for both engineering and quantum systems studying.There are many future follow up works can be done. Most importantly, device fabrication technique can be further developed. Dry transfer of graphene with Boron Nitride can greatly reduce residue, thus improve the quality of graphene. Beside, better electrical contact from graphene to gold electrode can be achieved by side contact. More robust contact leads allows for more sophisticated device geometry in the quantum Hall region. Different from the Si substrate, the LAO/STO interface is conducting. However, the conductance can be easily destroyed by ion beam during electrode fabrication process. An optimized fabrication recipe is essential for further study.

To better utilize the electron-hole symmetry property, we would like to tune the graphene to both p and n-type doped region. However, the shielding effect of LAO/STO interface makes it hard to tune the graphene to be n-type doped. By changing the thickness of LAO, the conductance of the LAO/STO interface can be varied. Robust nanostructures with smaller feature size has been achieved by our group with low energy electron beam. This technique along with c-AFM offers great opportunities for further work.

The Coulomb drag between graphene and LAO/STO is surprisingly complicated. The interaction between the two layers is well understood if both layers are in the Fermi-liquid state. Within the Fermi-liquid theory, the drag coefficient is proportional to the square of the temperature. The quadratic dependence in G/LAO/STO may be due to the effect of phonons and plasmons. Coulomb drag in none Fermi-liquid is much more interesting. G/LAO/STO is a novel system to further study strongly correlated, many-body states. Luttinger liquid physics and equilibration processes of drag can be further explored with the edge states of the quantum Hall region. Mesoscopic fluctuations of Coulomb drag in ballistic samples

should be further analyzed. The theory can be extended to the Dirac fermions in graphene.

More broadly speaking, there are many directions for the research on G/LAO/STO to go. Because of its intrinsic complexity with multitude of coupled degree of freedoms, LAO/STO has not been fully understand. For example, superconductivity in STO is still remain a mystery. The phonon mediated interaction between graphene and LAO/STO is not clear. The strong spin-orbit coupling in LAO/STO can also be studied in this hybrid system. All future depends on a precise control and measurement of carrier density in both graphene and LAO/STO. The ability to reliably control the carrier density, using c-AFM lithography and advanced fabrication and characterization technique, could help reveal the new physics we are trying to understand.

Bibliography

[1] Boris Lvovich Altshuler, Patrick A Lee, and W Richard Webb. *Mesoscopic phenomena in solids*. Elsevier, 2012.

[2] Sukang Bae, Hyeongkeun Kim, Youngbin Lee, Xiangfan Xu, Jae-Sung Park, Yi Zheng, Jayakumar Balakrishnan, Tian Lei, Hye Ri Kim, Young Il Song, Young-Jin Kim, Kwang S. Kim, Barbaros Özyilmaz, Jong-Hyun Ahn, Byung Hee Hong, and Sumio Iijima. Roll-to-roll production of 30-inch graphene films for transparent electrodes. *Nature Nanotechnology*, 5:574 – 578, 06 2010.

[3] Karl Heinz Bennemann. *Non-linear optics in metals*. Number 98. Oxford University Press, 1998.

[4] Debasis Bera, Lei Qian, Teng-Kuan Tseng, and Paul H Holloway. Quantum dots and their multimodal applications: a review. *Materials*, 3(4):2260–2345, 2010.

[5] Feng Bi, Daniela F Bogorin, Cheng Cen, Chung Wung Bark, Jae-Wan Park, Chang-Beom Eom, and Jeremy Levy. "water-cycle" mechanism for writing and erasing nanostructures at the $LaAlO_3/SrTiO_3$ interface. *Applied Physics Letters*, 97(17):173110, 2010.

[6] E Breckenfeld, N Bronn, Nadya Mason, and LW Martin. Tunability of conduction at the laalo3/srtio3 heterointerface: thickness and compositional studies. *Applied Physics Letters*, 105(12):121610, 2014.

[7] Alexander Brinkman, Mark Huijben, M Van Zalk, J Huijben, U Zeitler, JC Maan, Wilfred Gerard van der Wiel, GJHM Rijnders, David HA Blank, and H Hilgenkamp. Magnetic effects at the interface between non-magnetic oxides. *Nature materials*, 6(7):493, 2007.

[8] C. Cancellieri, N. Reyren, S. Gariglio, A. D. Caviglia, A. Fête, and J. M. Triscone. Influence of the growth conditions on the $LaAlO_3/SrTiO_3$ interface electronic properties. 91(1):17004, 2010.

[9] Yuan Cao, Valla Fatemi, Ahmet Demir, Shiang Fang, Spencer L Tomarken, Jason Y Luo, Javier D Sanchez-Yamagishi, Kenji Watanabe, Takashi Taniguchi, Efthimios Kaxiras, et al. Correlated insulator behaviour at half-filling in magic-angle graphene superlattices. *Nature*, 556(7699):80, 2018.

[10] Yuan Cao, Valla Fatemi, Shiang Fang, Kenji Watanabe, Takashi Taniguchi, Efthimios Kaxiras, and Pablo Jarillo-Herrero. Unconventional superconductivity in magic-angle graphene superlattices. *Nature*, 556(7699):43, 2018.

[11] A. D. Caviglia, M. Gabay, S. Gariglio, N. Reyren, C. Cancellieri, and J.-M. Triscone. Tunable Rashba spin-orbit interaction at oxide interfaces. *Phys. Rev. Lett.*, 104:126803, Mar 2010.

[12] AD Caviglia, Stefano Gariglio, Nicolas Reyren, Didier Jaccard, T Schneider, M Gabay, Stefan Thiel, German Hammerl, Jochen Mannhart, and J-M Triscone. Electric field control of the laalo 3/srtio 3 interface ground state. *Nature*, 456(7222):624–627, 2008.

[13] Cheng Cen, Stefan Thiel, German Hammerl, Christof W Schneider, KE Andersen, CS Hellberg, Jochen Mannhart, and J Levy. Nanoscale control of an interfacial metal–insulator transition at room temperature. *Nature materials*, 7(4):298–302, 2008.

[14] Cheng Cen, Stefan Thiel, Jochen Mannhart, and Jeremy Levy. Oxide nanoelectronics on demand. *Science*, 323(5917):1026–1030, 2009.

[15] Vadim V Cheianov, Vladimir Fal'ko, and BL Altshuler. The focusing of electron flow and a veselago lens in graphene pn junctions. *Science*, 315(5816):1252–1255, 2007.

[16] JH Chen, C Jang, S Xiao, M Ishigami, and MS Fuhrer. Nat. nanotechnol. 2008.

[17] Guanglei Cheng, Michelle Tomczyk, Shicheng Lu, Joshua P Veazey, Mengchen Huang, Patrick Irvin, Sangwoo Ryu, Hyungwoo Lee, Chang-Beom Eom, C Stephen Hellberg, et al. Electron pairing without superconductivity. *Nature*, 521(7551):196, 2015.

[18] Guanglei Cheng, Michelle Tomczyk, Alexandre B Tacla, Hyungwoo Lee, Shicheng Lu, Josh P Veazey, Mengchen Huang, Patrick Irvin, Sangwoo Ryu, Chang-Beom Eom, et al. Tunable electron-electron interactions in laalo 3/srtio 3 nanostructures. *Physical Review X*, 6(4):041042, 2016.

[19] Nuno J. G. Couto, Benjamin Sacépé, and Alberto F. Morpurgo. Transport through graphene on $SrTiO_3$. *Phys. Rev. Lett.*, 107:225501, Nov 2011.

[20] Rolf Crook, Abi C Graham, Charles G Smith, Ian Farrer, Harvey E Beere, and David A Ritchie. Erasable electrostatic lithography for quantum components. *Nature*, 424(6950):751–754, 2003.

[21] C. R. Dean, A. F. Young, I. Meric, C. Lee, L. Wang, S. Sorgenfrei, K. Watanabe, T. Taniguchi, P. Kim, K. L. Shepard, and J. Hone. Boron nitride substrates for high-quality graphene electronics. *Nature Nanotechnology*, 5:722 EP –, 08 2010.

[22] Cory R Dean, L Wang, P Maher, C Forsythe, Fereshte Ghahari, Y Gao, Jyoti Katoch, M Ishigami, P Moon, M Koshino, et al. Hofstadter's butterfly and the fractal quantum hall effect in moiré superlattices. *Nature*, 497(7451):598, 2013.

[23] Shonali Dhingra. *Quadratic coupling between a classical nanomechanical oscillator and a single spin*. PhD thesis, University of Pittsburgh, 2015.

[24] Shonali Dhingra, Jen-Feng Hsu, Ivan Vlassiouk, and Brian D'Urso. Chemical vapor deposition of graphene on large-domain ultra-flat copper. *Carbon*, 69:188–193, 2014.

[25] Raymond Dingle, Arthur C Gossard, and Horst L Stormer. High mobility multilayered heterojunction devices employing modulated doping, July 31 1979. US Patent 4,163,237.

[26] JP Eisenstein. New transport phenomena in coupled quantum wells. *Superlattices and microstructures*, 12(1):107–114, 1992.

[27] Gyula Eres, Murari Regmi, Christopher M Rouleau, Jihua Chen, Ilia N Ivanov, Alexander A Puretzky, and David B Geohegan. Cooperative island growth of large-area single-crystal graphene on copper using chemical vapor deposition. *ACS nano*, 8(6):5657–5669, 2014.

[28] N Feature. Enter the oxides. *Nature*, 459:28–30, 2009.

[29] Stefano Gariglio, Alexandre Fête, and Jean-Marc Triscone. Electron confinement at the laalo3/srtio3 interface. *Journal of Physics: Condensed Matter*, 27(28):283201, 2015.

[30] S Geller and VB Bala. Crystallographic studies of perovskite-like compounds. ii. rare earth alluminates. *Acta crystallographica*, 9(12):1019–1025, 1956.

[31] RV Gorbachev, AK Geim, MI Katsnelson, KS Novoselov, T Tudorovskiy, IV Grigorieva, Allan H MacDonald, SV Morozov, K Watanabe, T Taniguchi, et al. Strong coulomb drag and broken symmetry in double-layer graphene. *Nature Physics*, 8(12):896–901, 2012.

[32] T. J. Gramila, J. P. Eisenstein, A. H. MacDonald, L. N. Pfeiffer, and K. W. West. Mutual friction between parallel two-dimensional electron systems. *Phys. Rev. Lett.*, 66:1216–1219, Mar 1991.

[33] TJ Gramila, JP Eisenstein, AH MacDonald, LN Pfeiffer, and KW West. Measuring electron—electron scattering rates through mutual friction. *Physica B: Condensed Matter*, 197(1-4):442–448, 1994.

[34] TJ Gramila, JP Eisenstein, Allan H MacDonald, LN Pfeiffer, and KW West. Evidence for virtual-phonon exchange in semiconductor heterostructures. *Physical Review B*, 47(19):12957, 1993.

[35] Christoph W Groth, Michael Wimmer, Anton R Akhmerov, and Xavier Waintal. Kwant: a software package for quantum transport. *New Journal of Physics*, 16(6):063065, 2014.

[36] Melinda Y Han, Barbaros Özyilmaz, Yuanbo Zhang, and Philip Kim. Energy band-gap engineering of graphene nanoribbons. *Physical review letters*, 98(20):206805, 2007.

[37] Douglas R. Hofstadter. Energy levels and wave functions of bloch electrons in rational and irrational magnetic fields. *Phys. Rev. B*, 14:2239–2249, Sep 1976.

[38] B Huard, JA Sulpizio, N Stander, K Todd, B Yang, and D Goldhaber-Gordon. Transport measurements across a tunable potential barrier in graphene. *Physical review letters*, 98(23):236803, 2007.

[39] B Hunt, JD Sanchez-Yamagishi, AF Young, M Yankowitz, Brian J LeRoy, K Watanabe, T Taniguchi, Pilkyung Moon, M Koshino, P Jarillo-Herrero, et al. Massive Dirac fermions and Hofstadter butterfly in a van der Waals heterostructure. *Science*, page 1237240, 2013.

[40] H. Y. Hwang, Y. Iwasa, M. Kawasaki, B. Keimer, N. Nagaosa, and Y. Tokura. Emergent phenomena at oxide interfaces. *Nature Materials*, 11:103 EP –, 01 2012.

[41] Bjarke S. Jessen, Lene Gammelgaard, Morten R. Thomsen, David M. A. Mackenzie, Joachim D. Thomsen, JoséM. Caridad, Emil Duegaard, Kenji Watanabe, Takashi Taniguchi, Timothy J. Booth, Thomas G. Pedersen, Antti-Pekka Jauho, and Peter Bøggild. Lithographic band structure engineering of graphene. *Nature Nanotechnology*, page 1, 2019.

[42] Giriraj Jnawali, Mengchen Huang, Jen-Feng Hsu, Hyungwoo Lee, Jung-Woo Lee, Patrick Irvin, Chang-Beom Eom, Brian D'Urso, and Jeremy Levy. Room-temperature quantum transport signatures in graphene/$LaAlO_3$/$SrTiO_3$ heterostructures. *Advanced Materials*, 29(9):1603488, 2017.

[43] Alexey Kalabukhov, Robert Gunnarsson, Johan Börjesson, Eva Olsson, Tord Claeson, and Dag Winkler. Effect of oxygen vacancies in the srtio 3 substrate on the electrical properties of the laalo 3/ srtio 3 interface. *Physical Review B*, 75(12):121404, 2007.

[44] Dae Woo Kim, Yun Ho Kim, Hyeon Su Jeong, and Hee-Tae Jung. Direct visualization of large-area graphene domains and boundaries by optical birefringency. *Nature nanotechnology*, 7(1):29, 2012.

[45] K. v. Klitzing, G. Dorda, and M. Pepper. New method for high-accuracy determination of the fine-structure constant based on quantized hall resistance. *Phys. Rev. Lett.*, 45:494–497, Aug 1980.

[46] J-S Lee, YW Xie, HK Sato, C Bell, Y Hikita, HY Hwang, and C-C Kao. Titanium d_{xy} ferromagnetism at the $LaAlO_3$/$SrTiO_3$ interface. *Nature materials*, 12(8):703, 2013.

[47] Jianan Li. Graphene-complex oxide heterostructure. September 2019.

[48] Jianan Li, Qing Guo, Lu Chen, Shan Hao, Yang Hu, Jen-Feng Hsu, Hyungwoo Lee, Jung-Woo Lee, Chang-Beom Eom, Brian D'Urso, et al. Reconfigurable edge-state engineering in graphene using laalo3/srtio3 nanostructures. *Applied Physics Letters*, 114(12):123103, 2019.

[49] Gang Liu, Jairo Velasco Jr, Wenzhong Bao, and Chun Ning Lau. Fabrication of graphene p-n-p junctions with contactless top gates. *Applied Physics Letters*, 92(20):203103, 2008.

[50] Timm Lohmann, Klaus von Klitzing, and Jurgen H Smet. Four-terminal magnetotransport in graphene pn junctions created by spatially selective doping. *Nano letters*, 9(5):1973–1979, 2009.

[51] Allan H MacDonald and Rafi Bistritzer. Graphene moiré mystery solved? *Nature*, 474(7352):453–454, 2011.

[52] Jannik C Meyer, Andre K Geim, Mikhail I Katsnelson, Konstantin S Novoselov, Tim J Booth, and Siegmar Roth. The structure of suspended graphene sheets. *Nature*, 446(7131):60–63, 2007.

[53] Rahul Raveendran Nair, Peter Blake, Alexander N Grigorenko, Konstantin S Novoselov, Tim J Booth, Tobias Stauber, Nuno MR Peres, and Andre K Geim. Fine structure constant defines visual transparency of graphene. *Science*, 320(5881):1308–1308, 2008.

[54] Naoyuki Nakagawa, Harold Y Hwang, and David A Muller. Why some interfaces cannot be sharp. *Nature materials*, 5(3):204–209, 2006.

[55] BN Narozhny and A Levchenko. Coulomb drag. *Reviews of Modern Physics*, 88(2):025003, 2016.

[56] BN Narozhny, M Titov, IV Gornyi, and PM Ostrovsky. Coulomb drag in graphene: perturbation theory. *Physical Review B*, 85(19):195421, 2012.

[57] AH Castro Neto, Francisco Guinea, Nuno MR Peres, Kostya S Novoselov, and Andre K Geim. The electronic properties of graphene. *Reviews of modern physics*, 81(1):109, 2009.

[58] Kostya S Novoselov, Andre K Geim, Sergei V Morozov, D Jiang, Y_ Zhang, Sergey V Dubonos, Irina V Grigorieva, and Alexandr A Firsov. Electric field effect in atomically thin carbon films. *science*, 306(5696):666–669, 2004.

[59] Kostya S Novoselov, Andre K Geim, SVb Morozov, Da Jiang, Michail I Katsnelson, IVa Grigorieva, SVb Dubonos, Firsov, and AA. Two-dimensional gas of massless dirac fermions in graphene. *nature*, 438(7065):197–200, 2005.

[60] Kostya S Novoselov, Andre K Geim, SVb Morozov, Da Jiang, Michail I Katsnelson, IVa Grigorieva, SVb Dubonos, Firsov, and AA. Two-dimensional gas of massless dirac fermions in graphene. *nature*, 438(7065):197–200, 2005.

[61] A Ohtomo and HY Hwang. A high-mobility electron gas at the laalo 3/srtio 3 heterointerface. *Nature*, 427(6973):423–426, 2004.

[62] Barbaros Özyilmaz, Pablo Jarillo-Herrero, Dmitri Efetov, Dmitry A Abanin, Leonid S Levitov, and Philip Kim. Electronic transport and quantum hall effect in bipolar graphene p-n-p junctions. *Physical Review Letters*, 99(16):166804, 2007.

[63] Yun-Yi Pai, Anthony Tylan-Tyler, Patrick Irvin, and Jeremy Levy. Physics of srtio3-based heterostructures and nanostructures: a review. *Reports on Progress in Physics*, 81(3):036503, 2018.

[64] L. A. Ponomarenko, R. V. Gorbachev, G. L. Yu, D. C. Elias, R. Jalil, A. A. Patel, A. Mishchenko, A. S. Mayorov, C. R. Woods, J. R. Wallbank, M. Mucha-Kruczynski, B. A. Piot, M. Potemski, I. V. Grigorieva, K. S. Novoselov, F. Guinea, V. I. Fal'ko, and A. K. Geim. Cloning of Dirac fermions in graphene superlattices. *Nature*, 497:594 EP –, 05 2013.

[65] AS Price, AK Savchenko, BN Narozhny, G Allison, and DA Ritchie. Giant fluctuations of coulomb drag in a bilayer system. *Science*, 316(5821):99–102, 2007.

[66] C emsp14N emsp14R Rao, A emsp14K Sood, K emsp14S Subrahmanyam, and Achutharao Govindaraj. Graphene: the new two-dimensional nanomaterial. *Angewandte Chemie International Edition*, 48(42):7752–7777, 2009.

[67] Chintamani Nagesa Ramachandra Rao and Ajay K Sood. *Graphene: synthesis, properties, and phenomena*. John Wiley & Sons, 2013.

[68] Nicolas Reyren, S Thiel, AD Caviglia, L Fitting Kourkoutis, German Hammerl, Christoph Richter, CW Schneider, Thilo Kopp, A-S Rüetschi, Didier Jaccard, et al. Superconducting interfaces between insulating oxides. *Science*, 317(5842):1196–1199, 2007.

[69] W. D. Rice, P. Ambwani, M. Bombeck, J. D. Thompson, G. Haugstad, C. Leighton, and S. A. Crooker. Persistent optically induced magnetism in oxygen-deficient strontium titanate. *Nature Materials*, 13:481 EP –, 03 2014.

[70] P Rotter, M Suhrke, and U Rössler. Observability of the magnetic band structure of lateral superlattices. *Physical Review B*, 54(7):4452, 1996.

[71] Raymond Sachs, Zhisheng Lin, and Jing Shi. Ferroelectric-like $SrTiO_3$ surface dipoles probed by graphene. *Scientific Reports*, 4:3657 EP –, 01 2014.

[72] T Sakudo and H Unoki. Dielectric properties of srti o 3 at low temperatures. *Physical review letters*, 26(14):851, 1971.

[73] M. Salluzzo, J. C. Cezar, N. B. Brookes, V. Bisogni, G. M. De Luca, C. Richter, S. Thiel, J. Mannhart, M. Huijben, A. Brinkman, G. Rijnders, and G. Ghiringhelli.

Orbital reconstruction and the two-dimensional electron gas at the $LaAlO_3/SrTiO_3$ interface. *Phys. Rev. Lett.*, 102:166804, Apr 2009.

[74] U Sivan, PM Solomon, and H Shtrikman. Coupled electron-hole transport. *Physical review letters*, 68(8):1196, 1992.

[75] PM Solomon and B Laikhtman. Mutual drag of 2d and 3d electron gases in heterostructures. *Superlattices and microstructures*, 10(1):89–94, 1991.

[76] PM Solomon, PJ Price, DJ Frank, and DC La Tulipe. New phenomena in coupled transport between 2d and 3d electron-gas layers. *Physical review letters*, 63(22):2508, 1989.

[77] Joseph A Sulpizio, Shahal Ilani, Patrick Irvin, and Jeremy Levy. Nanoscale phenomena in oxide heterostructures. *Annual Review of Materials Research*, 44:117–149, 2014.

[78] Yuhe Tang, Jung-Woo Lee, Anthony Tylan-Tyler, Hyungwoo Lee, Michelle Tomczyk, Mengchen Huang, Chang-Beom Eom, Patrick Irvin, and Jeremy Levy. Frictional drag between superconducting laalo3/srtio3 nanowires. *Semiconductor Science and Technology*, 2020.

[79] Yuhe Tang, Anthony Tylan-Tyler, Hyungwoo Lee, Jung-Woo Lee, Michelle Tomczyk, Mengchen Huang, Chang-Beom Eom, Patrick Irvin, and Jeremy Levy. Long-range non-coulombic electron–electron interactions between laalo3/srtio3 nanowires. *Advanced Materials Interfaces*, 6(15):1900301, 2019.

[80] Stefan Thiel, German Hammerl, Andreas Schmehl, Christof W Schneider, and Jochen Mannhart. Tunable quasi-two-dimensional electron gases in oxide heterostructures. *Science*, 313(5795):1942–1945, 2006.

[81] HC Tso, P Vasilopoulos, and FM Peeters. Direct coulomb and phonon-mediated coupling between spatially separated electron gases. *Physical review letters*, 68(16):2516, 1992.

[82] HC Tso, P Vasilopoulos, and PM Peeters. Coupled electron-hole transport: generalized random-phase approximation and density functional theory. *Surface science*, 305(1-3):400–404, 1994.

[83] Jairo Velasco Jr, Long Ju, Dillon Wong, Salman Kahn, Juwon Lee, Hsin-Zon Tsai, Chad Germany, Sebastian Wickenburg, Jiong Lu, Takashi Taniguchi, et al. Nanoscale control of rewriteable doping patterns in pristine graphene/boron nitride heterostructures. *Nano letters*, 16(3):1620–1625, 2016.

[84] Jairo Velasco Jr, Gang Liu, Wenzhong Bao, and Chun Ning Lau. Electrical transport in high-quality graphene pnp junctions. *New Journal of Physics*, 11(9):095008, 2009.

[85] Maud Vinet and Nicolas Posseme. Cmos devices through the years. In *Plasma Etching Processes for CMOS Devices Realization*, pages 1–21. Elsevier, 2017.

[86] Ivan Vlassiouk, Murari Regmi, Pasquale Fulvio, Sheng Dai, Panos Datskos, Gyula Eres, and Sergei Smirnov. Role of hydrogen in chemical vapor deposition growth of large single-crystal graphene. *ACS Nano*, 5(7):6069–6076, 07 2011.

[87] Philip Richard Wallace. The band theory of graphite. *Physical review*, 71(9):622, 1947.

[88] Hong Wang, Guanzhong Wang, Pengfei Bao, Shaolin Yang, Wei Zhu, Xing Xie, and Wen-Jun Zhang. Controllable synthesis of submillimeter single-crystal monolayer graphene domains on copper foils by suppressing nucleation. *Journal of the American Chemical Society*, 134(8):3627–3630, 2012.

[89] JR Williams, L DiCarlo, and CM Marcus. Quantum Hall effect in a gate-controlled pn junction of graphene. *Science*, 317(5838):638–641, 2007.

[90] JR Williams, Tony Low, MS Lundstrom, and CM Marcus. Gate-controlled guiding of electrons in graphene. *Nature nanotechnology*, 6(4):222, 2011.

[91] Mark Wilson. Electrons in atomically thin carbon sheets behave like massless particles. *Physics Today*, 59(1):21, 2006.

[92] Joseph M Wofford, Shu Nie, Kevin F McCarty, Norman C Bartelt, and Oscar D Dubon. Graphene islands on Cu foils: the interplay between shape, orientation, and defects. *Nano letters*, 10(12):4890–4896, 2010.

[93] Andrea F Young and Philip Kim. Quantum interference and Klein tunnelling in graphene heterojunctions. *Nature Physics*, 5(3):222, 2009.

[94] Yi Zhang, Zhen Li, Pyojae Kim, Luyao Zhang, and Chongwu Zhou. Anisotropic hydrogen etching of chemical vapor deposited graphene. *ACS Nano*, 6(1):126–132, 01 2012.

[95] Yue Zhao, Jonathan Wyrick, Fabian D Natterer, Joaquin F Rodriguez-Nieva, Cyprian Lewandowski, Kenji Watanabe, Takashi Taniguchi, Leonid S Levitov, Nikolai B Zhitenev, and Joseph A Stroscio. Creating and probing electron whispering-gallery modes in graphene. *Science*, 348(6235):672–675, 2015.